Technical Physics Letters, Vol. 26, No. 3, 2000, pp. 179–181. Translated from Pis'ma v Zhurnal Tekhnicheskoĭ Fiziki, Vol. 26, No. 5, 2000, pp. 1–6.

Highly Effective Phototransducers Based on Polycrystalline Heterostructures of $A^{II}B^{VI}$ Compounds

A. V. Komashchenko, K. V. Kolezhuk, P. P. Gorbik, M. O. Maĭ, and G. I. Sheremetova

Institute of Semiconductor Physics, National Academy of Sciences of Ukraine, Kiev, 252028 Ukraine

Received August 5, 1999

Abstract—Thin-film polycrystalline heterostructures based on $A^{II}B^{VI}$ compounds were prepared, and related highly effective surface-barrier phototransducers of the *p*-$Cu_{1.8}S$/*n*-$A^{II}B^{VI}$/*n*-$A^{II}B^{VI}$ type (with a quantum efficiency of ~0.9) were obtained. The heterostructures are promising materials for the creation of solar cells and UV photodetectors insensitive to the visible light. © *2000 MAIK "Nauka/Interperiodica".*

Surface-barrier phototransducers of the *p*-$Cu_{1.8}S$/*n*-CdS type have been studied in sufficient detail [1–3]. These structures served as base elements for the creation of solar cells and radiation detectors for the short-wave optical range. In particular, the *p*-$Cu_{1.8}S$/*n*-CdS structure was implemented in commercial UV photodetectors (of the FPD-1, SKB, Spektr, and Kiev types). These devices, while possessing a sensitivity comparable to that of Si and GaP based photodetectors, are more stable in operation under the action of high-intensity UV radiation.

The purpose of this work was to implement some concepts, realized in single-crystal lattice-matched systems based on $A^{III}B^{V}$ compounds [4], in heterostructures involving polycrystalline films of $A^{II}B^{VI}$ semiconductors (featuring no materials with close crystal lattice parameters) with a view of creating highly effective phototransducers of new types.

The samples for investigation were prepared by depositing layers of $A^{II}B^{VI}$ compounds using the hot-wall technique [5, 6] with several independent sources. One of the main distinctions of our samples from the known structures consisted in that the polycrystalline layers were deposited under conditions providing for the quasi-epitaxial growth on oriented polycrystalline substrates. The substrates were represented by low-resistivity CdS films with a thickness of about 3 μm deposited onto metal-coated Sitall (devitrified glass ceramic) plates. The working layers of heterostructures were deposited onto these substrates in a single technological cycle (without breaking high-vacuum conditions). The thickness of the working layers (~0.6–1.0 μm) approximately corresponded to the thickness of a photoactive region, representing a sum of the space-charge region length and the hole diffusion length in *n*-$A^{II}B^{VI}$. Transition layers of low thickness (less than 500 Å) and variable chemical composition were built in between the oriented substrate and the working region. These layers allowed the lattice mismatch to be markedly reduced and provided for the obtaining of thin, high-quality photoactive layers. The heterostructure preparation was terminated, as described in [1–3], by thermal vacuum deposition of a thin (~300 Å) $Cu_{1.8}S$ film possessing conductivity of the *p*-type.

A characteristic feature of the structures studied in this work (as well as those described previously) was a sharp asymmetric *p–n* transition between degenerate copper sulfide (hole concentration $p \sim 5 \times 10^{21}$ cm^{-3}) and $A^{II}B^{VI}$ (electron concentration $n \sim 10^{14}$–10^{15} cm^{-3}). For this reason, the space-charge region is fully concentrated in $A^{II}B^{VI}$, while the $Cu_{1.8}S$ layer does not significantly contribute to the photoeffect (except for a situation considered in [3]).

Figure 1 shows the curves of quantum yield η for the heterostructures of several types studied. As seen, the minimum value of η is observed in a heterostructure of the *p*-$Cu_{1.8}S$/*n*-ZnS/*n*-CdS type (curve *1*). The quantum yield of a *p*-$Cu_{1.8}S$/*n*-CdTe/*n*-CdS structure (curve *3*) is close to theoretical limit (η ~ 0.94). We believe that the degree of fitting between the lattice parameters of substrate (CdS) and photoactive layers was approximately the same in all structures (as provided by the method of structure formation).

Figure 2 shows schematic energy band diagrams of the *n–n* heterojunction between the substrate and active region of some structures (the lattice-matching interlayers are not depicted). The band diagrams of heterojunctions of the *p*-$Cu_{1.8}S$/*n*-$A^{II}B^{VI}$ type are well known and not presented in Fig. 2. Note a principally different character of the potential barrier ΔE_v at the boundary of semiconductors with different bandgaps. In the structures depicted in schemes *2* and *3*, the presence of ΔE_v barrier for holes favors a decrease in recombination losses in the region of rear contact, which mostly

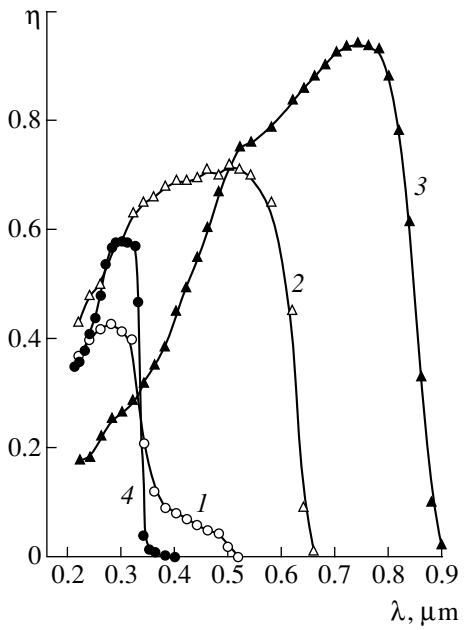

Fig. 1. Spectral characteristics (quantum yield η vs. wavelength) of the heterostructures studied: (*1*) *p*-$Cu_{1.8}S$/*n*-ZnS/*n*-CdS; (*2*) *p*-$Cu_{1.8}S$/*n*-CdSe/*n*-CdS; (*3*) *p*-$Cu_{1.8}S$/*n*-CdTe/*n*-CdS; (*4*) *p*-$Cu_{1.8}S$/*n*-ZnS/*n*-CdSe.

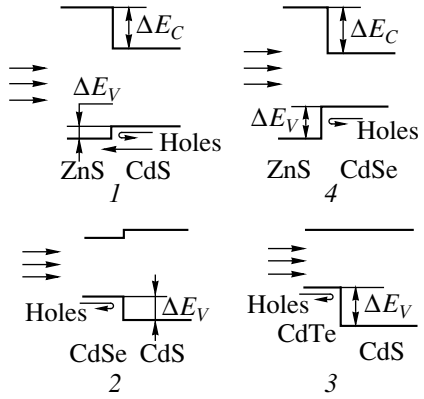

Fig. 2. Schematic energy band diagrams of heterojunctions in *p*-$Cu_{1.8}S$/*n*-$A^{II}B^{VI}$/*n*-$A^{II}B^{VI}$ structures: (*1*) *n*-ZnS/*n*-CdS; (*2*) *n*-CdSe/*n*-CdS; (*3*) *n*-CdTe/*n*-CdS; (*4*) *n*-ZnS/*n*-CdSe.

accounts for the high values of η. Note also that the high η value is partly due to small optical losses, which is a feature in common for polycrystalline surface-barrier structures of the *p*-$Cu_{1.8}S$/$A^{II}B^{VI}$ type. This feature is related to low reflectance of textured polycrystalline surfaces and high transmittance (>90%) of thin copper sulfide films in the visible spectral range.

The spectral characteristic of a heterostructure of the *p*-$Cu_{1.8}S$/*n*-CdSe/*n*-CdS type exhibits a shift of the longwave photoelectric threshold toward shorter wavelengths (Fig. 1, curve *2*). This is explained by the fact that the CdSe layer thickness (<0.6 μm) in the studied sample was insufficient for effective absorption of the edge radiation. At the same time, the diode characteristics of this structure approximately correspond to those for the optimum CdSe layer thickness. This fact is evidence of a high quality of even rather thin photosensitive layers.

The *n*-ZnS/*n*-CdS system represents a heterojunction of the type that must exhibit the wideband window effect (illumination on the ZnS side, space-charge region length is about twice the ZnS layer thickness). However, the current response in the spectral region of the intrinsic absorption of CdS was markedly lower than expected (Fig. 1, curve *1*). This is explained by a small value of $\Delta E_v \sim 0.2$ eV (Fig. 2, scheme *1*), which makes the barrier partly transparent for minority carriers photogenerated in this region, nevertheless, significantly restricting their transfer to a wideband component of the heterostructure.

This situation (the presence of a barrier for minority carriers at the heterojunction) can be used for the development of photoelectric devices of new types. For example, an important current task in the sensor microelectronics is to create a UV detector that would be "blind" in the visible spectral range. Attempts at manufacturing such a detector based on a wideband zinc sulfide were unsuccessful because of a number of technological difficulties related to the preparation of a thin perfect low-resistance ZnS film and formation of an ohmic contact on this film. As demonstrated above, this problem can be bypassed using cadmium sulfide as an electrode material and the oriented substrate.

In order to eliminate sensitivity of the heterostructure in the visible range (beyond the intrinsic absorption edge of ZnS), it is necessary to select a semiconductor creating a potential barrier in the valence band at the heterojunction with ZnS, the magnitude of which would be sufficiently high to exclude contribution of the narrowband component to the total photocurrent. A promising material of this kind, readily obtained with preset electrophysical characteristics, is cadmium selenide. A potential barrier height in this heterojunction is $\Delta E_v \sim 0.8$ eV (Fig. 2, scheme *4*). The spectral characteristic of a *p*-$Cu_{1.8}S$/*n*-ZnS/*n*-CdSe heterostructure on a polycrystalline CdSe substrate (Fig. 1, curve *4*) shows the absence of the narrowband component contribution to the total photocurrent. The current response at a wavelength of $\lambda = 0.25$ μm reaches 0.12 A/W. Under natural illumination conditions (summer cloudless midday, medium latitude), the fraction of photoresponse in the longwave spectral range ($\lambda > 0.4$ μm) was smaller than 1% of the integral photoresponse for heterostructures of this type.

Thus, we have obtained heterostructures based on high-quality photoactive layers of $A^{II}B^{VI}$ compounds deposited onto oriented polycrystalline substrates by the hot-wall technique. Highly effective thin-film surface-barrier phototransducers of the *p*-$Cu_{1.8}S$/*n*-$A^{II}B^{VI}$/*n*-$A^{II}B^{VI}$ type (with a quantum efficiency of ~0.9) were manufac-

tured. The heterostructures are promising materials for the creation of solar cells and new shortwave phototransducers, in particular, photodetectors insensitive to the visible light.

The authors are grateful to V.N. Komashchenko for initiation of this study and fruitful discussions.

REFERENCES

1. K. V. Kolezhuk, A. V. Komashchenko, S. Yu. Pavelets, *et al.*, Pis'ma Zh. Tekh. Fiz. **16**, 48 (1990).
2. Yu. N. Bobrenko, V. V. Kislyuk, K. V. Kolezhuk, *et al.*, Solar Energ. Mater. Solar Cells **33**, 83 (1994).
3. Yu. N. Bobrenko, A. M. Pavelets, S. Yu. Pavelets, *et al.*, Pis'ma Zh. Tekh. Fiz. **20**, 9 (1994).
4. Zh. I. Alferov, Fiz. Tekh. Poluprovodn. (St. Petersburg) **32**, 3 (1998).
5. A. López-Otero, Thin Solid Films **49**, 3 (1978).
6. I. P. Kalinkin, V. B. Aleskovskiĭ, and A. B. Simashkevich, *Epitaxial Films of $A^{II}B^{VI}$ Compounds* [in Russian] (Izdat. Len. Gos. Univ., Leningrad, 1978).

Translated by P. Pozdeev

Technical Physics Letters, Vol. 26, No. 3, 2000, pp. 182–183. Translated from Pis'ma v Zhurnal Tekhnicheskoĭ Fiziki, Vol. 26, No. 5, 2000, pp. 7–10.

Influence of Size Factor on Martensite Transformations and Shape Memory Effects in TiNi Based Alloys

V. É. Gyunter, V. V. Ovcharenko, and A. A. Klopotov

Research Institute of Materials for Medicine and Implants with Shape Memory, Tomsk, Russia

Received October 7, 1999

Abstract—The results of the studies of electrical and mechanical properties of fine and hyperfine wires prepared from titanium nickelide based alloys (TN-10 grade) are presented. It is established that the temperature range of the martensite transformations shifts to lower temperatures with a decrease in the specimen diameter. Oxide films formed on the surface of thin specimens deteriorate the parameters responsible for shape changes in the specimens possessing the shape memory effect. © *2000 MAIK "Nauka/Interperiodica".*

The unique electrical and mechanical properties of titanium nickelide based alloys possessing the shape memory effect account for their use in solving numerous practical problems. Many devices used in medicine and technology are manufactured with the use of fine (about 1 mm in diameter) and hyperfine (less than 0.5 mm in diameter) wires [1]. However, there are almost no publications on the comparative analysis of the properties of the specimens of various diameters prepared from titanium nickelide based alloys. Therefore, we had the aim to study the influence of the size factor (the diameter of a wire specimen) on the martensite transformations and the shape memory effect in a titanium nickelide based alloy of the TN-10 grade. This alloy possesses a number of attractive physical and mechanical properties, including the working temperature range convenient for various medical applications, good parameters of shape restoration, and high technological characteristics.

The wire specimens with various diameters were obtained from an ingot by pulling through a draw plate with intermediate anneals. Then the specimens were subjected to one-hour vacuum annealing at 850°C. During the preparation of wire specimens, their surfaces oxidized with the formation of an oxide layer [1]. This oxide film was removed by chemical etching. Martensite transformations in the specimens were studied by measuring the temperature dependence of electric resistance. The shape memory effect was studied under the conditions of constant loading and variation of the critical stresses of the martensite shift. These experiments were performed in a specially designed test complex.

Using the temperature dependence of resistance, one may determine the characteristic temperatures of martensite transformations in TiNi-based alloys [1]. Figure 1a shows the temperature variation of the resistance of a TN-10 wire with a diameter of 1.8 mm. During specimen cooling, the $R(T)$ curve starts rising at the temperature T_R corresponding to the onset of the $B2$–R transition, whereas the onset of decrease of the resistance is observed in the vicinity of the maximum corresponding to the temperature M_1 of the start of the R–$B19'$ martensite transformation. The temperature M_2 characterizes the completion of the R–$B19'$ martensite transformation (Fig. 1a) [1]. The study of the effect of the specimen diameter on the characteristic temperatures of martensite transformations shows that, with a decrease of the diameter of the specimen (with or without an oxide film), the range of the martensite transformations shifts toward low temperatures (Fig. 1b). The presence of an oxide film on the surface of a thin wire specimen results in a more pronounced decrease of the temperature M_1 as compared to that in the specimen without the oxide film. This is explained by the nature of thin wire specimens, in which the oxide film thickness is comparable with the transverse dimensions of the wire. Although the oxide film covering the specimen surface does not participate in the martensite transformations, it produces a considerable effect on the crystal lattice reconstruction during the phase transition (by hindering the motion of interphase boundaries).

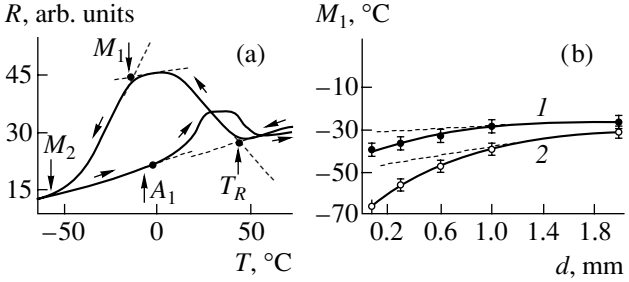

Fig. 1. (a) Temperature dependence of the electric resistance of wire specimens (1.8 mm in diameter) prepared from a TN-10 alloy and (b) the temperature M_1 of the start of the martensite transformation as function of the wire diameter for specimens (*1*) without and (*2*) with an oxide film.

1063-7850/00/2603-0182$20.00 © 2000 MAIK "Nauka/Interperiodica"

At a certain critical value of the wire diameter (less than 1.0 mm), the transverse specimen dimension begins to noticeably affect the martensite transformation and the $M_1 = f(d)$ curves start deviating from the linear law (Fig. 1b). The smaller the specimen diameter, the more pronounced the decrease in the M_1 temperature.

The influence of the size factor is especially clearly manifested in the shape memory effect. Indeed, the parameters characterizing the shape memory effect are significantly dependent on variations in the specimen diameter. These parameters are the loading strain ε_1, the reversible strain on heating under loading ε_2, the residual deformation upon the shape restoration during heating ε_3, the accumulated strain during cooling ε_4, the width of the hysteresis loop ΔH, and the total accumulated strain $\varepsilon_5 = \varepsilon_4 + \varepsilon_1 = \varepsilon_2 + \varepsilon_3$ (Fig. 2). With a decrease in the wire diameter, the width of the hysteresis loop increases, the accumulated strain decreases, and the level of the residual strain grows. In other words, the parameters of the shape memory effect used in practice are considerably deteriorated.

Thus, it is established that the size factor has a considerable influence on the martensite transformations and the shape memory effects taking place in TiNi-based wire specimens. The presence of an oxide film on the surface of thin wire specimens considerably shifts the temperature range of the martensite transformations toward low temperatures and deteriorates the parameters responsible for shape changing in wires with the shape-memory effect.

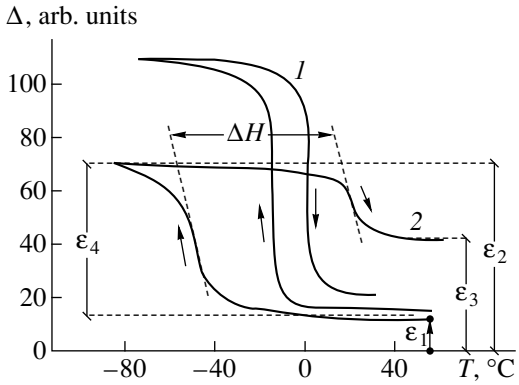

Fig. 2. Shape memory effect (strain accumulation and recovery) in a wire (0.6 mm in diameter) of the TN-10 alloy (*1*) without and (*2*) with an oxide film.

REFERENCES

1. V. É. Gyunter, G. Ts. Dambaev, P. G. Sysolyatin, *et al.*, *Materials for Medicine and Implants with Shape Memory* (Tomsk State University, Tomsk, 1998).

Translated by L. Man

Technical Physics Letters, Vol. 26, No. 3, 2000, pp. 184–186. Translated from Pis'ma v Zhurnal Tekhnicheskoĭ Fiziki, Vol. 26, No. 5, 2000, pp. 11–16.

Selection of the Annealing Regimes for Irradiated Diamonds

V. V. Frunze, A. Yu. Tsutskikh, and A. V. Krasil'nikov

Troitsk Institute for Innovation and Thermonuclear Research, Troitsk, Moscow oblast, 142092 Russia

Received August 23, 1999

Abstract—A diamond graphitization curve is plotted by the experimental data for $T < 2000$ K. A formula is derived for the calculation of the maximum pressure to provide for an optimum diamond annealing at a preset temperature and duration of the treatment. © *2000 MAIK "Nauka/Interperiodica".*

The diamond detectors of nuclear radiation, which are exposed to a high fluence of neutrons, are susceptible to accumulation of the crystal structure imperfections known as the intrinsic defects [1, 2]. The particular type of these defects is formed depending significantly on the degree of diamond perfection, that is, on the initial content and type of intrinsic and impurity defects. During annealing of an irradiation-damaged diamond, the defects acquire mobility and migrate over the crystal to feature various changes, including decay, conversion to other types, etc. This process leads eventually to the recovery of lost or deteriorated properties and characteristics of the diamond detectors. Unfortunately, the annealing may also produce an undesired effect of the diamond graphitization.

The initial crystal structure of diamond with covalent interatomic bonds is a sufficiently stable system, but heating may transfer this system to a state where the dissociation energy barrier can be surmounted and the atoms would become separated by macroscopic distances. This process is accompanied by a transition from sp^3 to sp^2 electron state, whereby one of the four covalent bonds transforms into a readily breakable contact of the van der Waals type. This results in reconstruction of the crystal lattice [3].

The purpose of this work was to construct a diamond graphitization curve and solve the task of selecting an optimum regime of diamond annealing at $T <$ 2000 K, that is, determine the maximum residual air pressure at a preset temperature and duration of the treatment.

Figure 1 shows a curve of pressure as function of the temperature of the diamond–graphite transition $P(T, °C)$ plotted using the following experimental values: four points (square symbols) were taken from tabulated data [4], three points (black circles) were obtained in our experiments on the natural diamond crystals of type II, and one point (triangle and rhombus) was taken from each of the works [5, 6], respectively.

This phase diagram of the graphitization process, covering nine orders with respect to pressure, determines the boundary state featuring the surface oxidation and graphitization of annealed diamonds. For example, the point (square) at $T = 1400°C$ in a vacuum of 6×10^{-6} Torr corresponds [4] to a 1–2-μm-thick graphite film formed within 10 min. As seen from Fig. 1, the temperature of a diamond annealed at a pressure of 10^{-4} Torr should not be increased above 1200°C, otherwise the danger of graphitization development would arise. Evidently, the annealing of diamonds at a given temperature should be performed at a pressure under the boundary curve $P(T, °C)$ of the pressure versus the temperature of the diamond–graphite transition. Heating an irradiation-damaged diamond crystal even at comparatively low temperatures and pressure may lead to the annealing of radiation-induced defects accompanied by graphitization of the crystal.

A part of the graphitization curve presented in Fig. 1, namely that for $T = 1400$–$1700°C$, represents a straight line described by the equation $P(T, °C) = 9.01235 \times 10^{-6} – 2.41765 \times 10^{-9}$ T (Torr). Another part of this curve, corresponding to the temperature range from 980 to 1400°C can be approximately descried by

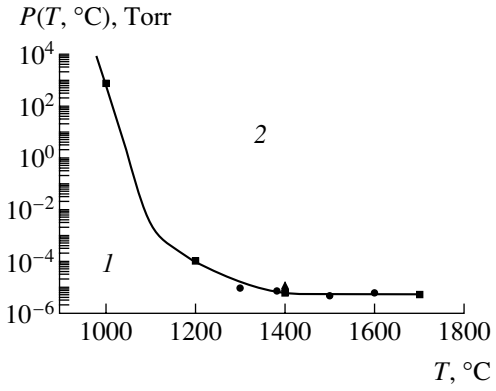

Fig. 1. The graphitization curve $P(T, °C)$ representing a plot of pressure vs. temperature for the transition from diamond (regions *1*) to graphite structure (region *2*).

1063-7850/00/2603-0184$20.00 © 2000 MAIK "Nauka/Interperiodica"

the function $P(T, °C) = \exp(\sum a_i T_i)$ (Torr). This function and the corresponding experimental plot are depicted in Fig. 2.

A reasonable task is to minimize the pressure of defect annealing in diamonds according to the function $P_{ann} = P(T, °C)/[(t/t^*)^{1/4} + \alpha]$ (Torr), which allows the vacuum (pressure) under the graphitization curve $P(T, °C)$ to be determined for the high-quality annealing of diamonds involving no surface graphitization. The point at $T = 1400°C$, belonging to the middle of the temperature interval under consideration (1000–1700°C), is characterized by the time $t^* = 10$ min during which a 1–2-μm-thick graphite film is formed on the surface of diamond annealed in a vacuum of 6×10^{-6} Torr. The parameter α cannot be taken smaller than unity, otherwise starting at $t = 0$ we would obtain $P_{ann} > P(T, °C)$ for a given temperature T (°C), which is unacceptable for the high-quality annealing of irradiation-induced defects in diamond. Estimates obtained by solving the above problem of minimization showed that α cannot exceed unity, so that we arrive at $\alpha = 1$. The exponent 1/4 was selected by fitting so as to provide coincidence of the calculated P_{ann} values to the experimental pressures at which the annealing treatment produced no diamond graphitization.

Figure 3 shows the results of calculation of the annealing pressures for $\alpha = 1$ and the treatment durations t = 30–30000 min (0.5–500 h). The curves are equidistant relative to each other and with respect to the graphitization curve ($t = 0$), from which they are shifted by the value of denominator $[(t/10)^{14} + 1]$ in the above expression for P_{ann}. As seen from Fig. 3, an increase in the duration of annealing at any fixed temperature requires a decrease in pressure (i.e., a better vacuum). For example, annealing in the temperature interval T = 1500–1700°C for t = 3000 min (50 h) must be performed in a vacuum from 1.02×10^{-6} to 9.69×10^{-7} Torr, that is, at a pressure equal to 1/5 of that according to the graphitization curve in the same temperature interval.

Examination of the published data showed that annealing is usually performed at lower pressures (higher vacuum conditions) than required. For example, in [7] the annealing of three CVD diamonds and a natural crystal of type IIa was effected at 420–540°C in an evacuated quartz cylinder placed inside a tubular furnace. In [8], diamonds were annealed at temperatures between 600 and 800°C in a quartz cylinder evacuated to 10^{-5} Torr [8]. As seen from Fig. 1, the points corresponding to these annealing regimes are situated far on the left from the curve of diamond–graphite transition.

If it is impossible to reduce the pressure to $\sim 10^{-6}$ Torr for the safe high-temperature annealing of defects in diamonds, the annealing should be performed at a lower pressure of 5×10^{-6} Torr (not exceeding that on the graphitization curve) and followed by etching the samples in an $H_2SO_4 \cdot K_2Cr_2O_7$ at 200°C for 10–15 min to remove the deteriorated surface layer (the diamond crystal proper is virtually not etched at this temperature) [5].

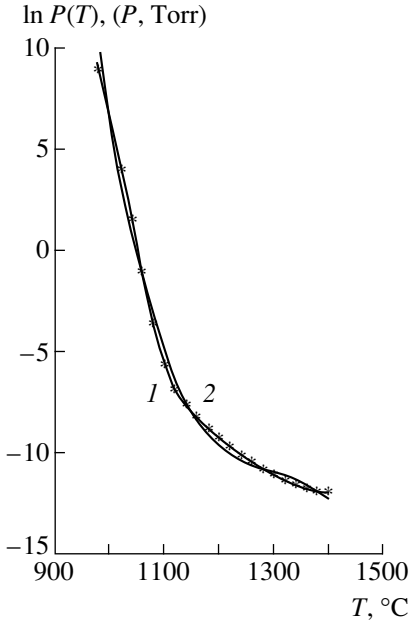

Fig. 2. A part of the (*1*) graphitization curve and (*2*) its approximation by the function $P = (\sum_{i=0}^{i=3} a_i T_i)$ for a_0 = 1189.23, a_1 = – 2.7494, $a_2 = 2.10572 \times 10^{-3}$, and $a_3 = -5.39216 \times 10^{-7}$ for T = 980–1400°C.

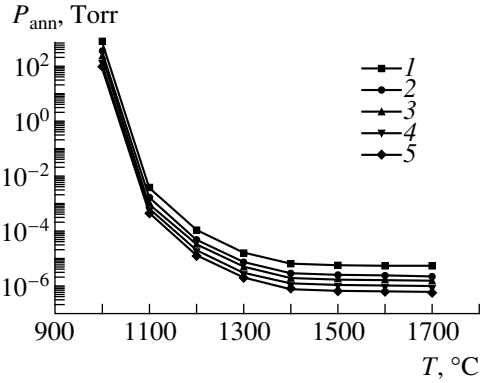

Fig. 3. Calculated plots of P_{ann} vs. temperature for various annealing durations t (min): (*1*) 0; (*2*) 30; (*3*) 300; (*4*) 3000; (*5*) 30000.

The proposed graphitization curve and the empirical formula for calculation of the residual air pressure during the annealing of defects in diamonds in the temperature interval $T < 2000$ K allow one to determine a maximum pressure for preset temperature and duration of the treatment. We have demonstrated that the annealing at T = 600–800°C can be performed using only a rough (mechanical) vacuum pump providing a pressure of

10^{-3} Torr, which implies a much simpler procedure and less expensive equipment as compared to that in a high-vacuum pumping stage.

The recommended (calculated) pressure P_{ann} for the annealing can be even increased by using a setup with graphite crucible. The crucible containing diamonds to be annealed is placed into a vacuum chamber, covered with a graphite lid, evacuated, and heated [5]. The atmosphere surrounding diamonds is additionally depleted of oxygen, which is absorbed by the graphite crucible. This factor eliminates the main reason for the graphite formation on the diamond surface.

This work was supported by the International Science and Technology Center, project no. 447.

REFERENCES

1. G. Davies and A. T. Collins, Diamonds and Relat. Mater., No. 2, 80 (1993).
2. *Natural Diamonds of Russia* [in Russian], Ed. by V. B. Kvaskov (Polaron, Moscow, 1997).
3. V. D. Andreev, Fiz. Tverd. Tela (St. Petersburg), **41** (4), 695 (1999).
4. É. N. Marmer, *Carbon-Graphite Composites. A Handbook* [in Russian] (Metallurgiya, Moscow, 1973).
5. M. A. Gukasyan and E. A. Konorova, Almazy, No. 1, 1 (1973).
6. E. A. Konorova and S. F. Kozlov, Fiz. Tekh. Poluprovodn. (Leningrad) **4**, 1865 (1970).
7. L. Allers, A. T. Collins, and J. Hiscock, Diamonds and Relat. Mater., No. 7, 228 (1998).
8. G. Davies, S. C. Lawson, and A. T. Collins, Phys. Rev. B **46**, 13157 (1992).

Translated by P. Pozdeev

Technical Physics Letters, Vol. 26, No. 3, 2000, pp. 187–189. Translated from Pis'ma v Zhurnal Tekhnicheskoĭ Fiziki, Vol. 26, No. 5, 2000, pp. 17–22.

Charge Carrier Recombination via Isoelectronic Traps Involving Excitons in Compensated Semiconductors

S. Zh. Karazhanov

Starodubtsev Physicotechnical Institute, Tashkent, Uzbekistan

Received May 11, 1999; in final form, November 10, 1999

Abstract—The lifetimes of electrons and holes in semiconductors were studied with respect to their recombination via excitons formed on isoelectronic traps. The curve of carrier lifetime versus trap concentration is nonmonotonic and exhibits a maximum. The effect is related to a sharp decrease in the concentration of major carriers under full compensation conditions and is accompanied by sharp increase in the semiconductor resistivity.

There is a vast number of papers devoted to investigations of the lifetimes of charge carries in semiconductors [1–4]. Until recently, it was commonly accepted that the lifetimes of both electrons (τ_n) and holes (τ_p) decrease monotonically with the concentration of deep impurity traps (N_t). However, more thorough investigations [5–8] of the process of recombination involving singly-charged [5–7] and doubly-charged [8] trapping centers showed that the dependence of τ_n and τ_p on N_t may be nonmonotonic, increasing by several orders in magnitude within certain interval of N_t.

Below, we will demonstrate that a similar phenomenon may take place under the conditions of electron–hole recombination via excitons formed on isoelectronic traps. Note that the isoelectronic traps and related exciton emission has been observed in many semiconductors widely used in modern optoelectronics (silicon carbide, gallium phosphide, etc.).

Using a relationship for the recombination rate derived in [2], the lifetimes of electrons (τ_n) and holes (τ_p) can be expressed as

$$\tau_n = \tau_{po}^* \frac{n + n_1^*}{n_o \Delta p/\Delta n + p} + \tau_{no}^* \frac{p + p_2^*}{n_o \Delta p/\Delta n + p} + \tau_{ex} \frac{\Delta n}{N_t}, \quad (1)$$

$$\tau_p = \tau_{po}^* \frac{n + n_1^*}{p_o \Delta n/\Delta p + n} + \tau_{no}^* \frac{p + p_2^*}{p_o \Delta n/\Delta p + n} + \tau_{ex} \frac{\Delta p}{N_t}. \quad (2)$$

Here, n_o and p_o are the equilibrium, and Δn and Δp are the excess (nonequilibrium) electron and hole concentrations; $n = n_o + \Delta n$, $p = p_o + \Delta p$; $\tau_{no}^* = 0.5\tau_{no}[1 + \exp(-E_{ex}/(kT))]$, $\tau_{po}^* = \tau_{po} + \tau_{ex} p_1/N_t$, E_{ex} is the energy released upon the exciton annihilation, $\tau_{no} = 1/(C_n N_t)$, $\tau_{po} = 1/(C_p N_t)$, C_n is the coefficient of electron trapping on a deep impurity level E_t, C_p is the coefficient of hole trapping on an exciton level E_h; τ_{ex} is the exciton lifetime; $n_1^* = 0.5n_1[1 + \exp(-E_{ex}/(kT))]$, $p_2^* = 0.5p_1[1 + \exp(-E_{ex}/(kT))]^{-1}$, and n_1 and p_1 are the statistical Shockley–Read factors.

A relationship between the concentrations of free electrons, holes, sallow donors (N_d) and negatively charged isoelectronic traps (N_t^-) is determined by the electroneutrality condition, with an expression for N_t^- having the form derived in [4]:

$$p + N_d = n + N_t^-,$$
$$N_t^- = N_t \times \frac{C_n C_p n p_2^* + C_n n \nu_t + C_p p_2 \nu_t'}{\nu_t [C_n(n + n_1^*) + C_p(p + p_2^*)] + C_n C_p (pn - n_i^2)]}. \quad (3)$$

The resistivity of a semiconductor is described by the formula $\rho = [q(\mu_n n + \mu_p p)]^{-1}$, where q is the electron charge and μ_n and μ_p are the mobilities of electrons and holes, respectively.

Estimates obtained using the above expressions for τ_{no}^*, τ_{po}^*, n_1^*, and p_1^* showed that $\tau_{no}^* \approx \tau_{no}$, $\tau_{po}^* \approx \tau_{po}$, $n_1^* \approx n_1$, and $p_2^* \approx p_1 = N_v \exp[(E_t - E_g)/(kT)] \ll n_1$. Accordingly, the lifetimes τ_n and τ_p are independent of the depth of the exciton level ($p_2^* \approx p_1$) and are determined by the position of the ground trap level ($n_1^* \approx n_1$). If the process of exciton annihilation is more delayed as compared to the electron exchange between levels of the isoelectronic trap and the nearest allowed bands, the third terms in equations (1) and (2) are greater than the two others and determine the lifetimes of electrons and holes. Accordingly, the τ_n and τ_p decrease monotonically with increasing N_t and grow linearly with Δn and Δp. This behavior is a manifestation of the exciton par-

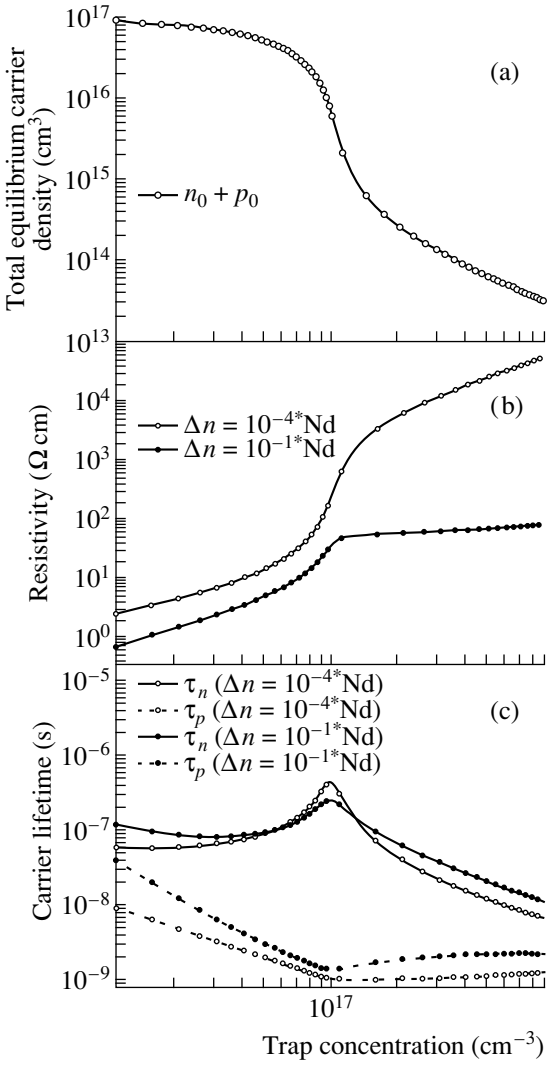

Fig. 1. The plots of (a) equilibrium carrier concentration $n_o + p_o$, (b) resistivity ρ, and (c) lifetimes of electrons τ_n and holes τ_p vs. isoelectronic trap concentration N_t at $T = 300$ K, $N_d = 10^{17}$ cm^{-3}, $\Delta n = 10^{-4} \times N_d$, and $\Delta n = 0.1N_d$.

ticipation in the process of the electron–hole recombination via isoelectronic traps.

The further analysis will be performed for the case when excitons annihilate at a higher rate as compared to that of the electron exchange between traps and allowed energy bands. The electron transition from the trap level to an exciton level is assumed not to make a decisive contribution to the carrier lifetimes τ_n and τ_p, so that the third term in equations (1) and (2) is always smaller than the first two. Accordingly, provided that deviations of the excess electron concentration Δn from the excess hole concentration Δp are small ($\Delta n/\Delta p \sim 1$) and the excitation levels are sufficiently low, the lifetimes τ_n and τ_p will increase for the equilibrium concentration of the major charge carriers sharply decreasing with growing N_t. This situation may take place under the conditions of compensation, whereby $N_t = N_d$. Here, a large fraction of the major carriers is trapped and their concentration drops sharply. This will result in a decrease of the recombination rate and a giant increase in the carrier lifetime.

Since the above effect is dependent on the equilibrium concentration of charge carriers, let us study the dependence of the sum $n_o + p_o$ on N_t using the electroneutrality condition (3) and the relationship $n_o p_o = n_i^2$. The numerical estimates were performed for GaP containing isoelectronic Zn–O traps. As is known, the process of recombination via these traps proceeds by binding electrons and holes into excitons [9] according to a mechanism proposed in [2]. The investigation was performed for $C_n \approx 10^{-10}$ cm^3/s, $C_p \approx 10^{-8}$ cm^3/s, $E_t = 0.3$ eV, $E_h = 0.036$ eV, $E_g = 2.26$ eV, $T = 300$ K, $N_t = 10^{16}$–10^{18} cm^{-3}, and $N_d = 10^{17}$ cm^{-3}. In the entire range of N_t and N_d values, the semiconductor conductivity type is the same, $n_o \gg p_o$.

The results of our calculations are presented in Fig. 1 (panel a). For $N_d > N_t$, we obtain $n_o \approx N_d$ and the main fraction of isoelectronic traps occur in the negatively charged state with $N_t^- \approx N_t \gg N_{og}^o, N_{oe}^o$, where N_{og}^o and N_{oe}^o are the concentrations of equilibrium neutral traps without and with exciton, respectively.

For $N_t = N_d$, the n_o value drops sharply (by several orders of magnitude) down to a level determined by thermal generation from a trap level characterized by the parameter n_1. This is accompanied by a sharp increase in the resistivity ρ (see Fig. 1, panel b) and the lifetimes of electrons τ_n and holes τ_p (panel c). The maximum values of ρ and τ_n are reached at a low excitation level ($\Delta n = 10^{-4} \times N_d$) and decrease with increasing Δn until a complete leveling at $\Delta n \geq N_d$ (see Fig. 1, panels b and c). This behavior is indicative of the fact that the semiconductor becomes sensitive to even low illumination intensity variations capable of changing the Δn and Δp values. These effects (see Fig. 1, panels a–c) can be used as experimental evidence of the full compensation in semiconductors.

An analysis of Fig. 1 (panel c) shows that the lifetime of holes monotonically decreases with increasing N_t, exhibits no maximum, and is lower by several orders of magnitude as compared to τ_n. This is explained by a difference in the excess concentrations of electrons and holes ($\Delta n > \Delta p$), as is readily seen upon dividing equation (1) by (2), which yields $\tau_n/\tau_p = \Delta n/\Delta p$.

It should be emphasized that the effects described above are significantly dependent on the depth of the ground trap level. Should this level be close to the conduction band ($n_1 \geq N_d$), no sharp changes in the sample resistivity and carrier lifetimes are observed at all. However, at a sufficiently large depth of the ground trap

level, the concentration of free carriers and the sample resistivity would drop (probably, in a nonmonotonic manner) by several orders of magnitude with increasing N_t.

Thus, the curve of charge carrier lifetimes versus isoelectronic trap concentrations can be nonmonotonic for the recombination process involving excitons. This phenomenon is related to a sharp drop in the carrier concentration under the conditions of full compensation ($N_d = N_t$) and is accompanied by sharp changes in the sample resistivity and other parameters depending on n_0 and p_0.

In conclusion, it should be noted that a similar phenomenon of the sharp increase in resistivity (by seven orders of magnitude) was experimentally observed for polycrystalline silicon [10]. Probably, that phenomenon can be also explained by the mechanism proposed above.

The author is grateful to A.Yu. Leĭderman and É.N. Tsoĭ for fruitful discussions and technical assistance.

REFERENCES

1. W. Shockley and W. Read, Phys. Rev. **87**, 835 (1952).
2. V. V. Evstropov and B. V. Tsarenkov, Fiz. Tekh. Poluprovodn. (Leningrad) **4**, 923 (1970).
3. P. T. Landsberg, *Recombination in Semiconductors* (Cambridge University Press, Cambridge, 1992), p. 595.
4. P. T. Landsberg, E. V. Kanaki, and S. Zh. Karazhanov, Uzbek. Fiz. Zh., No. 6, 52 (1997).
5. V. A. Kholodnov, Fiz. Tekh. Poluprovodn. (St. Petersburg) **30**, 1011 (1996).
6. A. A. Drugova and V. A. Kholodnov, Solid State Electron. **38**, 1247 (1995).
7. V. A. Kholodnov, Pis'ma Zh. Éksp. Teor. Fiz. **67**, 655 (1998).
8. V. A. Kholodnov and P. S. Serebrennikov, Pis'ma Zh. Tekh. Fiz. **23**, 39 (1997).
9. J. M. Dishman and M. DiDomeniko, Phys. Rev. B **1**, 3381 (1970).
10. J. Y. W. Seto, J. Appl. Phys. **46**, 5247 (1975).

Translated by P. Pozdeev

Technical Physics Letters, Vol. 26, No. 3, 2000, pp. 190–192. Translated from Pis'ma v Zhurnal Tekhnicheskoĭ Fiziki, Vol. 26, No. 5, 2000, pp. 23–30.

Features of the Long-Term Photo EMF Relaxation in a Heteroepitaxial ZnSe–GaAs Structure

L. V. Shekhovtsov, E. F. Venger, G. N. Semenova, Yu. G. Sadof'ev, N. E. Korsunskaya, M. P. Semtsiv, and S. Yu. Sapko

Institute of Semiconductor Physics, National Academy of Sciences of Ukraine, Kiev, Ukraine
Physical Institute, Russian Academy of Sciences, Moscow, Russia

Received August 6, 1999

Abstract—The spectral characteristics and transverse distribution of the photo emf were studied in a heteroepitaxial ZnSe–GaAs structure obtained by MBE on a zinc-stabilized GaAs(100) substrate surface. The spectral measurements revealed unusual manifestations of the long-term photo emf relaxation, whereby the amplitude of the spectral characteristic of the photo emf depends on the direction of wavelength variation of the exciting monochromatic light. Dependence of the amplitude and sign (phase) of the photo emf on the intensity of light absorbed in the sample can be explained by time variation of the effective lifetime of the electron–hole pairs and by a difference in the lifetime values between various layers of the structure. Resistivity gradients at the heterostructure interface exhibit a layer character. © *2000 MAIK "Nauka/Interperiodica".*

1. Introduction. Epitaxial ZnSe–GaAs heterostructures obtained by the method of molecular-beam epitaxy (MBE) find important applications, in particular, in the working elements of blue-green lasers [1]. An important task consists in determining the homogeneity of these structures, especially in the region of interface. A method capable of determining inhomogeneous doping or nonuniform distribution of the charge carrier lifetime in a sample is offered by measurements of the distribution of the bulk-gradient photo emf and its spectral characteristic [2–4].

As is known, the ZnSe films grown by MBE on GaAs substrates exhibit internal mechanical stresses caused by the lattice mismatch and by a difference of the thermal expansion coefficient between film and substrate [5]. Relaxation of these stresses leads to the formation of dislocations inhomogeneously distributed in the interfacial regions of both film and substrate. This is accompanied by a variation of the recombination parameters in these regions of the heterostructure. In addition, impurities from a near-surface substrate region diffuse during the growth into the boundary layer and bulk of the ZnSe film and affect the resistivity of the film. Note that the incorporated impurities may be also inhomogeneously distributed in the bulk.

Measurements of the bulk-gradient photo emf, which employ a monochromatic light probe moving along the interface of a heterostructure (e.g., ZnSe–GaAs), and the spectral characteristics of the photo emf provide a three-dimensional pattern of distribution of the impurity concentration and the lifetime of nonequilibrium (minority) charge carriers in the heterostructure.

2. Experiments and results. The experiments were performed using ZnSe–GaAs heterostructures comprising 2-μm-thick high-resistivity ZnSe films on semi-insulating 300-μm-thick GaAs substrates. The samples represented 15 mm long and 3 mm wide plates. The photo emf measurements were performed at 300 K.

Figure 1 (curve *1*) shows a spectral characteristic of the transverse photo emf in a ZnSe–GaAs heterostructure measured for a light intensity of $G = 1 \times 10^{14}$ quanta/(cm^2 s) in the entire excitation wavelength range studied. The measurements were performed with all the precautions necessary for the photoelectric measurements (the contacts were shadowed to eliminate the barrier-layer photoeffect, the size of the illuminated area was 5 mm). The samples were illuminated with a monochromated light modulated at 536 Hz. The primary beam was normally incident on the sample from the ZnSe film side. The photo emf was measured in a direction parallel to the sample surface.

The spectral characteristic of the photo emf exhibits characteristic maxima at $\lambda = 0.465$ μm ($h\nu = 2.67$ eV) and $\lambda = 0.885$ μm ($h\nu = 1.40$ eV) corresponding to the optical absorption edges of ZnSe and GaAs, respectively. In addition, there are broad maxima in the region of 0.5–0.7 μm, which can be related to periodic variations of the resistivity gradient in depth of a heterostructure.

Figure 2 shows the distribution curves of the bulk-gradient photo emf measured with a monochromatic light probe moving from one contact to another within the same area as that used for the spectral measurements. Here, curve *1* corresponds to the excitation wavelength $\lambda = 0.440$ μm ($h\nu = 2.82$ eV) and curves *2* and *3*, to $\lambda = 0.885$ μm ($h\nu = 1.40$ eV). The light probe

1063-7850/00/2603-0190$20.00 © 2000 MAIK "Nauka/Interperiodica"

had a diameter of 0.3 mm and was moved at a velocity of 0.025 mm/s. Curves *1* and *2* were measured at an incident light intensity of $G = 2 \times 10^{12}$ quanta/(cm^2 s), and curve *3*, at $G = 2 \times 10^{14}$ quanta/(cm^2 s). As seen from Fig. 2, the transverse photo emf distributions along the sample surface measured at $\lambda = 0.440$ and 0.885 μm (curves *1* and *2*, respectively) exhibit a rather small difference and the curves are qualitatively similar. However, the increase in the incident light intensity to $G = 2 \times 10^{14}$ quanta/(cm^2 s) results in a tenfold increase in the photo emf amplitude and in the inversion of the distribution measured at $\lambda = 0.885$ μm (cf. curves *2* and *3*). No such inversion was observed for the same change in the incident light intensity at $\lambda = 0.440$ μm.

3. Discussion of results. It is important to note that the alternating-sign distribution of photo emf (Fig. 2) was measured by the method of lock-in detection, while the spectral characteristics (Fig. 1) were measured without using this detector. For this reason, a change in the sign of the photo emf could not be detected during measurements at $\lambda = 0.885$ μm, although the intensity of the modulated incident light was as high as $G = 1 \times 10^{14}$ quanta/(cm^2 s).

As is known, the change in the lock-in detector signal sign corresponds to a 180° change in the signal phase. A primary reason for the sign change is the reversal of the direction of dopant concentration gradient in a sample. However, the experiment reveals gradual variation of the signal phase at a modulated light wavelength of $\lambda = 0.885$ μm when the light intensity G was increased from 2×10^{12} to 2×10^{14} quanta/(cm^2 s).

The obtained results can be interpreted within the framework of the concept of the recombination-drift barriers arising in strongly inhomogeneous semiconductor crystals [6].

A definite amplitude and phase of the experimentally measured photo emf signal correspond to some effective lifetime of the electron–hole pairs in the semiconductor sample. A change in the amplitude and sign (phase) of the signal depending on the wavelength of the probing monochromatic radiation (and, hence, on the optical absorption coefficient) implies variation of the effective lifetime in depth of the sample. This variation may be caused by a change in the recombination-drift barrier height in the heterostructure studied. In other words, this effect is indicative of a strong inhomogeneity of the ZnSe–GaAs heterostructure, showing a "layer" character in the regions of film and substrate adjacent to the interface. This conclusion is conformed by the presence of pronounced maxima in the region of 0.5–0.7 μm of the photo emf spectrum (Fig. 1).

An expression for the relaxation time of the nonequilibrium electron–hole pair concentration upon photoexcitation comprises two factors: $\tau = \tau_0 \exp(\varphi)$, where τ_0 is the lifetime of the electron–hole pairs in the absence of recombination barriers, $\varphi = E_{rec}/kT$, and E_{rec}

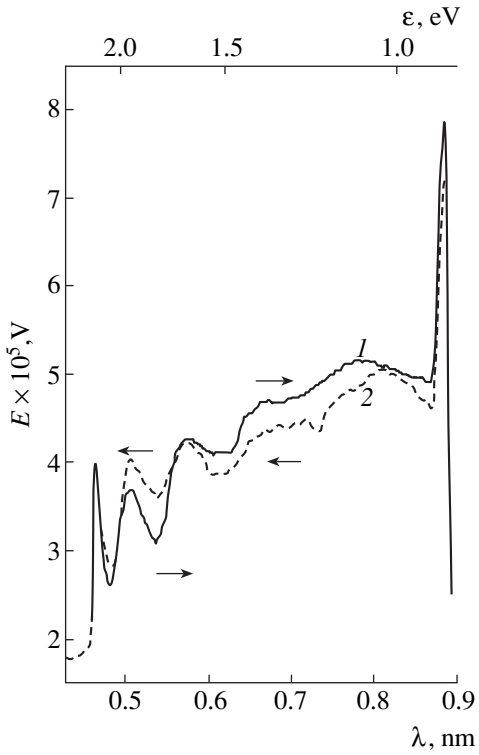

Fig. 1. Spectral characteristics of the transverse photo emf (E) measured in a ZnSe–GaAs heterostructure using a light probe with wavelength scanned (*1*) from 0.4 to 0.9 μm and (*2*) in the reverse direction. The incident light intensity $G = 1 \times 10^{14}$ quanta/(cm^2 s).

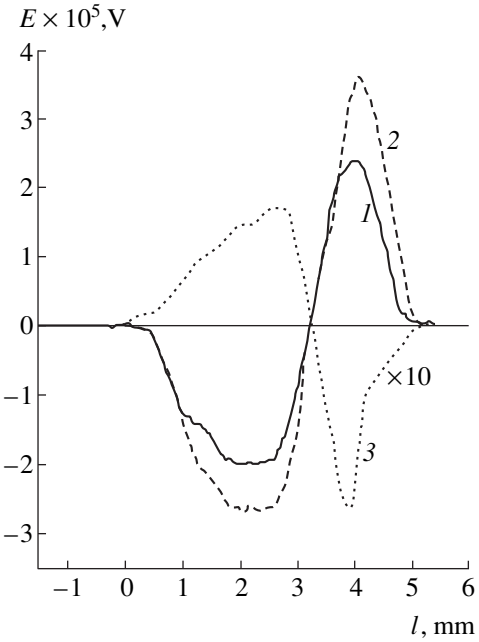

Fig. 2. Distribution of the transverse photo emf (E) across the surface (distance l) of a ZnSe–GaAs heterostructure probed with a modulated light from the side of epitaxial ZnSe film: (*1*) $\lambda = 0.44$ μm, $G = 2 \times 10^{12}$ quanta/(cm^2 s); (*2*) $\lambda = 0.88$ μm, $G = 2 \times 10^{12}$ quanta/(cm^2 s); (*3*) $\lambda = 0.88$ μm, $G = 2 \times 10^{14}$ quanta/(cm^2 s).

is the barrier height [6]. A change in the amplitude and sign of the measured photo emf can be related both to the variation of τ_0 in depth of the sample and to changes in the relaxation barrier height. In the case of ZnSe–GaAs heterostructures, both these factors may be operative. We are planning to study the nature of the layer structure of interfacial region of the ZnSe–GaAs heterostructure using the method of combined excitation of the semiconductor by modulated and nonmodulated monochromatic light beams [4, 8].

4. The effect of long-term photo emf relaxation. The presence of recombination-drift barriers in a semiconductor or a semiconductor heterostructure must lead to the phenomenon of long-term photo emf relaxation [6, 7]. Indeed, repeated measurement of the transverse photo emf spectrum, whereby the excitation wavelength (and, hence, the probe penetration depth) was varied from $\lambda = 0.4$ to 0.9 μm (Fig. 1, curve *1*) and then in the reverse direction (Fig. 1, curve *2*), showed that the photo emf amplitude at each particular λ value depends both on the rate of variation of the excitation wavelength (and, hence, the probe penetration depth and absorption coefficient) and on the direction of variation (increase from 0.4 μm versus decrease from 0.9 μm). This is a special form of manifestation of the effect of long-term photo emf relaxation.

When a monochromatic light probe is moved along the sample surface from one contact to another, the long-term photo emf relaxation gives rise to an additional emf component that is added (with the corresponding sign) to the bulk-gradient component [4, 8]. When the front of the absorbed light wave travels in depth of the sample, an analogous additional emf arises in the direction of light propagation, that is, from the illuminated to rear (dark) surface; the sign of the latter component also changes depending on the direction of the wave front propagation. Since there is a resistivity gradient component oriented along the illuminated surface, an additional emf would be generated (besides the main bulk-gradient component) between the sample contacts as a result of the relaxation of the nonequilibrium carrier concentration (distributed in depth of the sample) in the direction of their diffusion.

5. Methodological remark. It is important to note an important feature of the measurement of the transverse photo emf spectra such as those presented in Fig. 1. The amplitude difference of the photo emf spectra depends on the rate of variation of the excitation wavelength in the course of measurement. The experimentally measured signal is a sum of the bulk-gradient photo emf and an additional emf component related to the nonequilibrium electron–hole pair concentration gradient arising in the direction of the light wave front propagation, that is, in depth of the sample. Accordingly, an increase in the light propagation velocity would increase the amplitude of the latter component and its relative contribution to the total signal measured.

6. Conclusion. The results of investigation of the spectral characteristics of the transverse photo emf and its spatial distribution lead to the following conclusions.

The epitaxial ZnSe–GaAs heterostructures studied are featuring a nontraditional effect of the long-term relaxation of the transverse photo emf. This effect is manifested in the course of measurement of the photo emf spectrum under the conditions of continuous variation of the penetration depth of the excitation light probe in the sample.

The spectral characteristics of the photo emf displays a series of pronounced maxima both in the region of the fundamental absorption edge of ZnSe ($\lambda = 0.465$ μm, $h\nu = 2.67$ eV) and GaAs ($\lambda = 0.890$ μm, $h\nu = 1.40$ eV) and at the intermediate energies of the excitation light quanta. This fact is indicative of a variation of the resistivity gradient in depth of the sample, that is, of a layer character of the interfacial layers.

The observed variations in amplitude and sign of the photo emf depending on the excitation light intensity is apparently related to changes in the "effective" lifetime of the electron–hole pairs with time and to a difference in the lifetime values between various layers of heterostructure adjacent to the interface.

This work was supported by the Russian Foundation for Basic Research, projects nos. 2.4-362-98 and 2.4-621-98.

REFERENCES

1. S. V. Ivanov, A. A. Toropov, S. V. Sorokin, *et al.*, Fiz. Tekh. Poluprovodn. (St. Petersburg) **32**, 1272 (1998).
2. J. Tauc, *Photo and Thermoelectric Phenomena in Semiconductors* [in Russian] (Inostr. Lit., Moscow, 1962), pp. 1272–1276.
3. I. V. Baev and E. G. Valyashko, Fiz. Tverd. Tela (Leningrad) **7**, 2585 (1965).
4. L. V. Shekhovtsov, A. V. Sachenko, and Yu. M. Shvarts, Fiz. Tekh. Poluprovodn. (St. Petersburg) **29**, 566 (1995).
5. A. V. Kovalenko and A. Yu. Mekekechko, Fiz. Tverd. Tela (St. Petersburg) **35**, 2852 (1993).
6. M. K. Sheinkman and A. Ya. Shik, Fiz. Tekh. Poluprovodn. (Leningrad) **10**, 209 (1976).
7. V. S. Vavilov, P. K. Éfimiu, and J. E. Zardas, Usp. Fiz. Nauk **169**, 209 (1999).
8. L. V. Shekhovtsov, G. N. Semenova, E. F. Venger, *et al.*, Pis'ma Zh. Tekh. Fiz. **23**, 34 (1997).

Translated by P. Pozdeev

Technical Physics Letters, Vol. 26, No. 3, 2000, pp. 193–195. Translated from Pis'ma v Zhurnal Tekhnicheskoĭ Fiziki, Vol. 26, No. 5, 2000, pp. 31–36.

Quantum-Dimensional Lasers with Weak Temperature Dependence of the Output Power

S. V. Nalivko, A. A. Afonenko, and I. S. Manak

Belarus State University, Minsk, Belarus

Received August 9, 1999

Abstract—An injection laser configuration based on asymmetric quantum-dimensional heterostructure with inhomogeneous excitation of quantum wells (QW) is proposed. This configuration allows one to substantially reduce the temperature dependence of the output power. It is demonstrated that the relative variation of the lasing power at room temperature can be less than 1% per 10°C. © *2000 MAIK "Nauka/Interperiodica".*

Heating of the laser diode leads to a decrease in the output power of cw injection lasers [1]. The temperature stabilization of laser diodes is frequently achieved with the aid of Peltier elements [2]. The temperature dependence of the output power can be also decreased by means of the laser cavity modification [3, 4]. In this paper, we consider the effect attained in an asymmetric quantum-dimensional heterostructure with two inhomogeneously excited QWs. This effect allows the temperature dependence of the output power of the injection laser to be substantially reduced.

The active area of an asymmetric multilayer heterostructure includes quantum-dimensional layers of different thickness or composition. A regime of wavelength switching by means of variation of the pumping current was demonstrated for asymmetric heterostructures with two QWs [5]. Afonenko *et al.* showed the possibility of a bistable regime [6] and a regime of regular laser pulsations at widely spaced wavelengths [7]. In the described lasers, the generated radiation interacts with the charge carriers in all QWs. A special feature of the configuration of a heterostructure used for the temperature stabilization of the output power consists in selecting a spectrum of the energy levels of the QWs such that the radiation at a generated wavelength is amplified in one QW and virtually does not interact with charge carriers in the other QW (Fig. 1).

In the heterostructure considered as an example, QWs are separated by a wide barrier layer doped with acceptors. With a forward bias, the vacancies are transferred freely into QW 2, whereas the transfer of electrons into QW 1 is hindered because of the potential barrier emerging in the conduction band due to the barrier layer doping. Therefore, inhomogeneous excitation of the QWs is realized. As the temperature increases, a greater number of electrons can overcome the potential barrier. This leads to an increase in the coefficient η_1 of electron injection into the first QW and the corresponding decrease in the coefficient of injection of charge carriers into the second QW η_2. Therefore, a decrease in the output power of such a heterostructure, determined by the growth of spontaneous recombination in the amplifying QW caused by heating of the laser diode, can be compensated (even at a constant pumping

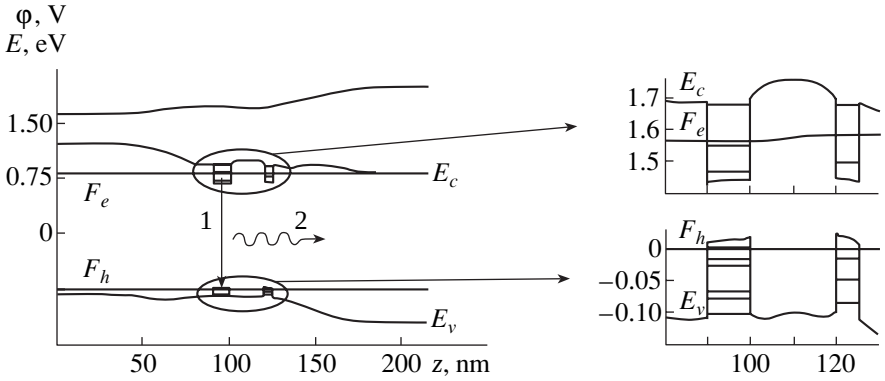

Fig. 1. Band diagram of an asymmetric quantum-dimensional heterostructure with two quantum wells in the system GaAs–$Al_xGa_{1-x}As$ at forward bias. F_e and F_h are the Fermi quasilevels for electrons and holes, respectively, φ is the electrostatic potential, E_c and E_v are the energies of the conductivity band bottom and the valence band top. Energy levels inside quantum wells are shown.

1063-7850/00/2603-0193$20.00 © 2000 MAIK "Nauka/Interperiodica"

current) by increasing the coefficient of injection of charge carriers into this QW.

An analysis of the output laser parameters is performed using a system of rate equations for 2D concentrations of electrons n_1 and n_2 in the corresponding quantum wells and 2D photon density S

$$\frac{dn_1}{dt} = \frac{j_{21}}{e} - R_1 - \nu_g G_1 S, \tag{1}$$

$$\frac{dn_2}{dt} = \frac{j - j_{21}}{e} - R_2, \tag{2}$$

$$\frac{dS}{dt} = \nu_g(G_1 - \kappa_l)S + \beta R_1. \tag{3}$$

Here, t is time; j is the pumping current density; j_{21} is the density of the barrier current in QW 1; R is the rate of spontaneous recombination; G_1 is the waveguide amplification coefficient; κ_l is the coefficient of the optical losses; ν_g is the group velocity of light in the heterostructure; β is the contribution of spontaneous transitions into the laser mode.

Under a stationary lasing regime, the gain G_1 is virtually equal to the coefficient of losses κ_l. The influence of temperature on the output power can be eliminated if the barrier current density j_{21} and the spontaneous recombination rate R_1 at the lasing threshold depend similarly on the temperature. For a certain temperature interval in the vicinity of the predetermined temperature T, this condition is presented mathematically as

$$\left.\frac{j_{21}}{e}\right|_T = R_1|_T + \nu_g \kappa_l S, \quad \left.\frac{dj_{21}}{edT}\right|_T = \left.\frac{dR_1}{dT}\right|_T. \tag{4}$$

For the quantitative analysis of the system of equations (1)–(3), one has to know the barrier current j_{21} as a function of the carrier concentration in QW and the temperature.

As the size of the barrier layer is comparable with the mean free path of electrons, the transfer of nonequilibrium charge carriers can be analyzed within the framework of the model of thermoelectron emission. In the limiting case of purely ballistic transfers, when electrons cross the potential barrier without collisions, the current through the barrier results from unbalance of the density of high energy electrons on two sides of the barrier [8]:

$$j_{21} = e\bar{v}_z N_{cd} \times \left\{\exp\left(\frac{F_{e2} - E_{cm}}{kT}\right) - \exp\left(\frac{F_{e1} - E_{cm}}{kT}\right)\right\}(1 + \gamma_n). \tag{5}$$

Here, $\bar{v}_z = \sqrt{kT/2\pi m_c}$ is the mean projection of the thermal velocity of electrons crossing the barrier; m_c is the effective mass of electron; E_{cm} is the maximum energy at the edge of the conduction band in the barrier; N_{cb} is the effective density of states in the barrier region; F_{e1} and F_{e2} are the Fermi quasilevels for electrons on both sides of the barrier; γ_n takes into account the contribution of tunneling. Expression (5) is written with regard to the fact that the distribution of electrons in the region of the potential barrier is nondegenerate.

Let us express the barrier current via the variables determining the level of excitation of QW. Calculations show that the Fermi quasilevel for holes in the region between QWs is virtually constant [9]. In the central part of the barrier, the relative position of the edge of the valence band and Fermi quasilevel for holes does not change with the level of excitation and is determined by the degree of doping of the barrier level. Hence, the increase of the difference between the Fermi quasilevels for electrons and holes ΔF in the barrier layer takes place completely at the expense of a change in the Fermi quasilevel for electrons. Then, an expression for the barrier current from QW 2 to QW 1 can be presented as [9]

$$j_{21} = j_{b0}\left\{\exp\left(\frac{\Delta F_2}{kT}\right) - \exp\left(\frac{\Delta F_1}{kT}\right)\right\}. \tag{6}$$

Here, ΔF_1 and ΔF_2 are the differences of Fermi quasilevels in the corresponding QWs. The electrophysical parameter of the structure j_{b0} depends on the temperature and can be determined by a calculation of the band diagram of the laser heterostructure by jointly solving

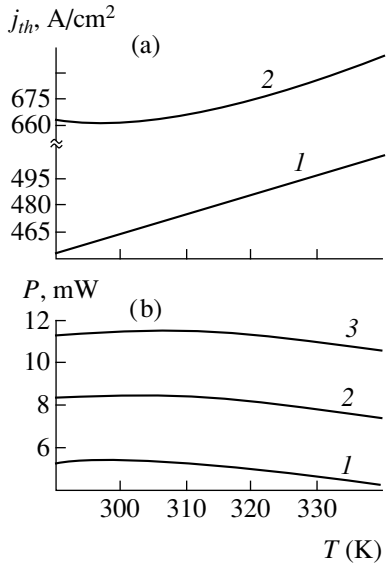

Fig. 2. Temperature dependencies (a) of the density of the threshold current j_{th} for quantum-dimensional heterostructure with (*1*) one and (*2*) two quantum wells and (b) of the output power P of a laser based on an asymmetric heterostructure with two quantum wells for different pumping current densities: (*1*) 0.8, (*2*) 0.9, and (*3*) 1.0 kA/cm^2.

the Poisson equation for the charge density and the continuity equations for the electron and hole currents.

Figure 2 shows the results of numerical calculations of the system of equations (1)–(3) with regard to the expression (6). The amplification coefficient and the recombination rate were calculated in the model of direct transitions with an allowance for broadening of the emission bands [10]. A minimum value of the threshold current j_{th} is achieved at a certain temperature that is determined by the parameters of the heterostructure. This value is about 1.5 times higher than that for a single QW because a part of the injected carriers recombines in the passive QW 2. As the temperature grows, the excitation of QW becomes more homogeneous and the curve of j_{th} for the multilayer heterostructure becomes similar to that for the case of a single QW. Optimum temperature depends slightly on the generated power P that is proportional to the photon density S. The value of P changes near the optimum by approximately 0.5% relative to the nominal value in the temperature range from 294 to 304 K, and by 5% in the range from 290 to 340 K. Note that, in the same temperature intervals, P of a laser with a single QW varies from 4 to 20%.

The effect described above can be realized if a multitude of quantum wells is used instead of a single QW as an amplifying medium. This proposed method of stabilization of the output power does not require an introduction of the additional (often worsening the reliability of the laser source) elements into the emitting unit.

REFERENCES

1. B. L. Gel'mont and G. G. Zegrya, Fiz. Tekh. Poluprovodn. **25**, 2019 (1991).
2. M. Ito and T. Kimura, IEEE J. Quantum Electron. QE-**17**, 796 (1981).
3. J. O'Gorman and A. F. J. Levi, Electron. Lett. **28**, 2091 (1992).
4. W. T. Tsang, F. S. Choa, R. A. Logan, *et al.*, Appl. Phys. Lett. **60**, 18 (1992).
5. S. Ikeda, A. Shimizu, and T. Hara, Appl. Phys. Lett. **55**, 1155 (1989).
6. A. A. Afonenko, V. K. Kononenko, and I. S. Manak, Pis'ma Zh. Tekh. Fiz. **19**, 35 (1993).
7. A. A. Afonenko, V. K. Kononenko, and I. S. Manak, Pis'ma Zh. Tekh. Fiz. **20**, 57 (1994).
8. M. Shur, *GaAs Devices and Circuits* (Plenum, New York, 1987).
9. A. A. Afonenko, V. K. Kononenko, and I. S. Manak, Preprint LAMP/95/6/ICTP, Trieste (1995).
10. V. K. Kononenko, I. S. Manak, S. V. Nalivko, *et al.*, Zh. Prikl. Spektrosk. **64**, 221 (1997).

Translated by A. Chikishev

Technical Physics Letters, Vol. 26, No. 3, 2000, pp. 196–198. Translated from Pis'ma v Zhurnal Tekhnicheskoĭ Fiziki, Vol. 26, No. 5, 2000, pp. 37–41.

Modeling of the Dendrite Shape Variation with Applied Electric Field Strength in Poly(ethylene)

M. M. Rezinkina

Received June 2, 1999; in final form, October 14, 1999

Abstract—A method for mathematical modeling of the electrophysical processes involved in the electrical aging of polymeric dielectrics under the action of stress is described. An example of the calculation of the defect structure evolution in space and time in a poly(ethylene) insulator is presented. © *2000 MAIK "Nauka/Interperiodica".*

Mathematical modeling of the electrical aging of solid dielectrics is usually performed by methods of the fractal theory [1]. This approach consists essentially in conventionally dividing a material into microvolumes of conducting and insulating phases, depending on whether a given microvolume exhibits breakdown or not. It is assumed that breakdown in separate regions has a stochastic character, with the probability determined by the strength of a local electric field. An advantage of using the fractal theory for a description of the electric breakdown in dielectrics is the allowance for the statistical nature of this process. However, the existing fractal models are not based on experimental data about the properties of particular dielectrics and processes involved in various stages of the breakdown development. Nor does this description allows the breakdown development to be studied on a real time scale.

In this work, the numerical modeling of the electrical aging in polymeric dielectrics was performed with an allowance for some specific features of particular insulating materials, using an approach described in [2]. The insulator under consideration was divided into cells of a parallelepiped shape, with the properties of the medium inside each cell assumed constant. Then, the distribution of the electric field strength **E** in the material was calculated and the resulting $|\mathbf{E}|$ values were used to determine the breakdown probability for each of the cells. The probability for a cell to convert from an insulating to conducting phase is proportional to the electric field strength, which is a traditional course of action in applying the fractal theory to modeling the breakdown in solid dielectrics.

In order to take into account experimental data characterizing the electric properties of a particular dielectric material, the probability of breakdown in a jth cell was determined in terms of a random quantity, the cell lifetime t_j depending both on $|\mathbf{E}_j|$ and on the material properties, rather than directly in terms of the $|\mathbf{E}_j|$ value. The t_j values were obtained with the aid of a random number generator with a distribution function coinciding with the experimental distribution of times to breakdown in microvolumes of the dielectric under consideration at a given level of the electric field strength. The generator was started with a random number K_j fixed for each cell. These numbers model the random distribution of dielectric properties in a given sample of an insulating material.

In the first step, we have selected a minimum lifetime among the values predicted for all elementary cells, followed by the lifetimes differing from the first one to within a preset computation accuracy. The magnitude of the current time step Δt_n was taken equal to this minimum lifetime difference $\Delta t_n = \min\{t_n\}$, where n is the time step number. The current time was determined by adding one step to the preceding time instant $t_{n+1} = t_n + \Delta t_n$. The cells with the minimum time to breakdown were considered as converted from insulating to conducting phase, which was manifested by changing the corresponding permittivities and conductivities for other values. The algorithm was repeated in the next time step.

Under the action of applied voltage, some polymeric dielectrics such as poly(ethylene) (PE) exhibit the formation of tree-like cavities—dendrites—having a diameter of 5–10 μm and a fractal structure. The breakdown of a cell implies that this microvolume has transformed into a cavity filled with a gas. It was reported that the surface resistance of the cavity walls in PE dropped from 10^{17} to 10^9 Ω upon a 1-h exposure to electric field with a strength of E = 5 kV/mm. The broken cells with a wall resistance of 10^{17} Ω are nonconducting. When the resistance of cells decreases to 10^{10}–10^9 Ω, their conductivity sharply grows to exceed by several orders of magnitude the conductivity of cells containing PE.

The period of time required for a broken cell to convert from nonconducting to conducting state was calculated using a well-known method [4], according to which the degradation times of solid dielectrics t_1 and t_2 at different voltages U_1 and U_2 are inversely propor-

1063-7850/00/2603-0196$20.00

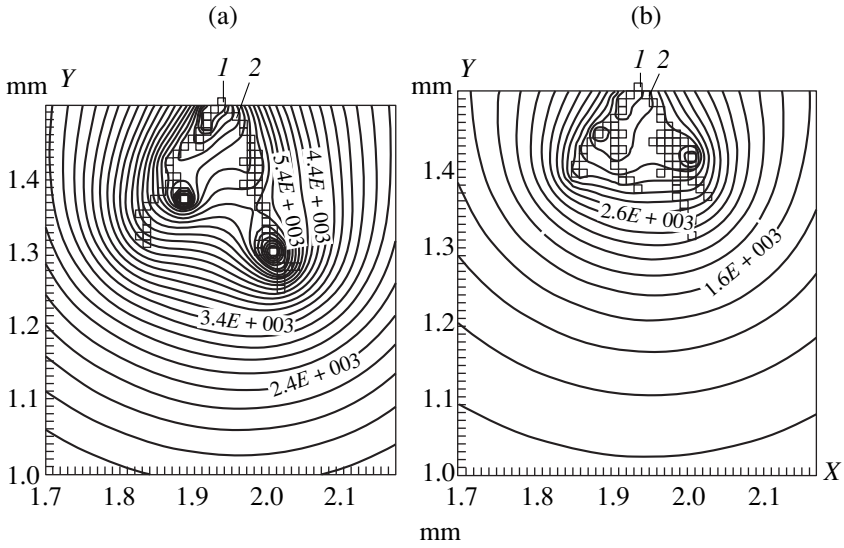

Fig. 1. The patterns of equipotential lines (voltages indicated in V) around a dendrite formed during the breakdown in PE at U = 9 kV (a) and 6 kV (b): (*1*) point electrode; (*2*) dendrite projection onto the cross-section plane Z = const passing through the point electrode.

tional to these voltages with an exponent r depending on the particular material: $t_1/t_2 = (U_2/U_1)^r$. The r values experimentally determined for microvolumes of a monolithic PE fall within r = 4–5. This feature of PE, not taken into account in [5], must be included into consideration in modeling the time evolution of dendrites.

The initial data for modeling were taken from the results of experiments devoted to determination of the time to breakdown in microvolumes of monolithic PE [6]. The strength of a three-dimensional electric field was calculated by the lattice-point (finite difference) method similar to that described in [7].

The patterns of calculated equipotential lines in a cross section Z = const in the vicinity of dendrites developed in PE in a "point–plane" electrode system are depicted in the Fig. 1. The field strength distributions were obtained by mathematical modeling using the approach described above. This particular electrode system was selected because a large body of experimental data were available on the electric aging of PE insulation in this very configuration. A distance between point and plane was 1.5 mm and the point potential was U = 9 kV (dendrite development time 1 min, see Fig. 1a) or 6 kV (dendrite development time 10 min, see Fig. 1b). Distribution of the dielectric properties of PE samples (represented by the distribution of random numbers K_j of the cells) in these numerical experiments was the same. This fact accounts for a certain similarity of the dendrites observed, while a difference in their spatial structures reflect the qualitative changes related to the application of stronger or weaker fields (voltages).

The results of our experimental investigations show that keeping a PE sample under an applied voltage of 6 kV is accompanied by a slow growth of dendrites. The growth process is accompanied by thickening of the dendrite branches and by increasing fractal dimensionality (D ~ 1.4–1.5), which implies an increase in the dendrite branching density. The application of a higher voltage (U = 9 kV) results in the acceleration of dendrite growth, whereby the interelectrode gap is covered within a time period of no longer than a few tens of minutes. Note that the dendrite branches still exhibit fine ends and the fractal dimensionality of this dendrite (D ~ 1.1–1.2) corresponds to a weakly branched structure. Thus, the proposed approach allowed all of these phenomena to be modeled.

If the dendrite growth is modeled with neglect of the effect of increasing conductivity of the dendrite walls, the structures grown at various voltages have the same fractal dimensionality and differ only by the times of dendrite development. For the adequate modeling of changes in the spatial structure of dendrites grown at higher or lower field strengths, the procedure must take into account the experimentally established dependence of the conductivity of dendrite channel walls on the applied voltage. At a higher voltage (U = 9 kV), the conversion of broken cells back into the state of high surface conductivity takes a rather short time and is accomplished before breakdown in the next cell. Therefore, the entire dendrite can be considered as conducting and, hence, the maximum electric field strength is developed at the ends of dendrite branches growing predominantly in longitudinal direction (see Fig. 1a). At a lower voltage (U = 6 kV), the surface resistance of broken cells decreases with a delay of several time steps. As a result, not all of the dendrite structure is conducting and the maximum electric field strength can be developed both at the branch ends and in other regions. This fact accounts for the dendrite growth both in the

longitudinal direction (across the gap) and the development of new runners in the middle regions of branches (see Fig. 1b). Thus, the dendrite branches increase in thickness, the electric field strength drops, and the longitudinal dendrite growth (elongation) slows down. The times of dendrite development and the fractal structures of modeled dendrites show good agreement with the experimental data.

REFERENCES

1. *Fractals in Physics*, Ed. by L. Pietronero and L. Tosatti (North-Holland, Amsterdam, 1986).
2. V. V. Konotop, O. L. Rezinkin, and M. M. Rezinkina, Zh. Tekh. Fiz. **66**, 198 (1996).
3. P. Morshuis, in *The 9th International Symposium on High-Voltage Engineering, August 28–September 1, 1995, Graz*, Vol. 5, p. 5644.
4. W. Starr and H. Endicott, IEEE Trans. PAS **55** (1961).
5. M. M. Rezinkina, in *The 10th International Symposium on High-Voltage Engineering, August 25–29, 1997, Montreal*, Vol. 2, p. 383.
6. V. V. Konotop, O. L. Rezinkin, M. M. Rezinkina, *et al*., Prib. Tekh. Éksp. No. 4, 191 (1995).
7. M. M. Rezinkina and O. L. Rezinkin, Élektrichestvo, No. 7, 62 (1995).

Translated by P. Pozdeev

Technical Physics Letters, Vol. 26, No. 3, 2000, pp. 199–201. Translated from Pis'ma v Zhurnal Tekhnicheskoĭ Fiziki, Vol. 26, No. 5, 2000, pp. 42–48.

Heterogeneous Effect in Carbonized Porous Silicon

B. M. Kostishko, Sh. R. Atazhanov, I. P. Puzov, S. Ya. Solomatin, and Yu. S. Nagornov

Ul'yanovsk State University, Ul'yanovsk, Russia

Received July 12, 1999

Abstract—The spectra of photoluminescence from carbonized porous silicon were measured upon the anodic polarization of samples in an oxidative electrolyte. A significant increase in the intensity of a blue-green emission band was observed and attributed to a change in parameters of the silicon–silicon carbide heterostructure. In addition, the carbonized porous silicon exhibits effective electroluminescence in an oxidizing electrolyte. © *2000 MAIK "Nauka/Interperiodica".*

The prospects of micro- and optoelectronics are determined to a considerable extent by the development of new materials compatible with the silicon technologies. Although porous silicon (por-Si) is still considered as a candidate, no competitive light-emitting devices have been yet created based on this material. This is primarily related to nonreproducible parameters of por-Si [1, 2], which have proved to depend significantly on the conditions of sample preparation, storage, and operation. Another impeding factor is a comparatively low quantum efficiency of LEDs implementing por-Si, which is typically not exceeding 10^{-3}% in the structures with solid electrodes [3].

A markedly higher (by two orders of magnitude [4]) luminescence efficiency was observed for the electroluminescence of por-Si in electrolytes, which was explained by the ambipolar injection and a better contact of liquid medium with the surface of quantum filaments. Unfortunately, short emission time, complicated design, and large dimensions of the electroluminescent structures hinder implementations of this phenomenon into practice. However, this effect can be used for modification of the properties of porous light-emitting structures.

The purpose of this work was to study the pattern of changes in the photoluminescence (PL) spectra of carbonized por-Si (CPS) [5, 6] upon the anodic polarization in an oxidizing electrolyte.

The experiments were performed with CPS samples prepared using the following procedure. A phosphorus-doped silicon wafer (ρ = 32 Ω cm) was subjected to electrochemical etching according to a standard technology to obtain a 30-μm-thick layer of porous silicon. The etching was carried out for 40 min at a current density of 20 mA/cm^2. In this regime, the electrochemical etching proceeds in the upper region of the ascending branch of the current–voltage characteristic of the silicon–electrolyte system. According to [7], the etched silicon structure is characterized by the formation of pores of the first morphology type. Then, the porous silicon samples were annealed in a carbon-containing medium and simultaneously doped with P or Ga atoms [5, 6]. The doping with phosphorus (to a final dopant concentration of 3×10^{18} cm^{-3}) was effected using gaseous P_2Cl_5 as a source. Gallium from a solid source was introduced to a final concentration of 5×10^{17} cm^{-3}.

Figure 1 (curves *1* and *3*) shows the PL spectra of CPS samples measured immediately upon the carbonization treatment. According to the results of investigations reported in [5, 6], the high-temperature process of porous silicon carbonization under specified conditions leads to the formation of quantum dots formed by sili-

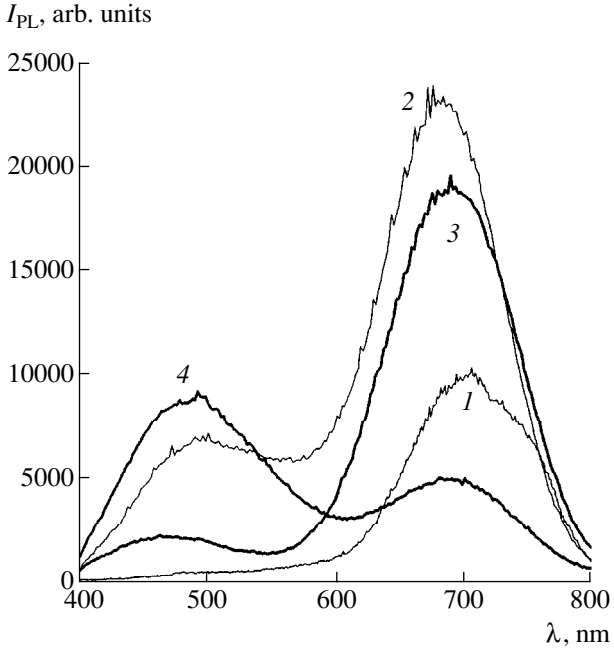

Fig. 1. The PL spectra of CPS samples (*1*, *2*) carbonized for 2 min at 1000°C and doped with phosphorus and (*3*, *4*) carbonized for 4 min at 1200°C and doped with gallium: (*1*, *3*) without subsequent electrochemical treatment; (*2*, *4*) upon 30-min anodic polarization.

1063-7850/00/2603-0199$20.00 © 2000 MAIK "Nauka/Interperiodica"

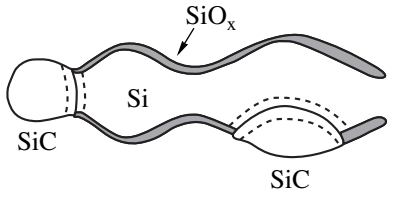

Fig. 2. Schematic diagram illustrating the formation of heterojunctions in CPS. Dashed lies indicate boundaries of the space-charge regions.

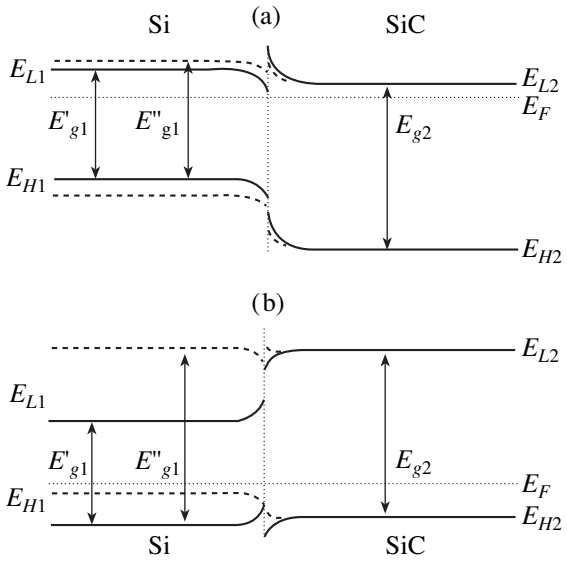

Fig. 3. Variation of the energy band profiles of (a) *n–n* and (b) *p–p* heterojunctions in CPS upon electrochemical oxidation. Dashed lines show changes caused by a decrease in the size of silicon filaments and the corresponding increase in the bandgap.

con carbide in a cubic modification (3C–SiC). This was confirmed by structural data of the X-ray diffraction and Raman spectroscopy, and by the Auger electron spectroscopy data on variation of the density of states in the valence band of CPS. The presence of two emission bands in the PL spectrum was previously explained by the radiative recombination of the electron–hole pairs proceeding independently in the quantum-dimensional silicon particles and in the silicon carbide grains. The first mechanism was considered as responsible for the longwave PL with λ = 680–750 nm, and the latter, for the shortwave emission at λ = 500–510 nm.

The same CPS samples were used to study the electroluminescence in a liquid phase. For this purpose, the samples were subjected to anodic polarization at a current density of 50 mA/cm^2 in an electrolyte comprising a mixture of 42% H_2SO_4, 18% acetone, and 40% H_2O. Acetone was added in order to increase wetting of the sample surface and decrease the cell resistance [4]. As a result of the anodic polarization, the sample exhibited blue electroluminescence with a characteristic emission time of the order of a few minutes. The surface structure of CPS samples was markedly affected by the anodic polarization. This was manifested by a change in color of the sample and by a 60–70-fold increase in the size of characteristic rectangular formations on the sample surface.

The obvious modification of the porous layer structure, caused by the electrochemical treatment, also markedly changed the shape of the PL spectra of CPS, as seen from the spectra presented in Fig. 1 (curves *2* and *4*). In the case of silicon doped with phosphorus, the CPS samples upon anodic polarization exhibit a considerable increase in PL intensity in the region of a blue-green emission line that was almost indistinguishable in the initial samples. It was found that the PL spectra of CPS are well described by a sum of two Gaussian lines:

$$I_{\mathrm{PL}} = A_{\mathrm{GB}}\exp\left(-\frac{(\lambda-\lambda_{\mathrm{GB}})^2}{2\sigma_{\mathrm{GB}}^2}\right) + A_{\mathrm{R}}\exp\left(-\frac{(\lambda-\lambda_{\mathrm{R}})^2}{2\sigma_{\mathrm{R}}^2}\right),$$

where A, λ, and σ are the amplitude, position (wavelength), and dispersion of the blue-green (subscript GB) and red (subscript R) spectral components.

An analysis of the results of approximation of the experimental PL spectra using the equation showed that the ratio of amplitudes of the red and blue-green lines for the phosphorus-doped samples decreased by a factor of about five upon the anodic polarization. Even more dramatic changes were observed in the gallium-doped CPS samples, where intensity of the shortwave component upon the anodic polarization increased so as to became two times that of the longwave line.

We believe that changes observed in the PL spectra of CPS can be explained by the fact that carbonization leads to the formation of heterojunctions between the 3C–SiC quantum dots and the cores of quantum filaments, such as depicted in Fig. 2. Apparently, doping the samples with phosphorus in the course of the carbonization treatment results in the formation of isotypic *n–n* heterojunctions, while the doping with gallium gives rise to isotypic *p–p* heterojunctions (Fig. 3). In the latter case, the hole conductivity of silicon in the regions adjacent to quantum dots in the silicon carbide phase is caused by overcompensation of the dopant.

Upon the space-charge region (SCR) formation, PL in the regions spaced from SCR by a distance shorter than the diffusion length of minority carriers is determined by the heterojunction parameters, primarily by the magnitude and direction of the built-in electric field. According to the data of Raman spectroscopy, the size of the silicon carbide grains in the CPS samples studied was 45–52 μm. This estimate implies that the PL from Si and SiC regions cannot be considered as independent processes.

Indeed, an electron–hole pair generated in the SiC phase of a nanodimensional heterojunctions will be

separated by electric field of the SCR (Fig. 3). As a result, the minority charge carriers are injected predominantly into the narrow-bandgap region of the single-crystal silicon. The major carriers are injected from the opposite side. As a result of this process, the number of radiative recombination events per unit time in the silicon quantum-dimensional regions would tend to increase, while that in the silicon carbide regions would decrease.

After the electrochemical treatment of CPS in a strong oxidizing medium (sulfuric acid), the dimensions of silicon nanoparticles would decrease as a result of the oxide formation. This is confirmed by a significant (20–25 nm) shift of λ_R. Note that the position of the blue-green line remains virtually unchanged. According to [8], this shift in the position of maximum of the red emission line corresponds to the size of the single-crystal silicon particles decreasing from 9.0 to 8.0 nm. This change in the bandgap and the size of silicon particles must modify the energy band profile in the heterojunction. One possible variant is presented in Fig. 3, where the energy band diagram depicted by dashed lines is constructed assuming that an increase in the difference between the lowest unoccupied (E_L) and highest occupied (E_H) states in silicon nanocrystals is accompanied by a shift of the Fermi level. The latter may be caused by changes in the atomic composition of groups passivating the surface of quantum filaments, which leads to a change in the density of states in the valence band [9, 10]. It should be recalled that the schematic energy diagram of the heterostructure presented in Fig. 3 is simplified and assumes the absence of charged states at the interface [11].

The modification of parameters of the *n–n* heterojunction depicted in Fig. 3a leads to a decrease in the flux of holes injected into silicon nanocrystals and an increase in the intensity of PL in the region of the blue-green line. As for the *p–p* heterojunction (Fig. 3b), the situation apparently corresponds to the case when the Fermi level in silicon shifts below that in silicon carbide. This leads to reversal of the direction of electric field in the SCR. As a result, the light-induced minority carriers are injected from Si into SiC and the intensity of the red emission component drops below that of the blue-green line.

Thus, we have demonstrated that the photoluminescence in CPS is a process occurring in a conjugated system of heterojunctions formed between the quantum-dimensional regions in silicon and silicon carbide. Parameters of these heterojunctions can be controlled by means of anodic polarization in an oxidizing electrolyte. This provides an opportunity to modify the PL spectra of carbonized porous silicon. In addition, we have observed, for the first time, the phenomenon of effective electroluminescence from carbonized porous silicon.

This work was supported by the Russian Foundation for Basic Research (project no. 99-02-17903) and by grants according to the “Russian Universities–Basic Research” and “Radio Engineering” programs of the Ministry of Higher Education of the Russian Federation.

REFERENCES

1. A. G. Gullis, L. T. Canham, and P. J. D. Calcott, J. Appl. Phys. **82**, 909 (1997).
2. I. M. Chang, G. S. Chuo, D. C. Chang, *et al.*, J. Appl. Phys. **77**, 5365 (1995).
3. C. Peng and P. M. Fauchet, Appl. Phys. Lett. **67**, 2515 (1995).
4. D. N. Goryachev, O. M. Sreseli, and L. V. Belyakov, Fiz. Tekh. Poluprovodn. (St. Petersburg) **31**, 844 (1997).
5. B. M. Kostishko, Sh. R. Atazhanov, and S. N. Mikov, Pis’ma Zh. Tekh. Fiz. **24**, 24 (1998).
6. B. M. Kostishko, Sh. R. Atazhanov, S. N. Mikov, *et al.*, Pis’ma Zh. Tekh. Fiz. **25**, 13 (1999).
7. É. Yu. Buchin and A. V. Prokaznikov, Pis’ma Zh. Tekh. Fiz. **23**, 80 (1997).
8. T. Takagahara and K. Takeda, Phys. Rev. B **46**, 15578 (1992).
9. G. Zajac and S. D. Bader, Phys. Rev. B **26**, 5688 (1982).
10. B. M. Kostishko, A. M. Orlov, S. N. Mikov, *et al.*, Neorg. Mater. **31**, 444 (1995).
11. B. L. Sharma and R. K. Purokhit, *Semiconductor Heterojunctions* [in Russian] (Sov. Radio, Moscow, 1979).

Translated by P. Pozdeev

Technical Physics Letters, Vol. 26, No. 3, 2000, pp. 202–205. Translated from Pis'ma v Zhurnal Tekhnicheskoĭ Fiziki, Vol. 26, No. 5, 2000, pp. 49–56.

Weak Variband Surface Layers as an Effective Means of Protection from the Surface Recombination of Photoexcited Carriers in Infrared Threshold CdHgTe Photoresistors

V. A. Kholodnov and A. A. Drugova

Orion, Research and Production Corporation, Moscow, Russia

Received July 19, 1999

Abstract—It is demonstrated that variband near-surface layers with even a small composition gradient can provide ultimate photomodulation (corresponding to the absence of the surface recombination) of the conductivity of thin CdHgTe samples used for manufacturing threshold photoresistors (including those of the SPRITE type) for the wavelengths λ = 8–12 μm and λ = 3–5 μm. This is explained by the formation (even in weak variband layers) of a special profile of the photoexcited carrier distribution that inhibits their diffusion to the surface. As is known, the introduction of the near-surface variband layers with a small composition gradient must not lead to any substantial increase in the number of defects in the sample. © *2000 MAIK "Nauka/Interperiodica".*

It is known [1] that the optimum thickness of a photoresistor along the direction of light propagation (Fig. 1a) is $W_0 \cong 1/\gamma$. In CdHgTe normally $1/\gamma < L$, where γ is the absorption coefficient and L is the ambipolar diffusion length of nonequilibrium carriers. Under these conditions, the carriers photoexcited in the bulk diffuse to both irradiated and shadow surfaces and disappear because of the surface recombination that is virtually inevitable [1]. Blocking of this channel of losses of the photocarriers is one of the most important problems encountered in the development of highly effective HgCdTe photoresistors, including those of the SPRITE type, for the wavelengths 8–12 and 3–5 μm. It is clear [2–5] that the introduction of the near-surface variband layers *1* and *2* on the irradiated and shadow sides of the working area *3* of the sample (Fig. 1a) with rather strong variband field E_{var} (of the appropriate orientation) would inhibit the diffusion of photocarriers to the surfaces ($x = 0$ and $x = W$, Fig. 1). Unfortunately, it is well known that a large gradient of the mole composition leads to the formation of a large number of defects in the sample. Recently, we reported [6, 7] on the possibility of blocking of the surface recombination by means of weak variband near-surface layers with

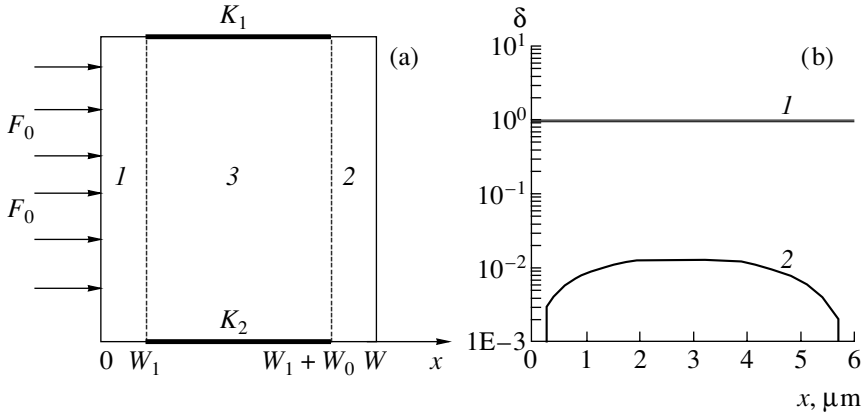

Fig. 1. (a) The scheme of the photoresistor and (b) the dependence of $\delta \equiv \Delta p/\Delta p_0$ on $x(b)$, where F_0 is the density of the incident light flux, K_1 and K_2 are current contacts, Δp_0 is the concentration of photovacancies in a normal photoresistor (without near-surface variband layers *1* and *2*) in the absence of the surface recombination (at the points $x = W_1$ and $x = W_1 + W_0$). The sample comprises the working area *3* (with the bandgap E_{g0}= 0.1 eV, the thickness is W_0 = 6 μm, and the variband layer thicknesses $W_1 = W_2$ = 2 μm), a photoresistor *1* with $\xi \equiv |\partial E_g/\partial x|$ = 1 – 100 eV/cm, and a normal photoresistor *2* with infinitely high rate of the surface recombination at the points $x = W_1$ and $x = W_1 + W_0$ (the optical wavelength is λ = 10.6 μm).

1063-7850/00/2603-0202$20.00 © 2000 MAIK "Nauka/Interperiodica"

small composition gradient and, hence, small number of defects. Below, we present substantiation of such a possibility.

In order to evaluate the effect under study (Fig. 1b), we use a schematic diagram of the sample shown in Fig. 1a (material of the *n* type; the equilibrium electron concentration n_e and the electron affinity are constant everywhere [8, 9]).

The photon absorption starts and ends at the points (Fig. 2):

$$x_1 = W_1 - \frac{h\nu - E_{g0}}{\xi} \text{ and } x_2 = W_1 + W_0 + \frac{h\nu - E_{g0}}{\xi}, \quad (1)$$

where $\zeta = |\partial E_g/\partial x| = \text{const}$ for $0 < x < W_1$ and $W_1 + W_0 < x < W = W_1 + W_0 + W_2$, $E_g(x)$ is the band gap, and $E_g(x) = E_{g0} = \text{const}$ for $W_1 < x < W_1 + W_0$.

Due to multiple reflections of the light beam, the specific rate of the photogeneration of charge carriers is:

$$g(x) = \alpha_1\gamma\exp(-\gamma x) + \alpha_2\gamma\exp(\gamma x), \quad (2)$$

where

$$\alpha_1 = \frac{(1-R)F_0\exp(\gamma x_1)}{1-R^2\exp[-2\gamma(x_2-x_1)]}, \quad \alpha_2 = R\exp(-2\gamma x_2)\alpha_1, \quad (3)$$

R is the reflection coefficient for the irradiated ($x = 0$) and unirradiated ($x = W$) surfaces, and F_0 is the density of the incident light flux (Fig. 1a). The function $\gamma(\lambda)$ can be determined from the known empirical relationship [10]:

$$\gamma(\lambda) = 1.7\times10^4\sqrt{\frac{1}{\lambda}-\frac{1}{\lambda_0}}, \quad \lambda_0 = 1.24/E_{g0}, \quad (4)$$

where γ is in 1/cm, λ is in μm, and E_{g0} is in eV. Consider the worst situation when the rate of the surface recombination is so high that the concentration of the nonequilibrium vacancies Δp and electrons Δn at the surface is equal to zero:

$$\Delta n(0) = \Delta p(0) = \Delta n(W) = \Delta p(W) = 0. \quad (5)$$

In a linear approximation with respect to g, which is valid in the case of weak illumination,

$$I_{ph}^{(n)} = q\mu_n n_e E_{ph} + qD_n\frac{d\Delta n}{dx},$$
$$I_{ph}^{(p)} = q\mu_p(p_e E_{ph} + E_{\text{var}}\Delta p) - qD_p\frac{d\Delta p}{dx}, \quad (6)$$

where $I_{ph}^{(n)}$ and $I_{ph}^{(p)}$ are the densities of the photocurrents of electrons and vacancies, respectively; $p_e(x)$ is the equilibrium concentration of vacancies; μ_n, μ_p and D_n, D_p are the mobilities and diffusion coefficients of electrons and vacancies, respectively; $E_{\text{var}} = -(1/q)(\partial E_g/\partial x)$ [2, 5]; $E_{ph}(x)$ is the electric field intensity caused by deviation of the carrier concentrations from their equilibrium values as a result of the photogeneration (photoinduced field); q is the charge of electron. The quantities $I_{ph}^{(p)}$, $I_{ph}^{(n)}$, and E_{ph} must meet macroscopic equation of currents continuity and macroscopic Poisson equation [1, 11–15]:

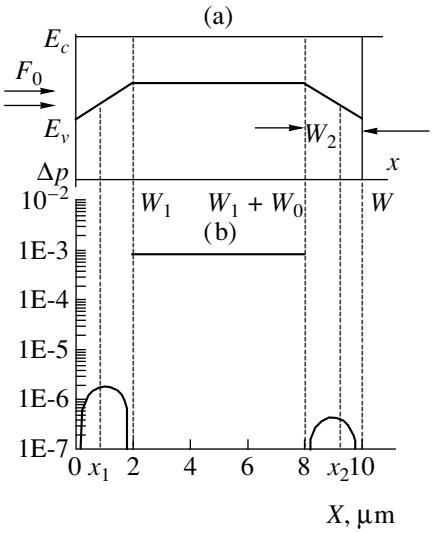

Fig. 2. (a) Band diagram and (b) the dependence of Δp on x for $F_0 = 1\ \text{cm}^{-2}\ \text{s}^{-1}$. E_c and E_v are the energies of the bottom of the conductivity band and the top of the valence band, respectively; $E_{g0} = 0.1$ eV, $\lambda = 10.6$ μm, $W_0 = 6$ μm, $W_1 = W_2 = 2$ μm.

$$\frac{dI_{ph}^{(p)}}{dx} = q(g - R_{in}), \quad \frac{dI_{ph}^{(n)}}{dx} = q(R_m - g), \quad (7, 8)$$

$$\frac{dE_{ph}}{dx} = \frac{4\pi q}{\varepsilon}(\Delta p - \Delta n), \quad (9)$$

where R_{in} is the rate of the interband recombination of the nonequilibrium electrons and vacancies [1, 11–14] and ε is the dielectric constant.

If the condition of quasineutrality [1, 11–15] is met,

$$\left|\frac{dE_{ph}}{dx}\right| \ll \frac{4\pi q}{\varepsilon}\Delta p, \quad (10)$$

it follows from equation (9) that

$$\Delta n = \Delta p, \quad (11)$$

and, therefore [1, 12–15],

$$R_{ib} = \frac{\Delta p}{\tau}, \quad (12)$$

where τ is the lifetime of the nonequilibrium carriers. Using relationships (6), (7), (11), and (12), we con-

clude that the spatial distribution $\Delta p(x)$ is given by the equations:

$$D\frac{d^2\Delta p}{dx^2} - \mu E_{\text{var}}\frac{d\Delta p}{dx} - \frac{\Delta p}{\tau} + g(x)U_-(x - x_1) = 0 \quad \text{for} \quad 0 \le x < W_1, \tag{13}$$

$$D\frac{d^2\Delta p}{dx^2} - \frac{\Delta p}{\tau} + g(x) = 0 \quad \text{for} \quad W_1 < x < W_1 + W_0, \tag{14}$$

$$D\frac{d^2\Delta p}{dx^2} - \mu E_{\text{var}}\frac{d\Delta p}{dx} - \frac{\Delta p}{\tau} + g(x)U_-(x_2 - x) = 0 \quad \text{for} \quad W_1 + W_0 < x \le W, \tag{15}$$

where the ambipolar diffusion coefficients D and the carrier mobility μ are determined by the formulas

$$D = \frac{n_e + p_e}{D_p p_e + D_n n_e} D_n D_p \cong D_p,$$
$$\mu = \frac{n_e - p_e}{\mu_p p_e + \mu_n n_e} \mu_n \mu_p \cong \mu_p, \tag{16}$$

and $U_-(x)$ is an asymmetric unit function [16].

It is well known that the number of defects in variband structures is much smaller than that in heterostructures. This is explained by smooth spatial variation of the mole composition in the variband structures. That is why we assume that the interfaces ($x = W_1$ and $x = W_1 + W_0$) between the homogeneous layer *3* (working area) and variband layers *1* and *2* (Figs. 1a and 2) contain neither recombination nor charged states. Then, it follows from equations (7) and (8) that

$$I_{ph}^{(n)}(W_1 - 0) = I_{ph}^{(n)}(W_1 + 0),$$
$$I_{ph}^{(n)}(W_1 + W_0 - 0) = I_{ph}^{(n)}(W_1 + W_0 + 0), \tag{17}$$

$$I_{ph}^{(p)}(W_1 - 0) = I_{ph}^{(p)}(W_1 + 0),$$
$$I_{ph}^{(p)}(W_1 + W_0 - 0) = I_{ph}^{(p)}(W_1 + W_0 + 0), \tag{18}$$

$$E_{ph}(W_1 - 0) = E_{ph}(W_1 + 0),$$
$$E_{ph}(W_1 + W_0 - 0) = E_{ph}(W_1 + W_0 + 0). \tag{19}$$

Equations (13)–(15) with the boundary conditions (17)–(19) allow one to determine the distribution $\Delta p(x)$ (Fig. 2b). It may seem [2–5] that the drift velocity of vacancies in the field E_{var} must be much higher than their diffusion velocity in order to provide strong photomodulation of the conductivity in area *3* (Fig. 1) under the condition (5). Thus, we arrive at the requirement $|dE_g/dx| \gg 50$ eV/cm. However, an analysis of the expression for $\Delta p(x)$ shows that ∇E_g can be reduced by at least two orders of magnitude (Fig. 1b) by forming a special carrier distribution profile $\Delta p(x)$ (Fig. 2b) hindering the flow of photovacancies from the working area *3* to the surfaces. The formation of such a profile is possible due to the fact that $\Delta p = 0$ for $x = W_1 - 0$ and $x = W_1 + W_0 + 0$ regardless of the value $\nabla E_g \neq 0$. Indeed, it follows from the expression (6) for $I_{ph}^{(n)}$ and the relationships (11), (17), and (19) that the values $d\Delta p/dx$ are continuous at the points $x = W_1$ and $x = W_1 + W_0$. Then, we conclude that $\Delta p(W_1 - 0) = \Delta p(W_1 + W_0 + 0) = 0$ based on the expressions (6) and the relationships (18) and (19).

In our system, the field E_{ph} is analogous to the Dember field existing in homogeneous semiconductors [11, 12, 15, 17]. However, this field exists in the variband layers even for $\mu_n = \mu_p$. This is explained by the fact that $E_{\text{var}} \neq 0$ only for the vacancies. The continuity of $I_{ph}^{(p)}$, $I_{ph}^{(n)}$, and E_{ph} for $x = W_1$ and $x = W_1 + W_0$ is the reason for the quantity Δp being zero at these points of the variband layers. This is an explanation for the fact that the maximum values of Δp in the variband layers are smaller than the value of Δp in the working area by three orders of magnitude (Fig. 2b).

Our assumption of the condition of quasineutrality (10) is met everywhere except at narrow intervals in the variband layers in the vicinity of the points $x = 0$, $x = W_1$, $x = W_1 + W_0$, and $x = W$. The same situation in the near-surface area is encountered in macroscopic consideration of a similar problem in homogeneous semiconductors [15]. The size of intervals in which the condition (10) is formally violated is of the same order of magnitude as the free path of charge carriers l_m with respect to momentum. Since this quantity is a physical zero in the macroscopic theory, the approximation of quasineutrality is valid.

We conclude that even weak variband near-surface layers can prevent the photoexcited carriers from the surface recombination if the quantity E_g increases substantially at the distances about l_m from the homogeneous layer.

Note that a more mathematically correct consideration of the problem under study without assumption of the quasineutrality condition (10) is possible with the use of the method proposed in [18–20] for the case of the impurity recombination of the nonequilibrium carriers. This will be the subject of our subsequent work.

This work was supported by the Russian Foundation for Basic Research, project no. 99-02-17415.

REFERENCES

1. A. Rogaski, M. Kimata, V. F. Kocherov, *et al.*, *Infrared Photon Detectors* (SPIE Opt. Engin. Press, Bellingham, 1995).
2. A. M. Vasil'ev and A. P. Landsman, *Semiconductor Phototransducers* (Sov. Radio, Moscow, 1971).
3. P. R. Emtage, J. Appl. Phys. **33**, 1950 (1962).
4. L. J. van Ruyvent and F. E. Williams, Am. J. Phys. **35**, 705 (1967).

5. T. Gora and F. Williams, Phys. Rev. **177**, 1179 (1969).
6. A. A. Drugova and V. A. Kholodnov, in *Abstracts of the XV International Scientific–Technical Conference on Photoelectronics, Electron and Ion–Plasma Technologies, Moscow, Russia, 1998*, p. 34.
7. A. A. Drugova and V. A. Kholodnov, in *Abstracts of the International Conference on Applied Optics, St. Petersburg, Russia 1998*, p. 87.
8. P. Migliorato and A. M. White, Solid State Electron. **26**, 65 (1983).
9. D. L. Smith, Appl. Phys. Lett. **45**, 83 (1984).
10. M. D. Blue, Phys. Rev. **134** (1A), 226 (1964).
11. R. A. Smith, *Semiconductors* (Cambridge University Press, Cambridge, 1959; Inostrannaya Literatura, Moscow, 1961).
12. V. L. Bonch-Bruevich and S. G. Kalashnikov, *Physics of Semiconductors* (Nauka, Moscow, 1990).
13. E. S. Rittner, in *Photoconductivity Conference* (New York, 1956), pp. 215–268.
14. J. S. Blakemore, *Semiconductor Statistics* (Pergamon Press, Oxford, 1962; Mir, Moscow, 1964).
15. G. E. Pikus, *Principles of the Theory of Semiconductor Devices* (Nauka, Moscow, 1965).
16. G. A. Korn and T. M. Korn, *Mathematical Handbook for Scientists and Engineers* (McGraw-Hill, New York, 1961; Nauka, Moscow, 1971).
17. S. M. Ryvkin, *Photoelectric Phenomena in Semiconductors* (Fizmatgiz, Moscow, 1963).
18. V. A. Kholodnov, Pis'ma Zh. Éksp. Teor. Fiz. **67**, 655 (1998).
19. V. A. Kholodnov, in *Abstracts of the International Conference on Applied Optics, St. Petersburg, Russia, 1998*, p. 88.
20. V. A. Kholodnov, Proc. SPIE, No. 5, 3819 (1999).

Translated by A. Chikishev

Technical Physics Letters, Vol. 26, No. 3, 2000, pp. 206–207. Translated from Pis'ma v Zhurnal Tekhnicheskoĭ Fiziki, Vol. 26, No. 5, 2000, pp. 57–61.

High-Efficiency Electron Accommodation during the Interaction of Atomic Hydrogen with the Surface of Zinc Sulfide Single Crystals

V. P. Grankin and V. Yu. Shalamov

Azov State Technical University, Mariupol, Russia

Received May 27, 1999

Abstract—Experimental data are presented that confirm an important role of the electron interactions in dissipation of the energy of hydrogen molecule formation ($H + H \longrightarrow H_2$) on a ZnS crystal surface. *© 2000 MAIK "Nauka/Interperiodica".*

During the interaction of some atoms (radicals) with solids, the energy dissipation is related for the most part to chemical conversions on the surface (~4 eV per elementary event for the process of atomic hydrogen recombination). At the first instant, this energy is concentrated in the form of oscillations of the nuclei of a newly formed H_2^v molecule interacting with both atomic and electronic subsystems of the crystal. Since any solid possesses a vast number of the vibrational degrees of freedom, it is commonly accepted that the phonon channel of energy accommodation in solids is most probable, although there are certain energy limitations on the efficiency of this mechanism [1].

Some new effects discovered in recent years, such as the radical-recombination luminescence (RRL) [2], adsorption-induced luminescence (AIL) [3], and electron chemoemission from the surface [4], are related to the electron excitation of solids in the events of exothermal transformations. These effects are indicative of the existence of an electron channel for accommodation of the energy of heterogeneous reactions. The quantum yield of luminescence per atomic recombination event is below 10^{-3} [2], and the electron emission probability is even smaller ($<10^{-6}$ [4]). Therefore, according to the pre-existing theories, the electron accommodation channel must not affect the rate of dissipation of the energy of excited vibrational bonds.

Previously [5], we reported on the high-efficiency electron heterogeneous accommodation (HEHA) of the energy of chemical reactions on the surface of vibrationally-excited solids. According to this phenomenon, the rate of a heterogeneous reaction on the surface of a wide-bandgap solid crystal exhibits a several-fold increase, and the rate of electron production in the C-band of the crystal due to the heterogeneous reaction energy increases by two orders of magnitude upon excitation of the solid by UV light in the region of intrinsic absorption. The HEHA effect is evidence that the electron energy accommodation channel for the electron-excited solids may be comparable in efficiency with the phonon channel. The experiments in [5] were performed in a system of atomic hydrogen and powdered ZnS or CdS–Ag preliminarily excited by UV light (prior to atomic probing of the surface).

The purpose of this work was to study the process of relaxation of the energy of highly excited vibrational bonds on the surface of a wide-bandgap solid via the electron channel under the conditions of controlled variation of the level of electron excitation in the crystal (over nine orders on magnitude). The experiments were performed with spectroscopic-purity gases in a high-vacuum setup with an oil-free pumping unit. The solid samples were represented by self-activated ZnS(011) single crystals.

It was established that the intensity of RRL, excited by a pulsed beam of H atoms on the sample surface illuminated by a stationary UV light beam, depends on the exciting light flux density Φ, that is, on the occupancy of electron traps n_e, and increases with this value (see the figure). The electron concentration in the traps was measured by the intensity of photoluminescence I_1 from the sample. For $\Phi = 10^{12}$ photon/(cm^2 s), the RRL intensity measured in the pulsed probing mode increased by 5 orders of magnitude as compared to the I_2 value for unexcited samples. The thermal devastation of traps led to a decrease in I_2 by several orders of magnitude, with an activation energy of $\Delta E = 0.20$ eV corresponding to the energy of major electron traps in ZnS [6]. The fact that the increase in I_2 of the ZnS crystal phosphor occurring in a metastable state is related to the trapped electrons is confirmed by the I_2 versus Φ curve for a ZnS– Tm sample. In contrast to the self-activated ZnS crystal, featuring the Classen–Shen mechanism of radiative recombination on traps, the ZnS–Tm system obeys the mechanism of intracenter luminescence excitation characterized by a weak dependence of I_2 on n_e. Indeed, ZnS–Tm studied under the same conditions as ZnS showed a very small increase in I_2

1063-7850/00/2603-0206$20.00 © 2000 MAIK "Nauka/Interperiodica"

(5 orders of magnitude below that for the self-activated ZnS).

The quantum yield of RRL (i.e., the number of RRL quanta per atomic recombination event) from a self-activated ZnS single crystal in the absence of UV excitation is ~10^{-5} [3]. An increase in the I_2 by five orders of magnitude upon conversion of the same ZnS crystal into a metastable state indicates that virtually every atomic recombination event on the surface results in the electron production in the C-band of the crystal. This implies that the probability of electron excitation of a solid possessing a system of occupied shallow electron traps increases by 5 orders of magnitude to become close to unity in the presence of vibrationally excited bonds on the surface. On the other hand, every event of atomic recombination, accompanied by the energy transfer from the excited reaction product $H_2^v L$ to a trapped electron, leads to a decrease in the energy of $H_2^v L$. This implies accommodation of the reaction energy by the electron channel. Note that the stabilization of $H_2^v L$ and the formation of the reaction product take place predominantly in the vicinity of the HEHA centers, that is, electrons in traps.

Experiments on the thermoinduced emission of the light energy stored in the crystal allowed the n_e value for the sample studied to be determined for $T = 293$ K. According to Fig. 1, the estimate $n_e \sim 5 \times 10^{10}$ cm^{-2} corresponds to $I_1 = 6 \times 10^{12}$ photons/(cm^2 s). Using this estimate for n_e and the experimental electron excitation probability, we have determined the effective electron accommodation cross section that proved to be very large: $\sigma_e \geq 10^{-12}$ cm^2. According to [7], the vibrational-electron relaxation of $H_2^v L$ cannot proceed by a long-range interaction mechanism. This large σ_e value may be related only to a high-rate diffusion of the vibrationally excited $H_2^v L$ particles over the surface during their lifetime τ($\tau \sim 10^{-10}$ s). Using the above σ_e value, we may estimate the diffusion length ($l_d \sim 2000$ Å) and the diffusion rate ($v = l_d/\tau \sim 10^5$ cm/s), the latter being of the same order of magnitude as the velocity of thermal motion of H_2 molecules in the gas phase. Thus, we obtained experimental evidence that vibrationally excited molecules formed in the course of the recombination reaction diffuse on the surface at a high velocity, with an effective relaxation via the electron channel as a result of collisions with occupied electron traps.

The above results indicate that the electron channel, rather than the phonon one, may be the main channel for accommodation of the energy of vibrational excitation or chemical interaction in some electron-excited wide-bandgap solids. At the same time, our experiments gave numerical values of the contribution of the electron channel to the process of relaxation of highly excited vibrational bonds in unexcited solids. For the unexcited ZnS single crystal studied in this work, this contribution is lower by 5 orders of magnitude as compared to the contribution from the equilibrium phonon channel. This implies that the electron channel of energy accommodation in wide-bandgap solids in the absence of excitation can be neglected in comparison with the phonon channel.

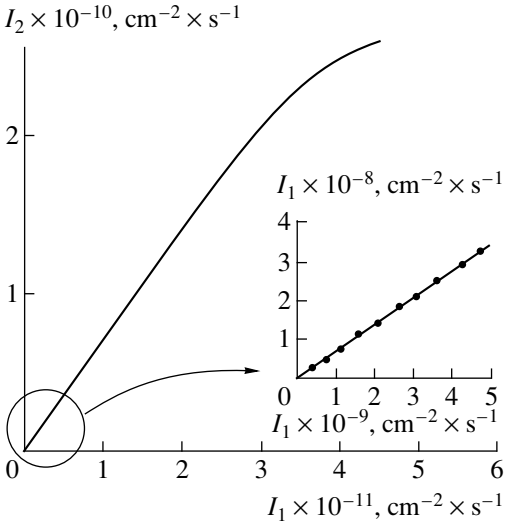

The plot of RRL intensity (I_2) from a ZnS single crystal surface probed with H atoms in a pulsed mode versus the intensity of photoluminescence from the sample (I_1) at various densities of the UV excitation; $T = 295$ K, $p_{H_2} = 3 \times 10^{-2}$ Torr; $I_2(I_1 = 0) = 5 \times 10^2$ photon/(cm^2 s).

Thus, the HEHA effect provides a new approach to description of the mechanism of photostimulated epitaxy of semiconductors, heterogeneous chemical reactions, exoelectron emission, and laser-assisted isotope separation, which is important for the chemical physics, plasma chemistry, epitaxial growth of semiconductors, etc.

REFERENCES

1. V. P. Zhdanov, *Elementary Physicochemical Processes on the Surface* [in Russian] (Nauka, Novosibirsk, 1988).
2. F. F. Vol'kenshteĭn, A. N. Gorban', and V. A. Sokolov, *Radical-Recombination Luminescence in Semiconductors* [in Russian] (Nauka, Moscow, 1976).
3. Yu. N. Rufov, A. A. Kadushin, and S. Z. Roginskiĭ, Dokl. Akad. Nauk SSSR **171**, 905 (1966).
4. V. V. Styrov, Pis'ma Zh. Éksp. Teor. Fiz. **15**, 242 (1972).
5. V. P. Grankin, Pis'ma Zh. Tekh. Fiz. **20**, 27 (1994).
6. A. M. Gurvich, *Introduction into Physical Chemistry of Crystal Phosphors* [in Russian] (Vysshaya Shkola, Moscow, 1982).
7. Yu. I. Tyurin, Poverkhnost, No. 9, 115 (1986).

Translated by P. Pozdeev

Technical Physics Letters, Vol. 26, No. 3, 2000, pp. 208–210. Translated from Pis'ma v Zhurnal Tekhnicheskoĭ Fiziki, Vol. 26, No. 5, 2000, pp. 62–66.

Electron Structure of Three-Component Lead-Silicate Glasses

A. L. Shakhmin and S. V. Murashov

State Scientific Center of Applied Chemistry, St. Petersburg, Russia

Received October 22, 1999

Abstract—The electron structure of three-component lead-silicate glasses was studied by electron spectroscopy for chemical analysis (ESCA). The contribution of the plasmon mechanism to the secondary electron emission (SEE) from lead-silicate glasses was evaluated. The SEE coefficient as function of the glass composition was determined. © *2000 MAIK "Nauka/Interperiodica".*

The study of the problems pertaining to the secondary electron emission (SEE) from glassy dielectrics involves evaluation of the contributions due to various channels of the production of secondary electrons and the conditions of their transport to the material surface. This implies the need in experimental data characterizing the electron structure of the objects under consideration. In the previous works [1–3], we have obtained some experimental data on the energy level structure of binary lead-silicate glasses and evaluated the maximum SEE coefficient for these materials with a allowance for the plasmon channel of the secondary electron production. Below, we report on the results of investigation of the effect of the third oxide component upon the electron energy structure of lead-silicate glasses. The data were obtained by the method of electron spectroscopy for chemical analysis (ESCA).

The measurements were performed on a Perkin-Elmer ESCA-5400 photoelectron spectrometer using MgKα radiation. The sample charging was corrected by calibrating spectra with respect to the electron binding energies of the C 1s (285 eV) and Au $4f_{7/2}$ (84/0 eV) levels. The samples were prepared by cleaving glasses immediately before measurements in order to minimize uncontrolled changes in the near-surface structure of the material [1]. The experiments were performed with a three-component lead-silicate glass of the composition xBaO–(0.4 – x)PbO–0.6SiO_2 (x = 0.05, 0.1, 0.15, 0.25, or 0.3).

The electron binding energies of the core levels Ba 3d, O 1s, Pb 4f and Si 2p did not vary with the glass composition, which indicated that the chemical state of elements entering into the glass composition remained unchanged. At the same time, the electron binding energies of the core levels of silicon and bridging oxygen were markedly greater as compared to those in base two-component glasses [2], which was evidence of decreasing electron density on the terminal quartz tetrahedra entering into the glass network. In order to elucidate the dynamics of the electron density variation in the valence band, we have analyzed changes in the spectrum of O 1s state of oxygen (whose 2p states form the top of the valence band in silicate glasses [4]).

According to this analysis, an increase in the content of barium oxide in the glass composition led to a considerable flattening of the low-energy wing of the O 1s peak (Fig. 1), at a rather insignificant change of the peak proper. Decomposition of the O 1s lines into components in the spectra of glasses representing the above series of compositions (using the result of decomposition of the O 1s line for a base two-component glass with 40 mol % PbO [2]) revealed three components of the bridging oxygen, one with a constant intensity (533.5 eV) and two others (corresponding to oxygen bound to the barium and lead ions) with variable intensity correlated to the concentration of the corresponding element in the glass. The electron binding energy of the component corresponding to oxygen bound to barium (531.5 eV) was greater than the energy of the component representing the oxygen–lead bond (530.5 eV). This resulted in flattening of the valence band top with increasing barium oxide content in the glass composition.

The valence-band spectra of glasses were compared, after smoothening and satellite peak subtraction, to the spectra of photoelectron energy losses measured within a 30-eV-wide energy interval after the O 1s peak. Features of the latter spectra, reflecting interaction of the photoelectrons with the electron structure of the solid sample, determine the energies of transitions between the valence and forbidden bands. The comparison of the valence-band and photoelectron energy loss spectra (Fig. 1) revealed several series of transitions from features in the valence band (related to various oxygen states) to the conduction band bottom: series *A* (due to the bridging oxygen), series B (representing oxygen bound to lead), series *C* (oxygen bound to barium), and series *E* (intraatomic transitions 6s $\longrightarrow$ 6p and 5d $\longrightarrow$ 6p in lead ions). The transition energies were determined, using the energy loss spectra, with

1063-7850/00/2603-0208$20.00

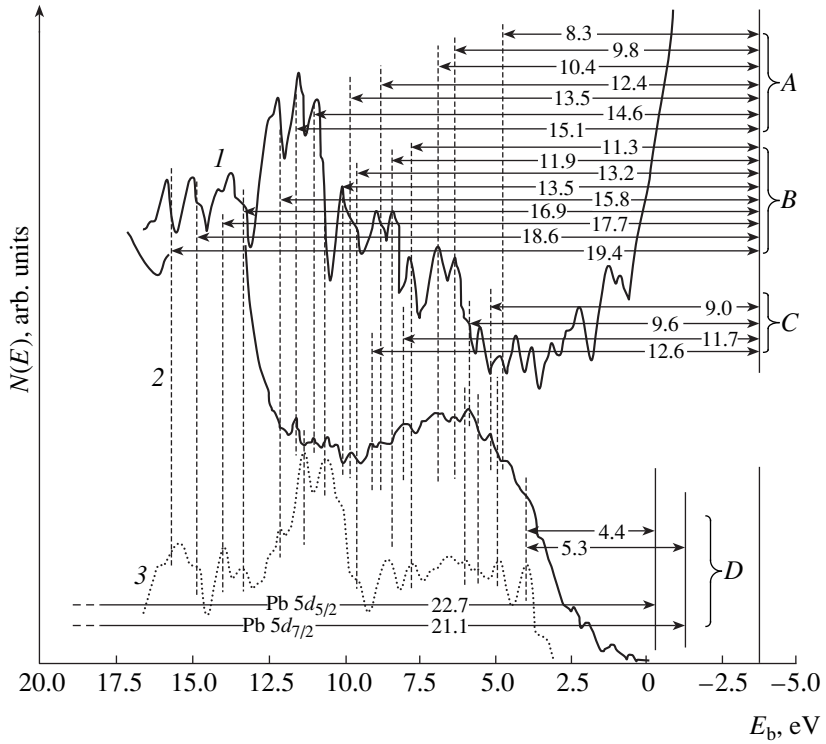

Fig. 1. Photoelectron spectra of (*1*) energy losses and (*2*, *3*) valence bands for (*2*) three-component glass with 15 mol % BaO and (*3*) base two-component glass with 40 mol % PbO.

respect to the corresponding component in decomposition of the O 1s line. The transition energies in series *A* coincide with those of the transitions at 9.0, 10.2, 11.7, 14.0, and 17.1 eV obtained from the vacuum UV reflectance spectra and the features of the photoelectron energy loss spectra corresponding to these transitions [1]. At the same time, the initial points of the transitions in series *B* coincide with features observed in the valence band of a base two-component lead-silicate glass containing 40 mol % of PbO (Fig. 1, curve *3*).

Thus, the final point of transitions determined the energy of the conduction band bottom (or the lowest unoccupied molecular orbital, LUMO). Since the valence band top in lead-silicate glasses is masked by the 6s states, we refined the bandgap value for these glasses based on analysis of the spectra of low-energy electron scattering (E_p = 10, 11, 12 eV). In these spectra the bandgap was determined as a distance from the peak of elastically reflected electrons to the beginning of a sloped front related to the electron energy losses for the excitation of interband transition. An analysis of these spectra showed that the bandgap weakly grows from 7.3 to 7.6 eV when the barium oxide content x decreases from 0.5 to 0.35. These changes are related to an increase in the energy of the conduction band bottom relative to the Fermi level.

Using the experimental data for the electron structure of glasses obtained in this work, we have estimated a relative change in the maximum possible contribution from the plasmon channel of secondary electron production to the SEE coefficient. This was done using a formula similar to that used in the case of base two-component glasses [3]:

$$\frac{\sigma(x)}{\sigma(0)} = \frac{\hbar\omega_{pl}(x)\ln(E_p/\hbar\omega_{pl}(x))}{\hbar\omega_{pl}(0)\ln(E_p/\hbar\omega_{pl}(0))},$$

where σ is the SEE coefficient, $\hbar\omega_{pl}$ is the plasmon energy, and E_p is the primary electron energy corresponding to the $\sigma(E_p)$ maximum. In our case, the $\sigma(0)$

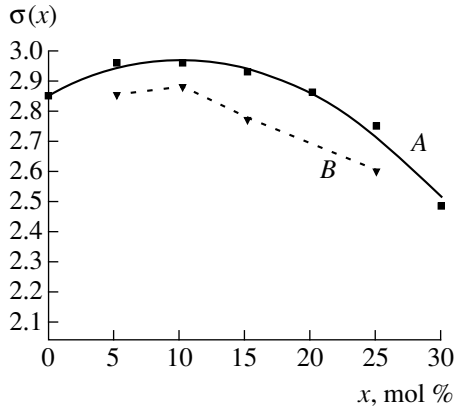

Fig. 2. Contribution of the plasmon channel of the secondary electron production versus glass composition: (*A*) calculation; (*B*) experimental data from [5].

and $\hbar\omega_{pl}(0)$ values were taken equal to those for the base two-component glass composition $0.4PbO–0.6SiO_2$. The calculated values of $\sigma(x)$ are presented in Fig. 2. The fact that the calculated values are always greater than the experimental ones is explained by neglect of the scattering of secondary electrons during their transport to the surface. As seen from Fig. 2, $\sigma(x)$ initially increases with BaO content in the region of small concentrations of this component (and, hence, small relative changes in the glass composition). However, further growth in the content of barium oxide leads to a decrease in the concentration of valence electrons and a drop in $\sigma(x)$.

Thus, we have determined parameters of the electron structure of three-component lead-silicate glasses and evaluated the contribution of the plasmon mechanism to the secondary electron emission. It is established that this contribution depends on the barium oxide content in the system from lead-silicate glasses, this factor determining to a considerable extent the dependence of the secondary emission coefficient on the glass composition.

REFERENCES

1. K. K. Sidorin and A. L. Shakhmin, Opt. Spektrosk. **72**, 160 (1992).
2. A. L. Shakhmin and A. M. Tyutikov, Fiz. Khim. Stekla **16**, 833 (1990).
3. A. M. Tyutikov and A. L. Shakhmin, Fiz. Tverd. Tela (St. Petersburg) **34**, 2893 (1992).
4. V. A. Gubanov and A. F. Zatsepin, Fiz. Khim. Stekla **13**, 811 (1987).
5. A. M. Tyutikov and V. A. Mashkov, *A Collection of Papers Devoted to the 90th Anniversary of A.A. Lebedev* [in Russian], Tr. Gos. Opt. Inst. **58**, Part 1, 43 (1985).

Translated by P. Pozdeev

Technical Physics Letters, Vol. 26, No. 3, 2000, pp. 211–214. Translated from Pis'ma v Zhurnal Tekhnicheskoĭ Fiziki, Vol. 26, No. 5, 2000, pp. 67–75.

Stochastic Resonance in a Tunnel Diode Circuit

V. M. Kartashov, A. F. Kotov, S. A. Reshetnyak, and Yu. S. Filimonov

Moscow State Institute of Radio Engineering, Electronics, and Automation, Moscow, Russia

Received July 9, 1999; in final form, October 14, 1999

Abstract—An experiment on the stochastic resonance in a bistable circuit with a tunnel diode is reported. In contrast to previous studies, the signal-to-noise ratio was measured across the load resistance. An additional narrow peak is observed in the signal-to-noise ratio plotted as function of the noise intensity. A brief explanation of the effect is given. © *2000 MAIK "Nauka/Interperiodica".*

Stochastic resonance (SR) has been attracting a great deal of attention lately [1]. This study addresses the SR in a circuit built around a tunnel diode. The existence of the phenomenon in such systems has already been confirmed [2, 3]. The SR is manifested by a distinct peak in the signal-to-noise ratio (SNR) η plotted as function of the noise intensity. This essentially stems from the signal frequency being equal to the Kramers rate, that is, to the mean rate of noise-induced transitions over the potential barrier. In contrast to [2, 3], we have found a second peak in the SNR curve. The observation was made under the following conditions: (1) the voltage across the load resistance, rather than that across the tunnel diode, was monitored; (2) the measurements were performed at a higher signal frequency, namely at $f = 100$ kHz; and (3) one of the two versions of a bistable circuit studied had the potential wells of nearly equal depths.

Figure 1 shows a schematic drawing of the experimental setup. The notation is as follows: HO is the harmonic oscillator (GZ-101), NG is the noise generator (G2-37), SA is the spectrum analyzer (S4-25) with uniform spectral density, loaded on the resistor R_0, D is the tunnel diode, R_a is the load resistance, C_0 is the capacitor connected in parallel with the tunnel diode, and E is the dc voltage source. The dc voltage serves for adjusting the operating point position in the current–voltage characteristic of the tunnel diode.

For the sake of simplicity, let us replace the HO and the NG by ideal sources of voltage and current, respectively, and neglect the effect of the SA. Furthermore, we represent the tunnel diode by an equivalent circuit comprising a resistance with memoryless nonlinearity and a linear diode capacitance C_d. Thus, the voltage u across the tunnel diode obeys the differential equation

$$\frac{du}{dt} = -W'(u) + (RC)^{-1}[A\cos(\omega t) + \xi(t)], \qquad (1)$$

with

$$W(u) = \frac{1}{C}\int\left[i_d(u) - \frac{E-u}{R}\right]du.$$

Here, A is the amplitude of the input signal, $W(u)$ is the bistable potential, $i_d(u)$ is the current–voltage characteristic of the tunnel diode, $\xi(t)$ is a zero-mean noise with rms deviation $\sigma = (\xi^2)^{1/2}$, $w = 2\pi f$ is the circular frequency of the signal, $R = R_{HO} + R_0 + R_a$ (with R_{HO} being the dc output resistance of the HO), and $C = C_d + C_0$. Specifically, $R_{HO} = 410\ \Omega$ and $C_d < 25$ pF (the latter is borrowed from [4]).

Generally, measurements are affected by the internal resistances and capacitances of the HO and the NG, as well as the SA. However, it can be shown that taking these parameters into account results in the same equation (1), except that certain effective values must be assigned to E and R.

We measured the mean voltage $\bar{u}_a$ across the load resistance, which is related to the mean voltage $\bar{u}$ across the tunnel diode as follows:

$$\bar{u}_a = E + A\cos(wt) - \bar{u}. \qquad (2)$$

Consequently, the load voltage is completely determined by the tunnel diode random voltage. If the

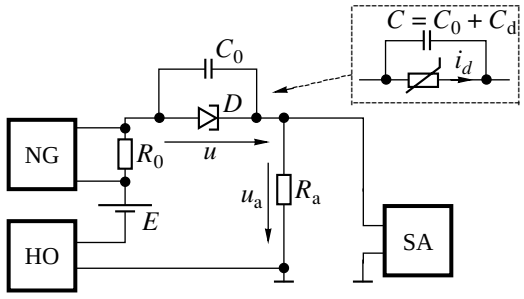

Fig. 1. Schematic drawing of the experimental setup.

1063-7850/00/2603-0211$20.00 © 2000 MAIK "Nauka/Interperiodica"

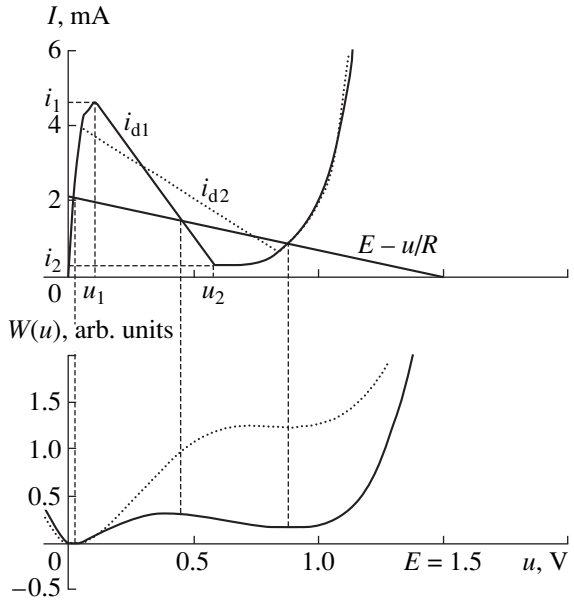

Fig. 2. Current–voltage characteristics of the tunnel diodes and the graphs of the potential functions of the circuit. Data for diodes 1 and 2 are represented by the solid and the dotted curve, respectively.

bistable potential is

$$W(u) = -\frac{a}{2}(u-u_0)^2 + \frac{b}{4}(u-u_0)^4$$

and the diode voltage is of the white noise type, then the Kramers rate is computed as

$$\mu = \frac{\sqrt{2}}{\pi} a \exp\left(-\frac{W_0}{\varepsilon}\right), \qquad (3)$$

where W_0 is the height of the potential barrier and ε is the noise intensity on the phase plane.

The measurements were carried out for two AI301V tunnel diodes with the current–voltage (i–u) characteristics displayed in Fig. 2. Also plotted are the load line $(E-u)/R$ and the potential functions $W(u)$. We selected $E = 1.5$ V and $R_0 = R_a = 150\ \Omega$. These values yield three operating points, determined as intersections of the i–u curve and the load line. Two of these points are stable and one is unstable. The stable points are situated in the left-hand and the right-hand ascending branch, respectively. The unstable point belongs to the negative-resistance (descending) portion of the i–u curve.

The Kramers rate can be estimated by the cubic approximation of the current–voltage characteristic, using coordinates of the maximum (i_1, u_1) and the minimum (i_2, u_2) points. For a symmetric function $W(u)$, we have

$$a = \frac{1}{RC}\left(\frac{3R}{2R_T} - 1\right), \quad b = \frac{2}{CR_T(u_2-u_1)^2}, \quad W_0 = \frac{a^2}{4b}, \qquad (4)$$

where $R_T = (u_2 - u_1)/(i_1 - i_2)$ is the absolute value of the mean resistance for the descending branch of the i–u curve.

It can easily be demonstrated that

$$\varepsilon = \frac{\sigma^2 \tau_0}{(RC)^2}, \qquad (5)$$

where τ_0 is the correlation time equal to the reciprocal value of the NG operating bandwidth (6.5 MHz).

Computation with (3)–(5) at $C = 300$ pF gives the Kramers rate varying within 1.4–250 kHz for $0.2 < \sigma < 0.3$ V. It is this range of σ values where the SNR $\eta(\sigma)$ can be expected to behave in an unusual manner, since the range includes a point at which the signal frequency equals the Kramers rate.

The quantity $\eta = (S/N)^2$, where S is the signal amplitude and N is the noise intensity, was measured across the load resistance by means of the SA. The values of S and N at the system output were taken directly from the screen. The measurement error was below 10%. Input signals of relatively high amplitude A were applied. With zero noise, only the first harmonic of regular shape was present in the output spectrum if $A \le A_c = 0.28$ V; otherwise, the output signal shape was distorted and four to five higher harmonics appeared.

Figures 3 and 4 present the plots of S, N, and η versus σ for several values of A. The data in Fig. 3 were obtained with diode 1 and $C_0 = 0$. Note the first narrow peak in the $\eta(\sigma)$ curves, which was not reported in [2, 3]. Since $W(u)$ is asymmetric, the measured values depend on the i–u curve branch (right vs. left) where the operating point is initially situated with zero noise. For $A = 0.14$ V, the dotted and the dashed curves correspond to the operating point belonging to the left-hand or the right-hand ascending branch, respectively. Figure 3 indicates that the position of the operating point influences only the segments where $\sigma < 0.4$ V. In particular, the first peak in $\eta(\sigma)$ is higher when the operating point is initially in the right-hand branch.

The graphs of $N(\sigma)$ exhibit a minimum similar to that observed in the experiments reported by [2]. At this noise level, the operating point leaves the left-hand branch and begins hopping between the branches. Note that we observed a minimum in $N(\sigma)$ also when the $\eta(\sigma)$ curve had a single maximum as in [2]. Consequently, there are factors other than the presence of a valley in $N(\sigma)$ that contribute to the double-humped behavior of $\eta(\sigma)$.

The circuit version with diode 2, taken from another batch, produced dramatically decreased peaks in $\eta(\sigma)$, the values of E, R, and signal amplitudes being unchanged (Fig. 4a). We suggested that the height of the first peak depends on diode capacitance, as well as on the current–voltage characteristic (Fig. 2). In order to verify the hypothesis, an additional capacitance C_0 = 284 pF was connected in parallel with diode 2. The results of subsequent measurements are presented in Fig. 4b. These data testified to the hypothesis by showing abruptly increased peaks. Furthermore, Fig. 4c indicates that the first peak rises with the signal amplitude A and shifts toward lower noise intensities.

It is also interesting to follow the evolution of the harmonic amplitudes of the load voltage at A = 0.28 V with increasing σ. When $\sigma \le 10$ mV, only the first harmonic is present. As σ increases, the higher harmonics appear. At a certain point, their growth changes to decline. The higher the order of a harmonic, the faster it decreases. The behavior of the first harmonic is most interesting. This harmonic suddenly disappears at $\sigma \approx 200$ mV to leave only the second harmonic in the spectrum, which corresponds to the minimum in Figs. 3 and 4. At $\sigma >$ 200 mV, the first harmonic arises again, with the second harmonic slowly decreasing. Then, the first harmonic amplitude exhibits a maximum (related to the first peak in Figs. 3 and 4) and begins to drop again. At $\sigma \approx 350$ mV (related to the second minimum in Figs. 3 and 4) the amplitudes of the first and the second harmonic cross the noise level. The further increase in σ leads to the growth of the first harmonic alone, the other harmonics being absent. Similar processes were observed with other A values at which two peaks exist in $\eta(\sigma)$.

The results of our experiments can be explained as follows. We believe that the narrow peak arises due to the fact that the load voltage is a superposition of the input signal and the tunnel diode output voltage [see equation (2)]. Noise in a bistable system is known to modify the amplitude and phase of the output signal [1, 5]. Therefore, $\bar{u} = kA\cos(\omega t + \varphi)$ so that

$$\bar{u}_a = E + A\sqrt{1 + k^2 - 2k\cos\varphi}\cos(\omega t - \psi), \qquad (6)$$

where k is the signal gain and φ is the signal phase. In [5], the dependences of k and φ on σ and the parameters of a bistable system were determined for $A \ll A_c$. Assume that qualitatively similar rules are valid if $A \approx A_c$. Then note that k varies smoothly as the noise intensity increases, the former approaching unity in the region where SR arises. Furthermore, the signal phase abruptly rises from 0 to $\pi/2$ in the same region, and then it abruptly drops. Consequently, the SR region is unique in that the effect of $\cos\varphi$ on $\bar{u}_a$ becomes appreciable, showing up as a narrow peak in $\eta(\sigma)$.

To sum up, the SR may occur in the random voltage across the load resistance. This type of SR is no less interesting than the SR in tunnel diode voltage. The former is remarkable for an additional peak in $\eta(\sigma)$,

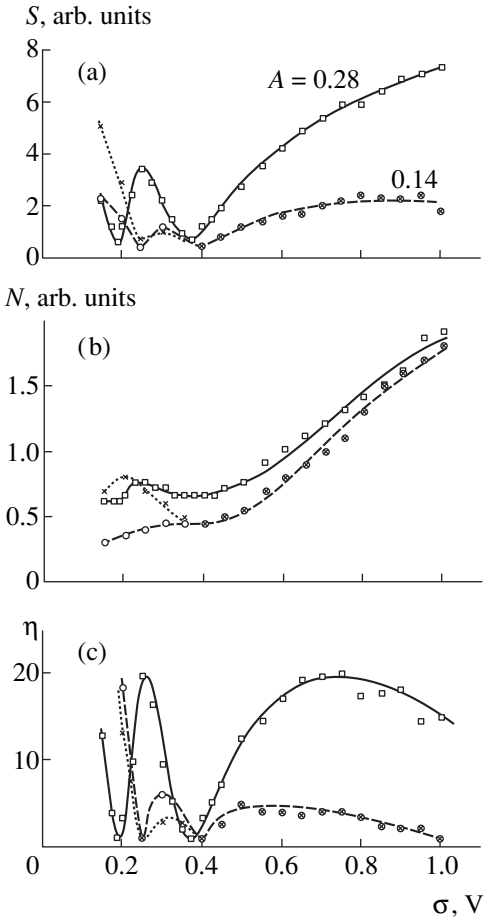

Fig. 3. (a) Signal amplitude, (b) noise intensity, and (c) SNR at the circuit output vs. the rms deviation of noise for diode 1 at C_0 = 0. The solid curves are plotted for A = 0.28 V. The dashed and the dotted curves are plotted for A = 0.14 V.

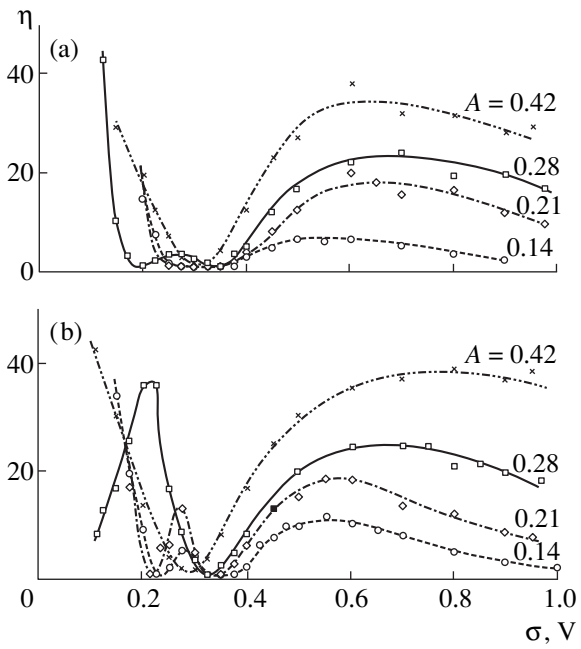

Fig. 4. The plots of SNR vs. rms deviation of noise for diode 2 at (a) C_0 = 0 or (b) C_0 = 284 pF.

which we traced to the synchronism between the input and the output signal. At certain parameter values, the peak height exceeds that for the SR in the tunnel diode voltage. Furthermore, at a sufficiently large σ [higher than that for the second minimum point of $\eta(\sigma)$], only an input-frequency harmonic and noise remain in the voltage spectrum across the load resistance. This occurs even at signal amplitudes so high that, in the absence of noise, the operating point hops from one current–voltage branch to the other and the load voltage spectrum contains many harmonics. In this respect, the experiment indicates that the circuit offers a kind of linearization at large noise intensities.

ACKNOWLEDGMENTS

We are grateful to S.V. Filatov and V.V. Krupchatnikov for kindly providing the equipment and for helpful discussions.

REFERENCES

1. L. Gammaitoni, P. Hänggi, P. Jung, *et al.*, Rev. Mod. Phys. **70**, 223 (1998).
2. R. N. Mantegna and B. Spagnolo, Phys. Rev. E **49**, R1792 (1994).
3. R. N. Mantegna and B. Spagnolo, Phys. Rev. Lett. **76**, 563 (1996).
4. A. B. Gittsevich, A. A. Zaĭtsev, V. V. Mokryakov, *et al.*, *Handbook of Semiconductor Devices: RF and Pulse Diodes and Optoelectronic Devices* [in Russian], Ed. by A. V. Golomedov (KUbK-a, Moscow, 1996).
5. S. A. Reshetnyak, J. Russ. Laser Res. **19**, 175 (1998).

Translated by A. A. Sharshakov

Technical Physics Letters, Vol. 26, No. 3, 2000, pp. 215–216. Translated from Pis'ma v Zhurnal Tekhnicheskoĭ Fiziki, Vol. 26, No. 5, 2000, pp. 76–79.

Heterogeneous Processes Affect the Hydrodynamic Resistance of a Surface Streamlined by a Nonequilibrium Gas Flow

I. P. Zavershinskiĭ and E. Ya. Kogan

Samara State Aerospace University, Samara, Russia

Received July 19, 1999; in final form, October 25, 1999

Abstract—A mechanism responsible for a decrease in the turbulent friction of bodies moving in (or streamlined by) a vibrationally-nonequilibrium gas flow is proposed. Heating of the gas in the immediate vicinity of the surface as a result of heterogeneous relaxation may decrease the transverse velocity gradient and reduce the friction resistance coefficient. © *2000 MAIK "Nauka/Interperiodica".*

An important task of the modern aerodynamics is to develop an adequate theoretical model capable of describing a significant decrease in hydrodynamic resistance for the motion of bodies with supersonic velocities in nonequilibrium gaseous media.

The total resistance to the motion of a body streamlined by the gas flows is a sum of the wave resistance and the friction resistance. A mechanism explaining the decrease in the wave resistance was proposed previously [1]. Kazakov *et al.* [2, 3] considered mechanisms of decrease in the friction resistance at the expense of artificial local heating of a streamlined surface.

Another factor of this kind can be the heating of gas in a near-wall layer as a result of heterogeneous relaxation of the internal degrees of freedom in the system of atoms or molecules of the gas or plasma. Heating of the wall and the gas stream in the immediate vicinity of the wall as a result of the heterogeneous relaxation leads to a sharp drop in the transverse velocity gradient $\partial u_x/\partial y$ and an increase in the displacement thickness of the boundary layer $\delta(x)$. Under these conditions, an increase in the dynamic viscosity coefficient μ with the temperature is a less significant factor.

In the vibrationally-nonequilibrium gas, the near-wall relaxation becomes an important process provided that the time of the heterogeneous relaxation τ_H is smaller than the characteristic time of the bulk relaxation (e.g., of the *VT*-relaxation) τ_{VT}: $\tau_H < \tau_{VT}$. In order to evaluate the corresponding conditions, we will use equation of the shake-up model of the heterogeneous relaxation [4]:

$$\frac{1}{\tau_H} = \frac{4\times 10^{-2} S}{\pi^{3/2} V}\frac{mk(kT)^3}{\rho_H(\hbar c_S)^3\hbar\omega_0}\left(\frac{kT}{2\pi m}\right)^{1/2}\left(\frac{\hbar\omega_0}{kT}\right)^{9/2}$$
$$\times\frac{\exp(-\hbar\omega_0/2kT_V)}{\mathrm{sh}(\hbar\omega_0/2kT_V)}\left(1-\exp\left((\alpha-\beta)\frac{\hbar\omega_0}{kT}\right)\right).$$

The τ_{VT} value is given by the formula $\tau_{VT} = 1/nk_{VT}$. In the above S and V are the area and volume of the streamlined body, m is the molecular mass, k is the Boltzmann constant, T is the gas temperature, ρ_H is the surface material density, c_S is the sound velocity in the surface material, $\hbar\omega_0$ is the energy of the first vibrational level, T_V is the vibrational temperature, $\alpha = 3(\pi a\omega_0/\bar{v})^{2/3}$, $\beta = 1 - T/T_V$, a is the characteristic size of the molecule–surface interaction potential, $\bar{v}$ is the thermal velocity, k_{VT} is the rate constant of the bulk relaxation process, and n is the gas concentration. Estimates show that the condition of dominating heterogeneous relaxation can be satisfied at a pressure below the atmospheric pressure level and provided a cold discharge ($T_V/T \gg 1$). For example, under the conditions studied in [5] (gas, air; surface, stainless steel; humidity, 1%; $P \sim 5\times 10^3$–10^4 Pa; $\hbar\omega_0 \approx 2300$ K; $T_V \approx 900$ K; $T \approx 300$ K; $k_{VT} \approx 10^{-22}$ cm^3/s), we obtain $\tau_H \sim 10^{-3}$ s and $\tau_{VT} \sim 3\times 10^{-3}$ s.

Let us describe the dependence of the friction resistance coefficient

$$Cx = \frac{2}{\rho_\infty u_{x\infty}^2}\mu\frac{\partial u_x}{\partial y} \quad (1)$$

on the gas temperature in a fully developed turbulent boundary layer over a flat plate under the conditions of dominating heterogeneous relaxation. Here, ρ_∞ is the gas density in the oncoming flow and u_x is the longitudinal flow velocity in the vicinity of the streamlined body.

The task can be solved using equations for a turbulent compressible boundary layer over a flat plate derived within the framework of a two-layer Cebeci–Smith model [6]:

$$\rho T = \text{const}, \quad \frac{\partial \rho u_x}{\partial x} + \frac{\partial \rho u_y}{\partial y} + \frac{\partial \rho u_x}{\delta}\frac{\partial \delta}{\partial x} = 0,$$

$$\frac{\partial}{\partial y}\left[(\mu+\mu_t)\frac{\partial u_x}{\partial y}\right] = \rho u_x\frac{\partial u_x}{\partial x} + \rho u_y\frac{\partial u_x}{\partial x},$$

1063-7850/00/2603-0215$20.00 © 2000 MAIK "Nauka/Interperiodica"

$$\frac{\partial}{\partial y}\left[\left(\frac{\mu}{\sigma}+\frac{\mu_t}{\sigma_t}\right)\frac{\partial T}{\partial y}\right]+\frac{T}{\tau_H}$$

$$=\rho u_x\frac{\partial T}{\partial x}+\rho u_y\frac{\partial T}{\partial y}-(\gamma-1)M^2(\mu+\mu_t)\left(\frac{\partial u_x}{\partial y}\right)^2,$$

where M is the Mach number, l_x and l_y are the longitudinal and transverse dimensions of the boundary layer, μ_t is the turbulent viscosity coefficient, $\sigma = 0.72$, and $\sigma_t = 0.9$. Note that a change in the boundary layer model does not principally alter the results. Upon transformations, we obtain the following relationships:

$$\left(\frac{\mu}{\sigma}+\frac{\mu_t}{\sigma_t}\right)\frac{T}{l_y^2}\sim\frac{T}{\tau_H},\quad(\mu+\mu_t)\frac{u_x}{l_y^2}\sim\rho\frac{u_x^2}{l_x}.$$

Finally, we arrive at an expression describing dependence of the turbulent friction force in the gas temperature:

$$\mu\frac{\partial u_x}{\partial y}\sim\frac{\mu(\mu+\mu_t)}{(\mu/\sigma+\mu_t/\sigma_t)^{3/2}}\times\frac{(1-\exp((\alpha-\beta)\hbar\omega_0/kT))^{3/2}}{T^{1/2}}. \quad (2)$$

According to this, the heterogeneous-relaxation gas heating in the vicinity of the streamlined body leads to decrease in the friction resistance coefficient and the transverse gradient of the longitudinal velocity. The latter gradient especially sharply decreases in the region of heating. Thus, behavior of the friction coefficient is determined by interplay between the change in viscosity as function of the wall temperature and the change in thickness of the effective (most strongly heated) part of the boundary layer in the vicinity of the wall. This conclusion is confirmed by the results of numerical modeling of a similar situation for the artificial heating of a streamlined surface [3].

Another possible mechanism of the effect of heterogeneous processes on the hydrodynamic resistance was considered in [7], where it was demonstrated that the surface relaxation may change the flux of momentum from the streamlined surface. This, in turn, leads to a relative pressure variation describe by the relationship

$$\frac{\Delta P}{P}\sim\alpha\eta^*w\frac{\hbar\omega_0}{T},$$

where η^* is the degree of excitation, w is the probability of de-excitation of the molecules as a result of the heterogeneous relaxation, and α is a coefficient ($\alpha < 1$). Estimates for the conditions established in [5] yield $w \sim 10^{-1}$, $\eta^* \sim 10^{-1}$, $\Delta P/P \sim 10^{-2}$. Note that the coefficients of pressure, resistance, and buoyancy exhibit changes of the same order of magnitude.

REFERENCES

1. I. P. Zavershinskiĭ and M. N. Kogan, Teplofiz. Vys. Temp. **37**, 134 (1999).
2. A. V. Kazakov, M. N. Kogan, and V. A. Kuparev, Teplofiz. Vys. Temp. **33**, 244 (1996).
3. A. V. Kazakov, M. N. Kogan, and A. P. Kuryachiĭ, Prikl. Mekh. Tekh. Fiz. **37**, 70 (1996).
4. E. Ya. Kogan and V. N. Mal'nev, Ukr. Fiz. Zh., 374 (1983).
5. V. L. Bychkov, L. P. Grachev, I. I. Esakov, *et al.*, Preprint Inst. Probl. Mekh. Ross. Akad. Nauk, No. 27 (1997).
6. T. Cebeci and A. M. Smith, *Analysis of Turbulent Boundary Layers* (Academic Press, New York, 1974).
7. V. N. Mal'nev and A. V. Nedospasov, in *Abstracts of Papers Presented at the International Meeting "Prospects of MHD and Plasma Technologies in Aerospace Research," Moscow, March 24–25, 1999* (Moscow, 1999), pp. 47–48.

Translated by P. Pozdeev

Technical Physics Letters, Vol. 26, No. 3, 2000, pp. 217–219. Translated from Pis'ma v Zhurnal Tekhnicheskoĭ Fiziki, Vol. 26, No. 5, 2000, pp. 80–85.

Experimental Study of the Parametric Interaction between Space-Charge Waves in Thin-Film GaAs-Based Semiconductor Structures

A. I. Mikhaĭlov

Saratov State University, Saratov, 410071 Russia

Received July 6, 1999

Abstract—An experiment on the effect of low-frequency pumping on the output spectrum of a thin-film *n*-GaAs semiconductor structure with electron drift is reported in the 3-cm and 8-mm wavelength intervals. It is found that the presence of a low-frequency pump signal, whose power greatly exceeds that of a test signal, considerably enhances microwave transfer within two frequency bands separated by $\Delta f = f_s - f_p$, where f_s is the frequency of a weak test signal and f_p is the frequency of the pump signal ($f_p < f_s$). The transfer enhancement is evidence of the existence of effective parametric coupling between space-charge waves in the drift electron stream. This effect confirms the conclusions of previous theoretic studies. © *2000 MAIK "Nauka/Interperiodica".*

The parametric interaction between space-charge waves (SCWs) in thin-film semiconductor structures with negative differential conductivity was theoretically studied in a number of works [1–3]. The semiconductor was assumed to be *n*-GaAs or *n*-InP. It has been shown that (i) damped SCWs may become growing waves if pumping is applied at a lower frequency and (ii) SCW parametric interaction under the stated conditions can be useful for frequency conversion and controlled signal filtering at wavelengths of a few centimeters or in the millimeter-wave region. By contrast, experimental data on the subject are very nearly lacking except for [4, 5], which report preliminary results.

This paper presents experimental data on the effect of low-frequency pumping on the output spectrum of an *n*-GaAs thin-film structure. The measurements were performed in the 3-cm and 8-mm band.

Figure 1 shows the layout (top view) of a thin-film structure with a planar design implementing the structure. An *n*-GaAs epitaxial film *1* of thickness 1–5 μm is grown on an *i*-GaAs semi-insulating substrate *2*. The electron density in the film is chosen to be $n_0 = (2–6) \times 10^{14}$ cm^{-3}. The choice aims for stationary distributions of the field and the electron concentration (so as to prevent formation of the Gunn domains). Created on the film surface are the cathode and anode ohmic contacts (OCs) together with the input and output coupling elements (CEs). Identically designed as a Schottky-barrier strip contacts, the CEs connect the sample structure to microwave sources and meters. During the measurements, the Schottky barriers were driven with dc voltages and a large dc bias voltage U_A (above the threshold) was applied between the cathode and anode OCs, causing electron drift in the film. The CEs perform the conversion between electromagnetic waves and SCWs. The distance L_a between the OCs (i.e., the length of the active region), was chosen to be 60–120 μm, depending on the version of the structure. The choice was dictated by the requirement that L_a must be greater than several SCW wavelengths. The aperture of the structure, $2b$, was 290–500 μm. This insured operation in the Fresnel region [6] with a large margin, since $L_a\lambda/b^2 < 1$. The spacing l_1 between OCs and the adjacent CEs, and the CE width l_2, were selected within 1.5–8 μm, depending on the version of the structure.

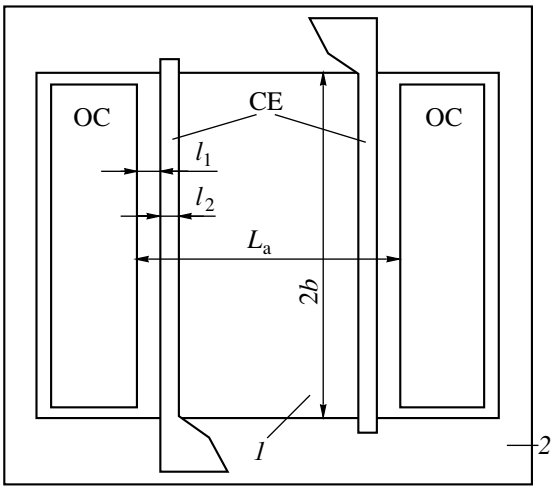

Fig. 1. Layout of the sample structure (top view). CE is a coupling element and OC is an ohmic contact.

1063-7850/00/2603-0217$20.00 © 2000 MAIK "Nauka/Interperiodica"

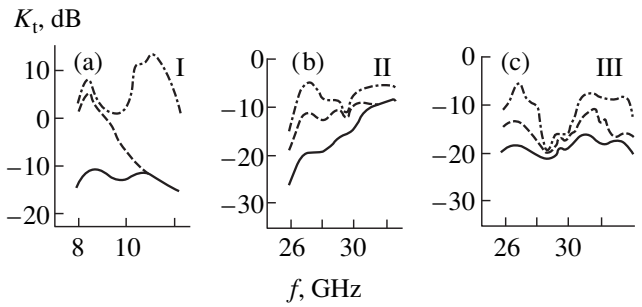

Fig 2. Measured transfer coefficient vs. frequency for (a) P_p = 10.8 mW, f_p = 2.3 GHz, and U_A = 34 V; (b) P_p = 18 mW, f_p = 4 GHz, and U_A = 16.5 V; and (c) P_p = 6 mW, f_p = 8 GHz, and U_A = 11 V.

The entire structure (except for the contact regions) was covered with a thin SiO_2 film (with a thickness of ~0.3 μm). The thickness of the CE metallic films was 0.3–0.5 μm, and that of the contact regions of the CEs and OCs was 1–1.5 μm.

Thin-film semiconductor structures from seven batches were employed. The physical parameters for three batches that showed best performance are given in the table.

The experiment was conducted at wavelengths near 3 cm, 2 cm, or 8 mm. The voltage standing-wave ratio and attenuation were measured with panoramic devices of the R2-61 and R2-65 types. This paper presents most typical results, obtained in the 3-cm and 8-mm band. Pumping was provided by the oscillators G4-79 (1.77–2.58 GHz) and G4-80 (2.56–4 GHz) and also by the sweep oscillator (8–12 GHz) from R2-61. Microwave signals were coupled in and out by means of coplanar waveguide sections.

The measurements were organized as follows: (1) With zero dc voltages and a zero pump signal, a test signal was turned on at a frequency lying in the sweep range of R2-61 and R2-65 and the output spectrum in the frequency range of interest was displayed on the screen. This measurement provided the value of the transmission coefficient K_t as function of the frequency f (1st measurement). (2) Drive voltages were applied to the Schottky barriers of the CEs, a voltage U_A from the descending portion of the current–voltage characteristic was applied between the OCs, and the spectrum of the response to the test signal was displayed on the screen (2nd measurement). (3) In addition to the test signal and the dc voltages used in the previous measurement, a pump signal was turned on and the response spectrum was displayed on the screen (3rd measurement). The transmission coefficient K_t as a function of frequency was thus measured three times.

Table

Series	I	II	III
$2a$, μm	4	2.2	1.4
n_0, 10^{14} cm^{-3}	3	3.5	6
$2b$, μm	300	320	290
L_a, μm	60	100	60
l_1, μm	8	5	2.5
l_2, μm	8	5	1.5

Figure 2 depicts the measured distributions of K_t over frequencies. Measurements 1, 2, and 3 are represented by the solid, dashed, and dot–and–dash curve, respectively. Each panel corresponds to a particular series of samples, the number of which (in accordance with the table) is indicated in the figure. Test-signal power was within 0.1–1 μW in each measurement, and the drive voltages across the input and the output Schottky barriers were –2 and –0.5 V, respectively. The values of the power P_p and the frequency f_p of the pump signal and those of U_A are given in the caption to Fig. 2.

The results suggest that pumping amplifies the output signal in two distinctive frequency bands, for which $f_s - f_i = f_p$, where f_s is the frequency of the upper band, f_i is that of the lower band, and f_p is the pump frequency. This relation was observed in all of the measurements, irrespective of the frequency and power of pumping. Note that the effect is more pronounced in the 3-cm wavelengths range, where a gain shows up in both bands. On the other hand, K_t was below zero in both f_s and f_i bands for any dc voltages when pumping was turned off. As for wavelengths near 8 mm, no gain was obtained in this range. This obviously stems from the fact that the 8-mm band includes the boundary frequency of amplified SCWs in *n*-GaAs [7, 8].

To sum up, the experiment has demonstrated that lower-frequency pumping ($f_p < f_h$) insures efficient parametric coupling between the SCWs of frequencies f_s and f_i. This finding confirms the conclusions of theoretical studies [1–3].

ACKNOWLEDGMENTS

I am grateful to Prof. A.A. Barybin and his coworkers A.A. Levitskiĭ and M.S. Kravtsov for kindly providing the samples of series I and II and for their help in experiments. I am also grateful to S.A. Sergeev for his assistance in some of the measurements.

REFERENCES

1. Yu. M. Ignat'ev and A. I. Mikhaĭlov, Izv. Vyssh. Uchebn. Zaved., Radioélektronika **33**, 76 (1990).
2. A. I. Mikhaĭlov and S. A. Sergeev, Izv. Vyssh. Uchebn. Zaved., Radioélektronika **38**, 43 (1995).
3. A. I. Mikhaĭlov and S. A. Sergeev, Pis'ma Zh. Tekh. Fiz. **22**, 75 (1996).
4. V. A. Ivanchenko, Yu. M. Ignat'ev, and A. I. Mikhaĭlov, in *Interaction of Electromagnetic Waves with Semiconductors and Semiconductor–Dielectric Structures* [in Russian] (Saratov Gos. Univ., Saratov, 1988), Part 2, pp. 117–118.
5. V. A. Ivanchenko and A. I. Mikhaĭlov, in *Abstracts of Papers of All-Union Conference on Transducers, Moscow–Nizhniĭ Novgorod, Russia, 1991*, p. 12.
6. Yu. N. Balodis and S. I. Lutovinov, *Functional Electronics*, Part 1: *Acoustoelectronic Devices* [in Russian] (LIÉS, Leningrad, 1988).
7. A. I. Mikhaĭlov, Pis'ma Zh. Tekh. Fiz. **21**, 89 (1995).
8. A. I. Mikhaĭlov and S. A. Sergeev, Pis'ma Zh. Tekh. Fiz. **25**, 85 (1999).

Translated by A. A. Sharshakov

Technical Physics Letters, Vol. 26, No. 3, 2000, pp. 220–222. Translated from Pis'ma v Zhurnal Tekhnicheskoĭ Fiziki, Vol. 26, No. 5, 2000, pp. 86–94.

Numerical Simulation of Some Peculiarities of the Formation of Multilayer Structures with Quantum Dots by Means of Molecular Beam Epitaxy

V. A. Egorov and G. É. Tsyrlin

Institute of Analytical Instrument Building, Russian Academy of Sciences, St. Petersburg, Russia

Received October 11, 1999

Abstract—Some peculiarities of the growth of nanoislands in multilayer heteroepitaxial stressed systems are studied numerically based on the theory of elastic interaction. Different scenarios of the behavior of the system of vertically coupled islands and the intervals, separating these scenarios, are determined for the case of heteroepitaxial growth of multilayer systems. *© 2000 MAIK "Nauka/Interperiodica".*

The study of processes involved in the formation of nanostructures during heteroepitaxial growth in the systems with lattice mismatch is one of the main directions in the modern fundamental and applied physics of the surface of solids [1, 2]. This is related to the fact that the quantum dots, formed as a result of the decay of a stressed pseudomorphous layer at the interface of such semiconductor structures, can be used for manufacturing optoelectronic devices of the new generation [3, 4] and make it possible to model the properties of "artificial atoms" [5]. The progress in the theory of formation of such nanostructures [6] and the discovery of the effects of ordering in quantum-dimensional formations on the surface of the (InAs, InGaAs)/GaAs heterosystem during the molecular beam epitaxy process [7, 8] make it possible to obtain quantum-dimensional structures with predetermined geometry. Tersoff *et al.* [9] proposed a model of the process of self-organization in a system of quantum dots, based on the construction of multilayer structures, and presented experimental data confirming the "effective" self-organization of $Si_{0.25}Ge_{0.75}$ on Si surface. The authors reported also on a limiting value of the stable distance between nanoislands ($3.5L$) in the layer starting from certain time, where L is the characteristic distance between layers in the system (spacer thickness). However, alternative experimental data [10, 11] that provide evidence for the existence of, at least, an interval of stable distances for the system InGaAs/GaAs are in contradiction with the data presented in [9]. A possibility of the vertical correlation and anticorrelation in a vertically coupled system of flat nanoislands (the height of which is much smaller than the lateral size) in multilayer heteroepitaxial structures was considered in [12].

This work is devoted to the study of nanoislands formed during heteroepitaxial growth and their cooperative behavior during the growth of multilayer structures with multitudes of quantum dots by numerical methods based on the Maradudin theory [13], and to the possibility of using such structures in real systems.

Figure 1 shows the geometry of a system consisting of two islands of the same shape and dimensions (which implies equal contributions to the elastic energy of the surface) for two cases: (i) a decrease of the distance between islands leads to their merging with the formation of a single island in the next layer ("merging and vanishing") and (ii) an increase of the distance between islands leads to the formation of another island between them ("separation and birth"). We search for the critical values of distances between the islands: when the distance is larger or smaller than the critical one, the pattern of mutual arrangement of the islands in

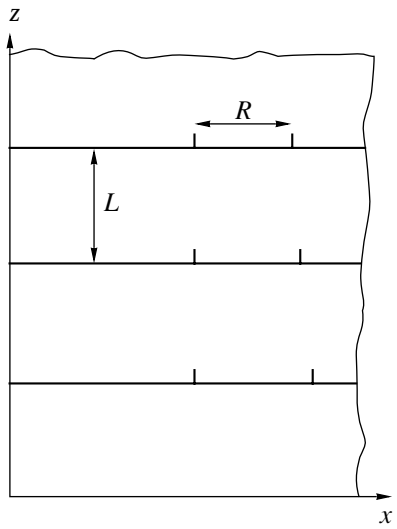

Fig. 1. Schematic diagram of the arrangement of islands in a heteroepitaxial multilayer system: L is the spacer thickness, R is the distance between the neighboring islands in one layer.

1063-7850/00/2603-0220$20.00 © 2000 MAIK "Nauka/Interperiodica"

the next layer changes quantitatively which means that the total number of the islands increases or decreases.

The calculations were performed within the framework of the Maradudin theory. It is assumed that an island has zero lateral size but a finite height. Different volumes of the islands result in their different contributions to the elastic energy. The elastic interaction of a single defect (nanoisland) with the whole surface is calculated as

$$U(x) = C(x^2 + L^2)^{-3/2} P_2(x^2/(x^2 - L^2)^{1/2}),$$

where C is the coefficient proportional to the volume of a nanoislands and depending on the elastic constants of the materials, L is the spacer thickness, and P_2 is the Legendre polynomial. Then the next defect is added and so on. The total change of the elastic energy of the surface is a sum of contributions from all defects. After that, the nanoislands are deposited onto the surface in the areas of minima of the elastic energy and "healing" of the layer take place. The process is repeated until the system reaches a stable configuration of the islands. Within the framework of the proposed theory, the spacer thickness appears to be the main parameter that influences the positions of the islands inside the layer. The simulation was performed for a 2D case.

We use the following parameters of the system for numerical calculations: the distance between layers L = 50 Å (this is a typical size used, in particular, in the experimental works [10, 11]); the lateral size of the system is about 1000 Å. In the initial layer, one island (left) has a fixed position (x_1 = 200) and the position of the right island is varied. The islands are of the same size, which provides clear illustration of the system behavior; interaction of the islands with the sample boundaries is neglected.

Figure 2a shows a situation when the right island is located at x_2 = 455 (the distance between the islands is 5.1L). The minima of the elastic energy in the second layer appear virtually exactly (within the accuracy of calculations that is about 0.05 Å) above the islands in the initial layer, which results in the emergence of a vertically correlated system of nanoislands. The correlation is quite high: if the positions of islands in each layer are shifted (to within a given accuracy) to one and the same side (the worst variant), then the deviation accumulated for 1000 layers is 5 Å, which means that the structure is shifted by an interatomic distance (such a number of layers is obviously of no practical interest). However, the shift of the second island in the system to the right results in a quantitative change: for the distances starting from 5.2L, an additional minimum appears in the elastic energy of the surface (Fig. 2b). Within the framework of our method of calculations, this minimum is considered as a center of nucleation for the next layer, and the third island appears between the initial two (Fig. 3). Thus, it is seen that the system is stable (in the sense of formation of new centers of nucleation) if the distance between the islands is smaller than 5.1L. The act of birth of a new island in the next layer takes place if the distance is larger than 5.2L.

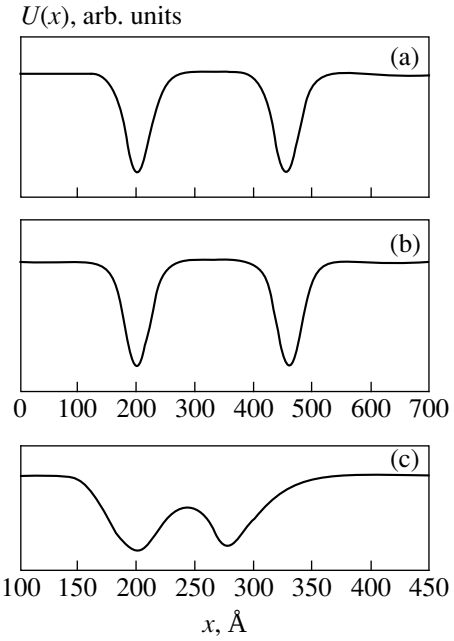

Fig. 2. Profiles of elastic energy in the second layer of a heteroepitaxial multilayer system of two islands. The position of the left island is x_1 = 200 Å, the positions of the right island are x_2 = 455 (a); 460 (b); and 280 Å (c).

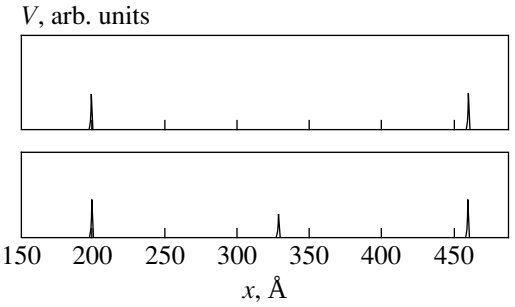

Fig. 3. The initial distribution of islands in the first layer (top) and the appearance of the third island in the second layer (bottom). The volumes of the islands are given in relative units.

Consider now another critical distance, whereby quantitative changes in the system take place if the distance between the islands is smaller than this value. Figure 2c shows the arrangement for x_2 = 280 (1.6L), after which the minima of the elastic energy start moving slightly: x_1 = 200.8 and x_2 = 279.2 for the left and the right islands, respectively. Nucleation in these positions in the second and subsequent layers results in even closer mutual approaching of the minima. After a certain number of layers, the system reaches the state shown in Fig. 4.

Therefore, the distance between the nanoislands R determines several possible scenarios of the system evolution:

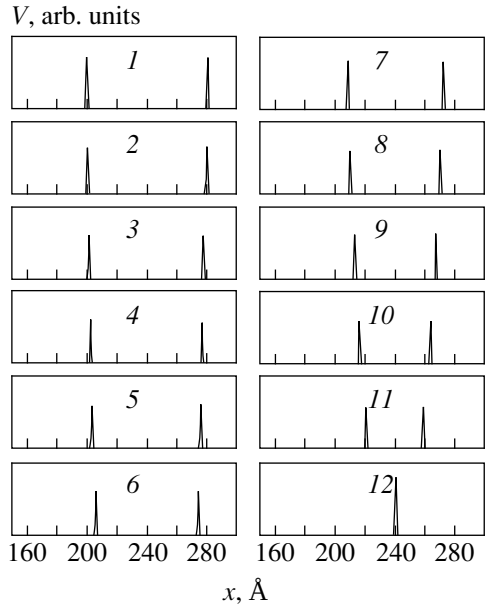

Fig. 4. Evolution of a system of two islands. Numbers enumerate the layers of the structure. The volumes of the islands are given in relative units.

1) if $R \le 1.6L$, the islands approach each other and merge;

2) if $R \ge 5.2L$, an additional island appears;

3) in the intermediate interval, there are stable states without merging or formation of the islands.

A combination of these scenarios can be observed in a real system with many islands.

An analysis of the equations used for calculations yields a narrower range of the values of R ($2.8L$–$4L$) for which the system is stable. However, in practice a substantial shift of the islands resulting in their mutual approaching and merging can be detected only if the number of layers is unreasonably large (>1000) for a real experiment. It happens so because of the exponential growth of the rate of mutual approaching of the islands and their hardly detectable shifts (fractions of Angström) in the initial stages for R close to $2.8L$.

It is seen from the calculations that distances equal to the critical values (i.e., those determining the three scenarios) or close to them appear to be "stable" in the sense of shifts in the positions of the points in the subsequent layers. Therefore, the statement on the existence of a certain distance ($3.5L$) between the islands, to which the system tends with increasing number of layers must be questioned.

Thus, we have studied numerically some peculiarities of the growth of nanoislands in multilayer heteroepitaxial systems. We determined possible scenarios of the evolution of a system of vertically coupled islands in the case of heteroepitaxial growth of multilayer systems and the intervals that separate these scenarios. These results are in qualitative agreement with the experimental data [10, 11] on the formation of a regular system of nanoislands in the 5th–10th layer, with the distance between the islands ranging from $3L$ to $5L$. In the future, we plan to study the influence of the shape of the nanoislands on their relative arrangement in the neighboring layers of the heteroepitaxial structure.

This work was supported by the Russian Foundation for Basic Research (project no. 98-18317), and the Program "Physics of Solid State Structures" (project no. 98-2029). G. É. Tsyrlin is grateful for partial financial support of this work by the INTAS, Foundation project no. YS 54.

REFERENCES

1. L. Goldstein, F. Glas, J. Y. Marzin, *et al.*, Appl. Phys. Lett. **47**, 1099 (1985).
2. Y.-W. Mo, B. S. Swartzentruber, R. Kariotis, *et al.*, Phys. Rev. Lett. **63**, 2393 (1989).
3. N. Kirstaedter, N. N. Ledentsov, M. Grundmann, *et al.*, Electron. Lett. **30**, 1416 (1994).
4. N. N. Ledentsov, M. Grundmann, N. Kirstaedter, *et al.*, Solid State Electron. **40**, 785 (1996).
5. N. N. Ledentsov, V. M. Ustinov, V. A. Shchukin, *et al.*, Fiz. Tekh. Poluprovodn. **32**, 358 (1998).
6. V. A. Shchukin, N. N. Ledentsov, P. S. Kop'ev, and D. Bimberg, Phys. Rev. Lett. **75**, 2968 (1995).
7. G. É. Cirlin, G. M. Guryanov, A. O. Golubok, *et al.*, Appl. Phys. Lett. **67**, 97 (1995).
8. M. Grundmann, J. Christen, N. N. Ledentsov, *et al.*, Phys. Rev. Lett. **74**, 4043 (1995).
9. J. Tersoff, C. Teichert, and M. G. Lagally, Phys. Rev. Lett. **76**, 1675 (1996).
10. G. É. Tsyrlin, V. N. Petrov, S. A. Masalov, *et al.*, Fiz. Tekh. Poluprovodn. **33**, 733 (1999).
11. G. É. Tsyrlin, V. N. Petrov, S. A. Masalov, *et al.*, Pis'ma Zh. Tekh. Fiz. **23**, 80 (1997).
12. A. A. Schukin, D. Bimberg, V. G. Malyshkin, *et al.*, Phys. Rev. B **57**, 12262 (1998).
13. A. A. Maradudin and R. F. Wallis, Surf. Sci. **91**, 423 (1980).

Translated by A. Chikishev

Technical Physics Letters, Vol. 26, No. 3, 2000, pp. 223–224. Translated from Pis'ma v Zhurnal Tekhnicheskoĭ Fiziki, Vol. 26, No. 6, 2000, pp. 1–4.

Effect of Annealing in Various Atmospheres on the Photoluminescence of Porous Silicon

E. B. Korol' and S. M. Kikkarin

Physico-Technical Institute, Ministry of Science and Education of the Republic of Kazakhstan, Almaty, Kazakhstan

Received August 30, 1999

Abstract—The effect of isochronous annealing in various atmospheres on the photoluminescence of porous *p*-type silicon samples obtained by anodization under identical conditions was studied. Comparative experimental data for the samples annealed in air, nitrogen, and vacuum are presented. © *2000 MAIK "Nauka/Interperiodica".*

The luminescent properties of porous silicon have been discovered quite recently [1] and now this material is rather extensively studied in view of the prospect for creating new silicon-based optoelectronic devices. Although the nature of the photoluminescence in porous silicon is still incompletely clear, most of the researchers believe the phenomenon to be related to the quantum effects in nanosize elements of the porous structure [2–4], which makes the problem important from the standpoint of fundamental science as well.

By now, a considerable experimental material has bee gained concerning the effect of various factors upon the luminescent properties of porous silicon [5–7]. However, the large number of variable factors frequently hinders elucidation of the clear trends because of the simultaneous variation of several parameters or the difference in important parameters in the course of various experiments.

Below we report on the results of experiments devoted to elucidation of the character of degradation of the peak of photoluminescence observed in the samples of porous silicon upon isochronous annealing under identical conditions in various atmospheres.

The samples of porous silicon were obtained by anodization of the single-crystalline *p*-Si wafers with a resistivity of 6–8 Ω cm. The treatment was effected in a cell filled with an H_2O–C_2H_5OH–HF electrolyte solution (1 : 2 : 1) and continued for 30 min at a current density of 30 mA/cm^2. After anodization, the wafers cov-

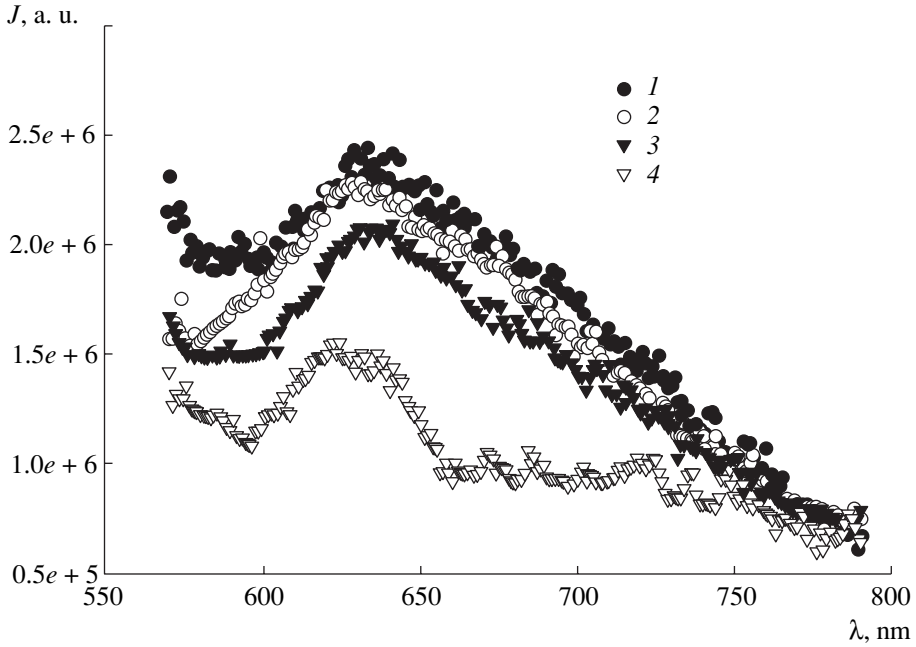

Laser-excited photoluminescence spectra of porous *p*-Si samples annealed in various atmospheres: (*1*) control (unannealed sample); (*2*) vacuum; (*3*) nitrogen; (*4*) air.

1063-7850/00/2603-0223$20.00

ered with a layer of porous silicon were cut into samples and annealed, with one part retained as the control sample. The photoluminescence spectra were measured in an automated mode using a modified computer-controlled SDL-2 setup. The luminescence was excited by radiation of an argon laser with the wavelength components 458, 488, and 514 nm. The samples were annealed in a resistance-heated quartz tube kept in air, purged with nitrogen, or placed in a vacuum system (10^{-4} atm). All samples were annealed using the same thermal regime: the sample was placed at room temperature into the quartz tube, the tube was either filled with a gas (air or nitrogen) or evacuated, and then the sample was treated at 200°C for 40 min.

The results of photoluminescence measurements for four different samples are presented in the figure. As is seen, the porous silicon exhibits luminescence with a peak at about 640 nm. A sharp increase in the intensity of emission at short wavelength is explained by approaching the wavelength of the laser excitation (514 nm). The annealing treatment in all cases markedly reduced the luminescence peak height, the maximum degradation being observed upon the annealing in air. The annealing in vacuum or nitrogen leads only to a small decrease in the emission intensity (by approximately 10 and 20%, respectively).

The strong decrease in the photoluminescence intensity in the samples annealed in air is naturally attributed to increasing thickness of the surface SiO_2 layer and, accordingly, decreasing size of silicon crystallites. The decrease in emission can be partly also due to the silicon oxidation by residual oxygen, although the effect is most probably related to changes in composition of the layer covering the surface of pores.

REFERENCES

1. L. T. Canham, Appl. Phys. Lett. **57**, 1046 (1990).
2. V. Lehmann and U. Göselle, Appl. Phys. Lett. **58**, 856 (1991).
3. J. Kanemitsu, H. Uto, and J. Masumoto, Phys. Rev. B **48**, 2827 (1993).
4. F. Koch, V. Petrova-Koch, T. Muschik, *et al.*, Mater. Res. Symp. **283**, 197 (1993).
5. E. V. Astrova, V. V. Ratnikov, R. F. Vitman, *et al.*, Fiz. Tekh. Poluprovodn. (St. Petersburg) **31**, 1261 (1997).
6. E. D. Shelonin, M. V. Naĭdenkova, A. M. Khort, *et al.*, Fiz. Tekh. Poluprovodn. (St. Petersburg) **32**, 494 (1998).
7. T. Ya. Gorbach, S. V. Svechnikov, P. S. Mertenko, *et al.*, Fiz. Tekh. Poluprovodn. (St. Petersburg) **31**, 1414 (1997).

Translated by P. Pozdeev

Technical Physics Letters, Vol. 26, No. 3, 2000, pp. 225–227. Translated from Pis'ma v Zhurnal Tekhnicheskoĭ Fiziki, Vol. 26, No. 6, 2000, pp. 5–11.

Separately Bounded InGaAsP High-Power Laser Heterostructures Obtained by VPE of Organometallic Compounds

E. G. Golikova, V. A. Gorbylev, N. Yu. Davidyuk, V. A. Kureshov, A. Yu. Leshko, A. V. Lyutetskiĭ, N. A. Pikhtin, Yu. A. Ryaboshtan, V. A. Simakov, I. S. Tarasov, and N. V. Fetisova

Ioffe Physicotechnical Institute, Russian Academy of Sciences, St. Petersburg, Russia

Received November 10, 1999

Abstract—InGaAsP/InP laser heterostructures with two stressed quantum wells operating in the wavelength range 1.3–1.55 μm were obtained by VPE of organometallic compounds. An optical emission power of 2.4 W was reached for the laser diodes with 100-μm wide strips operated in the continuous lasing mode at 20°C. A minimum threshold current density was 260 A/cm^2. A differential quantum efficiency $\eta_d = 40\%$ was obtained with a 1.9-mm-long Fabry–Perot resonator. The internal optical losses of the heterostructures are reduced to 2.6–4.2 cm^{-1}. © *2000 MAIK "Nauka/Interperiodica".*

In recent years, considerable achievements have been gained in the development of high-power semiconductor laser diodes with low internal optical losses emitting in the wavelength range 0.8–1.0 μm [1–3]. A similar approach has been used to increase the power of laser diodes emitting in the long-wavelength region (λ = 1.55 μm) [4]. We have spent much effort to develop a technology of separately bound (SB) InGaAsP heterostructures with low internal optical losses based on the method of liquid-phase epitaxy (LPE), which failed to realize all advantages of the proposed approach [5].

The purpose of this work was to obtain and characterize SB InGaAsP laser heterostructures with low internal optical losses for high-power laser diodes emitting in the 1.3–1.55 μm wavelength range using the method of vapor-phase epitaxy (VPE) of organometallic compounds (metalorganic-hydride VPE).

Using the metalorganic-hydride VPE technique [6], we have fabricated SB InGaAsP laser heterostructures with two stressed quantum wells on InP substrates. Figure 1 schematically shows the energy band diagram of these heterostructures. The sample structures had different solid solution compositions in the active region and the waveguide layers. The solid solution compositions of stressed quantum wells corresponded to E_g = 0.95 eV (λ = 1.3 μm) and E_g = 0.8 eV (λ = 1.55 μm). The quantum wells had a thickness of 50 Å and were separated by an intermediate waveguide layer with a thickness of 150 Å. The main waveguide layer with a thickness of D = 1 μm had a bandgap width of E_{gw} = 1.1 and 1.25 eV for the emission wavelengths 1.55 and 1.3 μm, respectively. Neither the active region nor the waveguide layers were intentionally doped. A 1-μm-thick wide-bandgap P-emitter was doped to a concentration of 7×10^{17} cm^{-3}. A contact p-type layer with a thickness of 0.3 μm had a hole concentration of 2×10^{18} cm^{-3}. The resulting laser heterostructures were used to form, by appropriate photolithographic operations, strips with a width of W = 100 μm on a SiO_2 insulating substrate. These sample structures were provided with ohmic contacts of the Au/Te and Au/Zn type. Then the structures were divided into laser diodes with a resonator length of L = 500–4000 μm. The resonator edges were coated with Si/SiO_2 mirrors with a reflection coefficient of $R > 0.95$ and clarifying layers with $R < 0.04$. Finally, the laser diode samples were mounted by soldering onto copper heat-exchangers using an indium-based solder.

Figure 2 shows the plots of inverse differential quantum efficiency $1/\eta_d$ versus the Fabry–Perot resonator length L. Using linear approximations of these plots, we may determine the intrinsic quantum yields of the laser diodes studied. In our case, the intrinsic quantum yield was $\eta_i = 67 \pm 3\%$ for the lasers operating at

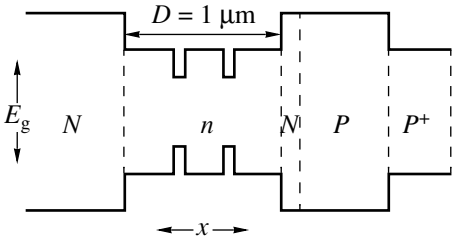

Fig. 1. Schematic energy band diagram of the laser heterostructures studied.

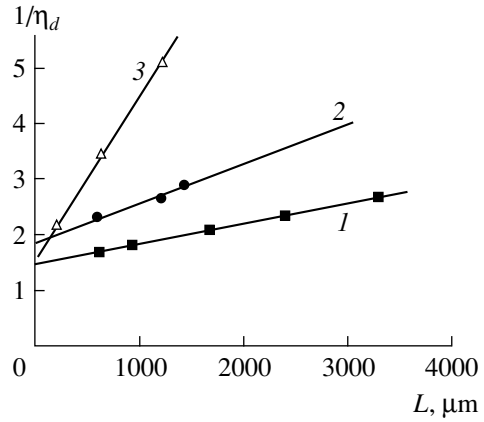

Fig. 2. The plots of inverse differential quantum efficiency $1/\eta_d$ versus the laser diode length L in laser heterostructures with two stressed quantum wells for the wavelengths λ = 1.3 (*1*) and 1.55 μm (*2*); the plot *3* refers to a structure with a single unstressed quantum well for λ = 1.3 μm; η_i = 67 (*1*), 53 (*2*), 66% (*3*); α_i = 2.6 (*1*), 4.2 (*2*), 23 cm^{-1} (*3*).

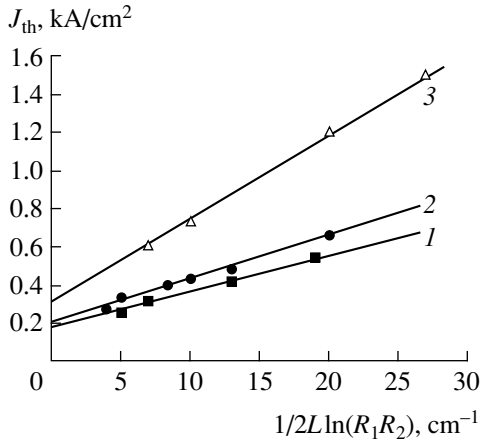

Fig. 3. The plots of threshold current density J_{th} versus output losses for (*1*, *2*) laser heterostructures with two stressed quantum wells operating at the wavelegths λ = 1.3 and 1.55 μm, respectively, and (*3*) a structure with a single unstressed quantum well for λ = 1.3 μm.

λ = 1.3 μm and η_i = 53 ± 3% for the samples operating at λ = 1.55 μm. In both structures, the quantum yield is lower compared to the best reported value (η_i = 78% [4]). Using the experimental data, we may also determine the internal optical losses in the sample structures. These values were α_i = 2.6 cm^{-1} for the lasers operating at λ = 1.3 μm and α_i = 4.2 cm^{-1} for the heterostructures operating at λ = 1.55 μm. These values are also somewhat inferior to the best known (1.3 cm^{-1} [4]). This implies that the laser structure design has to be optimized so as to increase the quantum yield and reduce the optical losses in the *p*-type emitter.

Figure 3 shows a plot of the threshold current density J_{th} versus output losses. The minimum threshold current density (260 A/cm^2) was obtained in a laser diode operating at a wavelength of 1.3 μm. It should be also noted that, despite higher values of α_i and η_i, the laser diodes operating at 1.55 μm had a threshold current density of 280 A/cm^2, which is comparable with the world best values [7].

For a comparison, Figures 2 and 3 show data for the SB laser heterostructures with a single unstressed 300-Å-thick quantum well fabricated by the LPE method. As is seen, parameters of the laser heterostructures fabricated by the metalorganic-hydride VPE technique in this work are markedly better as compared to those of their LPE counterparts. The threshold current densities are reduced to less than half. However, a most significant result from the standpoint of increase in the optical output power is a decrease in the level of internal optical losses (amounting to 23 cm^{-1} in a usual unstressed single-well SB laser heterostructure).

As is known, the high output power can be achieved only in lasers with sufficiently long resonators, provided that high differential quantum efficiency is retained as well. The high η_d values can be retained in laser diodes with long resonators only provided that internal optical losses are sufficiently small. Therefore, it is the decrease in internal optical losses in SB InGaAsP laser heterostructures with two stressed quantum wells (to 2.6 and 4.2 cm^{-1}) that allowed the optical output power to be markedly increased.

Figure 4 shows the output power versus pumping current curves for the laser diodes with λ = 1.3 and 1.55 μm operated in the continuous lasing mode at a heat-exchanger temperature of T = 20°C. The resonator lengths for λ = 1.3 and 1.55 μm were 1.9 and 1.2 mm and the differential quantum efficiency was retained on

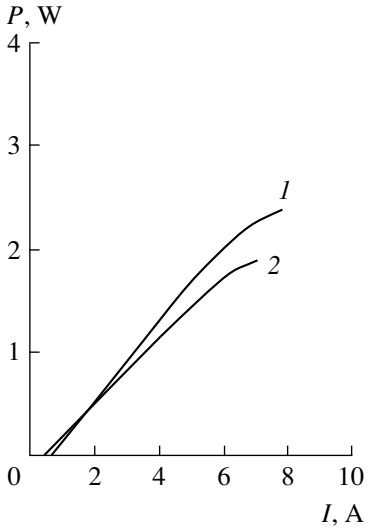

Fig. 4. The plots of output power P versus pumping current I for the laser diodes with a stripe width W = 100 μm operating at λ = 1.3 (*1*) and 1.55 μm (*2*) in the continuous lasing regime at a heat-exchanger temperature of T = 20°C.

a level of 40 and 33%, respectively. The further increase in the resonator length was inexpedient because increasing internal losses resulted eventually in a drop of η_d. The observed bending of the W versus I curve (related to heating of the active region) was observed at a pumping current of 6–8 A and was explained, in our opinion, by a high serial resistance of our structures $R_s = 0.45\ \Omega$.

Thus, we have obtained and studied laser diodes with an output optical power of 2.4 and 1.9 W emitted in the continuous regime for the wavelengths 1.3 and 1.55 μm, respectively. The laser heterostructures were fabricated by the metalorganic-hydride VPE technique using InGaAsP solid solutions on *n*-type InP substrates. The new structures exhibit low level of internal optical losses (2.6–4.2 cm^{-1}).

The work was supported by the State Interinstitution Scientific-Technological Program "Physics of Solid-State Nanostructures," projects nos. 97-1035, 99-2037, and 99-2038.

REFERENCES

1. J. K. Wade, L. J. Mawst, D. Botez, *et al.*, Appl. Phys. Lett. **72**, 4 (1998).
2. J. Wang, B. Smith, X. Xie, *et al.*, Appl. Phys. Lett. **74**, 1525 (1999).
3. A. Al-Muhanna, L. J. Mawst, D. Botez, *et al.*, Appl. Phys. Lett. **73**, 1182 (1998).
4. D. Garbuzov, L. Xu, S. R. Forrest, *et al.*, Electron. Lett. **32**, 1717 (1996).
5. D. Z. Garbuzov, N. Yu. Antonishkis, A. D. Bondarev, *et al.*, IEEE J. Quant. Electron. **27**, 1531 (1991).
6. E. G. Golikova, V. P. Duraev, S. A. Kozikov, *et al.*, Kvant. Élektron. **22**, 85 (1995).
7. W. T. Tsang, F. S. Choa, M. C. Wu, *et al.*, Appl. Phys. Lett. **58**, 2610 (1991).

Translated by P. Pozdeev

Technical Physics Letters, Vol. 26, No. 3, 2000, pp. 228–230. Translated from Pis'ma v Zhurnal Tekhnicheskoĭ Fiziki, Vol. 26, No. 6, 2000, pp. 12–17.

Electric Analog of Magnetic Resonance

B. A. Andrianov

South Ural State University, Chelyabinsk, Russia

Received July 26, 1999

Abstract—Resonant rf absorption was observed during an experiment with a negative point-to-plane corona discharge at a small-amplitude rf voltage combined with a high dc voltage. The absorption is maximum if the frequency of the rf voltage is equal to or a multiple of the repetition rate of Trichel pulses. A number of resonances are detected by recording the Q factor of a resonant circuit, which includes the interelectrode gap, against the dc voltage at a fixed frequency of the rf voltage. The rf voltage frequency was plotted against the electrostatic field strength, both measured under the resonance conditions at different interelectrode spacings. For the most part of the interelectrode gap, the initial portions of these graphs are linear with the proportionality factor being independent of the interelectrode spacing. The proportionality factor is evaluated as 1.0 ± 0.2 Hz m/V. © *2000 MAIK "Nauka/Interperiodica".*

The most remarkable feature of a negative corona discharge is the ability to self-ordering. This is manifested by a linear dependence of the repetition rate of Trichel pulses [1] on the average discharge current in a wide frequency range. Furthermore, the initial portion of the corona current–voltage characteristic is also linear, which was established in early experiments [2] in contrast to the theory [3]. It is therefore easy to infer that the Trichel pulse rate is a linear function of the electric field strength. Thus, an analogy with magnetic resonance comes to mind.

In this context, it seems very interesting to look for the possible selective absorption of a weak harmonic electric field applied to a negative corona. In our experiment, we tried several values of electric field frequency, ranging from tens of kilohertz to a few megahertz. The measurements were performed according to the well-known Q meter technique [4]. The Q meter was constructed using commercial electronic components. However, the setup was modified as follows. The energy-absorbing component was the capacitive branch of a parallel resonant circuit. The branch comprised the interelectrode gap, a blocking capacitor, and the measuring capacitor of the Q meter. The gap was connected in series with the blocking capacitor, and the two-element chain was connected in parallel with the measuring capacitor. The blocking capacitance was used to set the amplitude of the rf electric field applied to the discharge gap. The Trichel pulse rate f_{Tr} was controlled by varying a dc voltage U across the interelectrode gap. The voltage U (diminished by a divider) and the dc output voltage of the Q meter (proportional to the Q factor) are fed to the corresponding inputs of a two-coordinate recorder. Resonant energy absorption must show up as a decrease in amplitude of the rf voltage across the resonant circuit, resulting from a drop in the circuit impedance. Thus, the presence of dissipation is indicated by a reduced Q factor.

The experiment was carried out in air at room temperature. The Q meter was tuned to a selected frequency f and then a high dc voltage U across the gap was turned on, after which the Trichel pulses appeared immediately with a repetition frequency f_{Tr} determined by the U value. When f_{Tr} and its multiples are far from f, the output voltage of the Q meter is almost independent of U.

Nevertheless, resonant drops in Q have been observed at certain dc voltages in the Q–U characteristic, as shown in Fig. 1. These features cannot be related to peaks in the interelectrode gap conductance, since the average discharge current varies monotonically. The measured values of f_{Tr} indicate that the resonant

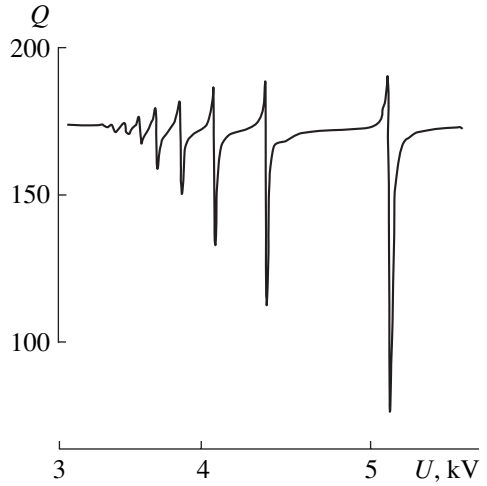

Fig. 1. The Q factor of the resonant circuit vs. the dc voltage between electrodes at f = 1 MHz and h = 5 mm.

1063-7850/00/2603-0228$20.00 © 2000 MAIK "Nauka/Interperiodica"

peaks are situated at the U values for which the frequency of the rf voltage is equal to or a multiple of f_{Tr}:

$$f_{\mathrm{r}} = N f_{\mathrm{Tr}} \quad (N = 1, 2, 3, \ldots), \tag{1}$$

where the resonant dc interelectrode voltages will be denoted as U_{r}, the subscript "r" denoting the resonance conditions.

In Fig. 1, the rightmost resonant curve corresponds to $f_{\mathrm{r}} = f_{\mathrm{Tr}}$ for $N = 1$, the neighbor refers to $N = 2$, and so on. No resonances were observed at $f_{\mathrm{Tr}} > f$.

Note that the existence of a series of resonances does not violate the analogy with magnetic resonance: for example, recall rf parametric resonances in the optically pumped vapor of an odd alkali metal isotope [6, 7]. The consideration also gives an insight into some peculiarities of the Trichel pulses [2], such as the spontaneous pulse rate hopping between different modes, the existence of double-mode regimes, and especially the fact that the current–voltage characteristic curves of different modes have nearly the same slopes (see Figs. 4 and 5 in [2]).

A lower voltage sweep rate makes it clear that the shape of a resonant line is the same is that for the well-known absorption curves observed for magnetic resonance. Although our Q peaks are slightly distorted by a dispersion signal, the latter effect varies from measurement to measurement, seemingly depending on the accuracy to which the Q meter is tuned and on spontaneous phase shifts in the measuring system.

Another feature in common with the magnetic resonance is rf broadening: we have found that the resonant peak width doubles upon a two-fold increase in the rf voltage amplitude.

The design of the Q meter did not allow us to vary f continuously. Nevertheless, the Q factor was measured at different values of f at the same dc voltage. The Q–f diagram thus obtained looked exactly like an absorption curve, the width being around 10 kHz.

We have also conducted a thorough theoretical and experimental investigation into unwanted effects of various instrumental factors (variation in the operating frequency of the resonant circuit, mutual synchronization between the Trichel pulses and the oscillator of the Q meter, interaction between the resonant circuit and harmonics of the Trichel pulses). All these factors were found to be of minor importance. Thus, the phenomenon is inherent to a negative point-to-plane corona discharge.

The f_{r}–U_{r} pairs measured for a fixed interelectrode spacing h and $N = 1$ indicated that the initial portion of the $f_{\mathrm{r}}(U_{\mathrm{r}})$ plot is linear, while its slope depends on h. However, we have found that the latter dependence is virtually eliminated if one changes over from U_{r} to E_{r}, the latter denoting the electric field strength on the plane facing the point electrode.

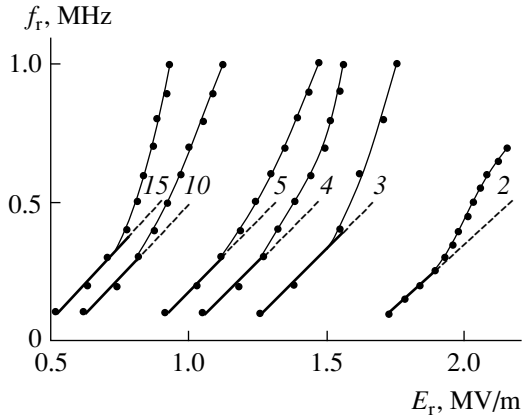

Fig. 2. The resonant frequency of the rf voltage vs. the resonant electrostatic field strength on the plane electrode in front of the tip. The corresponding value of the gap width h (in millimeters) is written indicated at each curve.

The value of E_{r} can be computed by means of formula (2.53) from [5]. In the context of this study, we obtain

$$E_{\mathrm{r}} = (3/2)U_{\mathrm{r}}/h. \tag{2}$$

Although (2) is approximate and does not allow for the finite curvature radius of the needle point, it adequately describes the field within certain region, rather than only on the plane in front of the point. According to the measurements reported in [5], the electric field strength in the interelectrode gap differs from its value on the plane by less than 10–15% for distances up to $0.7h$ from the plane. Thus, in the greater portion of the interelectrode space, the electric field strength is roughly the same as that on the plane.

The f_{r}–E_{r} curves shown in Fig. 2 confirm that the slope of the initial portion is in fact independent of the interelectrode spacing. This portion obeys the equation

$$f_{\mathrm{r}} = \gamma_E(E_{\mathrm{r}} - E_0), \tag{3}$$

where E_0 is a certain value of field strength and γ_E is a common proportionality factor. The parameter E_0 is proportional to a corona-start voltage and can be computed from (2).

According to the data presented in Fig. 2,

$$\gamma_E = (1.0 \pm 0.2)\ \text{Hz m/V}, \tag{4}$$

where the error includes both systematic and random components.

To sum up, the resonant rf absorption in an electrostatic field suggests that the phenomenon is an electric analog of the magnetic resonance. The idea encourages one to regard γ_E as a "gyroelectric" ratio. Of course, the

analogy leaves many questions open and so deserves further thorough investigation.

REFERENCES

1. G. W. Trichel, Phys. Rev. **54**, 1078 (1938).
2. W. N. English, Phys. Rev. **74**, 170 (1948).
3. L. B. Loeb, *Electrical Coronas: Their Basic Physical Mechanisms* (California University Press, Berkeley–Los Angeles, 1965).
4. A. Abragam, *The Principles of Nuclear Magnetism* (Clarendon, Oxford, 1961; Inostrannaya Literatura, Moscow, 1963).
5. I. P. Vereshchagin, *Corona Discharge in Processing Equipment Using Electron or Ion Beams* [in Russian] (Énergoatomizdat, Moscow, 1985).
6. C. Cohen-Tannoudji, J. Dupont-Roc, S. Haroche, *et al.*, Rev. Phys. Appl. **5**, 95 (1970).
7. B. A. Andrianov, P. S. Ovcharenko, and N. V. Studentsov, USSR Inventor's Certificate No. 847237 (published 15 July 1981), Byull. Izobret., No. 26.

Translated by A. A. Sharshakov

Technical Physics Letters, Vol. 26, No. 3, 2000, pp. 231–232. Translated from Pis'ma v Zhurnal Tekhnicheskoĭ Fiziki, Vol. 26, No. 6, 2000, pp. 18–21.

A Statistical Criterion for the Onset of Turbulence

S. A. Novopashin* and Amador Muriel**

** Institute of Thermal Physics, Siberian Division, Russian Academy of Sciences, Novosibirsk, Russia*

*** Center of Theoretical and Computational Sciences, SBMA, Olongapo, Philippines*

Received November 11, 1999

Abstract—The Reynolds number is interpreted as the ratio of phase volumes for the macroscopic and microscopic motions of molecules. Effect of the second virial coefficient on the critical Reynolds number was predicted and experimentally verified. The measurements were performed in a Hagen–Poiseuille flow of several gases (He, Ne, Ar, Kr, Xe, N_2, CO_2, and SF_6). © *2000 MAIK "Nauka/Interperiodica".*

Analysis of the Navier–Stokes equations for the flow of incompressible fluids reveals a single dimensionless parameter characteristic of the flow type—the Reynolds number $R = \rho LU/\eta$ (for gases, $\eta \propto \rho\lambda v$). Here, ρ is the fluid density, L and U are the characteristic length and velocity of the flow, and η is the dynamic viscosity (λ is the mean free path of molecules in the gas and v is a characteristic thermal velocity of molecules in the gas). Violation of the steady laminar flow conditions and the transition to a turbulent flow are conventionally associated with the loss of stability accompanying increase in the Reynolds number.

The steady laminar flow is a layered flow in which molecules (representing the ideal gas) move according to the current lines (streamlines) topology, while the mixing is provided by the diffusion processes. At every time instant, the uncertainty of coordinates for each molecule in the phase space is determined by the mean free path of molecules and their possible momentum values (according to the velocity distribution function). Thus, the one-dimensional phase volume of a molecule can be evaluated as $\gamma = m\lambda v/\hbar$, where m is the molecular mass and $\hbar$ is the Planck constant.

In a turbulent flow, the current lines exhibit chaotic mixing over a characteristic scale L determining the uncertainty of coordinates for each molecule in this regime. The turbulent mixing, in contrast to the diffusional mixing in a laminar flow, involves a large number of molecules (mole). Here, the uncertainty of momentum is determined by the number of molecules in the mole and by the uncertainty of a macroscopic flow velocity which, according to the pattern of the streamline mixing, is of the order of the flow velocity U. For this macroscopic motion, the phase volume per molecule can be evaluated as $\Gamma = mLU/\hbar$. Comparing this quantity with the phase volume determined by molecular collisions, we arrive at the ratio

$$\Gamma/\gamma = UL/\lambda v \propto R, \qquad (1)$$

which coincides, to within a constant numerical factor, with the Reynolds number. Note that the Reynolds number is usually considered as characterizing the ratio of inertial and viscous forces. In our approach, the Reynolds number is interpreted as the ratio of phase volumes for the macroscopic and microscopic motions of molecules. The transition from laminar to turbulent flow takes place when this ratio exceeds certain critical level.

For the ideal gas, the statistical interpretation does not lead to new consequences. However, application of this approach to a nonideal gas may give rise to distinctions, because molecular collisions contribute to the statistical sum [1]. The correction is determined by the so-called second virial coefficient $B(T)$ defined as

$$B(T) = \frac{1}{2}\int(1 - e^{-U_{1,2}/T})dV,$$

where T is the absolute temperature and $U_{1,2}$ is the intermolecular interaction potential. Note that B can be both positive and negative, depending on the temperature and the particular interaction potential.

In the case of weak nonideality, a linear correction to the phase volume for the microscopic motion can be written as

$$\gamma_{\text{real}} = \gamma(1 + \alpha n B(T)), \qquad (2)$$

where n is the concentration of molecules and α is a dimensionless coefficient. The phase volume related to the macroscopic motion remains unchanged Taking into account equations (1) and (2), the Reynolds number for a weakly nonideal (real) gas is

$$R_{\text{real}} = \frac{\Gamma}{\gamma_{\text{real}}} = \frac{R}{(1 + \alpha n B)}.$$

Assuming that a statistical criterion for the transition from laminar to turbulent flow is universal (R_{real} = const), we obtain a relationship between the conven-

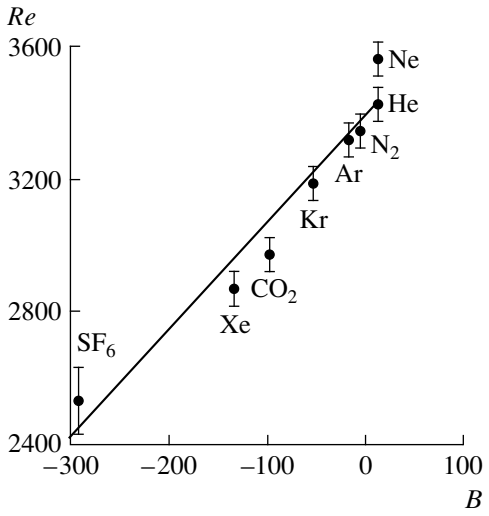

The plot of critical Reynolds number versus second virial coefficient.

tional Reynolds number R and the second virial coefficient B:

$$R = R_{\text{real}}(1 + \alpha n B). \quad (3)$$

We have performed experimental verification of this relationship for the Hagen–Poiseuille flow in a long circular pipe. This flow is stable with respect to infinitely small perturbations [2, 3]. The onset of turbulence in this system is caused by finite perturbations or by insufficiently smooth boundary conditions at the pipe inlet. In the laminar flow regime, the resistance coefficient is $\lambda = (\Delta P/L)/(\rho U^2/2d) = 64/Re$ [4], where $\Delta P/L$ is the mean pressure gradient along the pipe, ρ is the gas density, U is the gas flow rate, and d is the pipe diameter. Upon transition to the turbulent mode, the resistance coefficient exhibits a sharp increase that provides reliable monitoring of the critical Reynolds number variation.

Not describing the experiment in much detail in this short communication, we only outline the major features of the experimental setup: the measurements were carried out using a 300-mm-long glass capillary with a diameter of 1.3 mm, by which a gas (contained at elevated pressure in a hermetic chamber with a volume of 0.13 m^3) elapsed into atmosphere. The experiments were performed with He, Ne, Ar, Kr, Xe, N_2, CO_2, and SF_6.

The experimental plot of critical Reynolds number versus second virial coefficient B (in cm^3/mol) is presented in the figure together with a linear approximation of this relationship ($R_{\text{real}} = 3440$, $\alpha \cong 25$, $n = 10^{-3}/22.4$ mol/cm^3). The observed correlation between the critical Reynolds number and the second virial coefficient indicates that the proposed statistical criterion provides a correct prediction of the onset of turbulence in the gas flow.

REFERENCES

1. L. D. Landau and E. M. Livshits, *Statistical Physics* (Nauka, Moscow, 1976), Part 1.
2. J. A. Fox, M. Lessen, and W. V. Bhat, Phys. Fluids **11** (1968).
3. H. Salwen, F. W. Cotton, and C. E. Grosch, J. Fluid Mech. **92**, 273 (1980).
4. L. Prandtl and O. Tietjens, *Hydro- und Aeromechanik* (Springer, Berlin, 1931).

Translated by P. Pozdeev

Technical Physics Letters, Vol. 26, No. 3, 2000, pp. 233–235. Translated from Pis'ma v Zhurnal Tekhnicheskoĭ Fiziki, Vol. 26, No. 6, 2000, pp. 22–26.

Self-Oscillatory Effects Accompanying the Field-Induced Desorption of Alkali Metals

D. P. Bernatskiĭ and V. G. Pavlov

Ioffe Physicotechnical Institute, Russian Academy of Sciences, St. Petersburg, Russia

Received October 30, 1999

Abstract—Self-oscillatory effects were observed during continuous field-induced desorption of alkali metals (K, Cs) from a gold-coated tungsten surface. The substrate surface images in alkali metal ions, reflecting various stages of the desorption process, were obtained using a field-ion microscope. © *2000 MAIK "Nauka/Interperiodica".*

We have studied the field desorption of alkali metals (K, Cs) from the surface of a tungsten needle coated with a gold film of variable thickness (from a fraction of monolayer to a few monolayers). The experiments were performed in an ultra-high vacuum field-emission microscope [1] capable of operating in the field-induced desorption microscopy (FIDM), field-electron microscopy (FEM), or desorbed-ion mass spectrometry (DIMS) modes. The deposition of gold and alkali metals onto the tungsten needle was monitored by FEM images.

Steady-state field desorption of alkali metals from tungsten was studied previously [1–3] and FIDM images of the substrate surface obtained in the continuous ion desorption regime were reported. In this regime, the adatoms are supplied to a desorption zone at the needle tip by surface diffusion of the adsorbate from the side surface areas of the needle. In this work, the field-induced desorption of alkali metal (K, Cs) from gold-coated tungsten needle surface was observed and it was established that the process is accompanied by the self-oscillatory effects, as manifested by periodic variations of the FIDM images under steady-state experimental conditions.

The self-oscillatory phenomena were observed in a certain range of electric field strengths F and temperatures T, in the course of electric-field-induced desorption of alkali atoms from the tungsten needle tip. For potassium, the self-oscillatory effects were observed during the continuous field-induced desorption at F = (1.4–3.2) × 10^7 V/cm and T = 500–800 K, and for cesium, at F = (1–2) × 10^7 V/cm and T = 300–550 K. The period of oscillations varied from fractions of a second to a few tens of seconds. Variations of the microscopic image appeared as periodic changes in the brightness of separate parts of the pattern or as the disappearance, appearance, and motion of the desorption-active zones.

Figures 1 and 2 present the FIDM images obtained in a continuous desorption regime, reflecting various stages of the self-oscillatory processes. Figure 1a shows the FEM image of a clean tungsten needle tip with indicated crystallographic faces. Figures 1b and 1c illustrate two extreme stages of a self-oscillatory process accompanying the desorption of cesium from a tungsten needle tip with a submonolayer gold film. The process was is follows. First, the FIDM image shows two bright spots in the upper part corresponding to faces of the (110) type, which implies that Cs^+ ions are only emitted from these faces (Fig. 1b). The third (110) face appears in the image bottom with an 0.5 s delay (Fig. 1c) and then disappears again. This process is repeated with a period of 5–15 s.

As the desorption regime (F, T) is modified, the character of the self-oscillatory process exhibits a change. A decrease in the temperature T led to the appearance of bright arms ($\langle 111 \rangle$ zone lines) connecting the above faces into a triangle (Fig. 1d). The arms were also involved in the oscillatory process, whereby the image brightness distribution varied in a complicated manner. When the temperature was increased, desorption of cesium ions from the third (110) face completely ceased. An increase in the field strength F increased the duration of desorption from the third (110) face. Upon the additional deposition of cesium onto the needle tip, the pattern of desorption exhibited inversion: the desorption of cesium was continuous on the bottom (110) face and periodic on the two upper faces.

Figure 2 gives another example of the periodic process, observed for the field-induced desorption of potassium. Here, a bright area (potassium desorption zone) propagates from periphery (Fig. 2a) toward the center (Fig. 2b) of the image and then rapidly turns back (to the same state as in Fig. 2a). This process is repeated with a period of 1–2 s.

The self-oscillatory processes observed did not restrict to the types descried above. Both periodic changes of various types and stationary patterns (typical of the continuous field-induced desorption of alkali

1063-7850/00/2603-0233$20.00

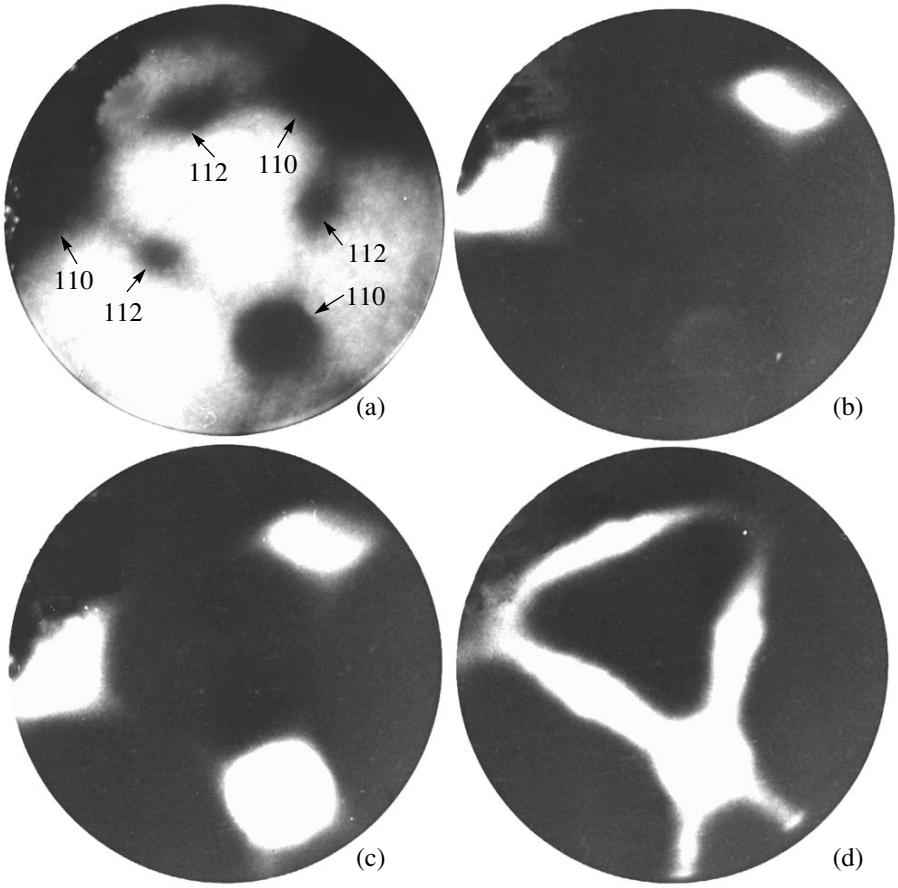

Fig. 1. Microscopic images of a tungsten needle tip: (a) FEM image of the tip annealed at $T = 2500$ K; (b–d) FIDM images in Cs^+ ions for the same gold-coated tip observed at $F = 1.3 \times 10^7$ V/cm and $T = 540$ K (b, c) and 460 K (d).

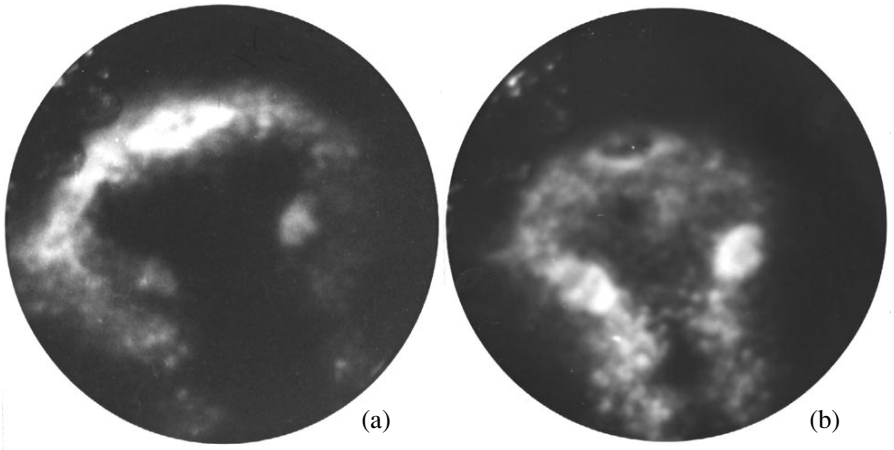

Fig. 2. FIDM images in K^+ ions for a periodic process accompanying the desorption of potassium from a gold-coated tungsten tip at $F = 2.1 \times 10^7$ V/cm and $T = 630$ K.

metals from pure metal surfaces [1, 2]) were observed in the our FIDM images, depending on the desorption conditions (*F*, *T*, and the amount of Au, K, and Cs deposited). In the absence of gold, only stationary FIDM images were obtained from the tungsten needle tip. The self-oscillatory process appeared only when gold was present, at least at an insignificant amount (a fraction of monolayer).

The self-oscillatory processes observed in the system studied are apparently caused by a complicated dependence of the desorbing field on the surface concentration of adsorbed alkali metal atoms. The role of gold in the appearance of these oscillations (related to periodic changes in the concentration of adatoms) is yet insufficiently clear. However, we may put forward some ideas to explain the phenomenon.

The effect of self-oscillations may be related to some special features of the gold–alkali metal adsorbate system. This system is characterized by a chemical reaction of gold with alkali metal, leading to the formation of a semiconducting compound [4], and by the diffusion of alkali metal atoms toward gold atoms and into the compound film [5]. These processes may lead to periodic variations in the concentration of alkali metal atoms at certain sites on the surface as a result of competition between surface migration, field-induced desorption, chemical reaction (alkali metal binding to gold), and diffusion of alkali metal atoms in the film of gold and/or compound. Variations in the alkali metal atom concentration would strongly affect the surface work function and the rate of desorption for ions forming the FIDM image.

At the same time, the role of gold may consist in providing certain physical conditions, in particular, a definite work function distribution on the needle surface and a special dependence of this parameter on the alkali metal concentration. This factor, in combination with the surface diffusion, may give rise to a concentration dependence of the desorbing field and, hence, to the observed periodic phenomena.

The phenomena observed in the system studied may have a general character and can be manifested on other surfaces under analogous conditions. These effects should be taken into account in FIDM and in the technology of ion sources involving continuous field-induced desorption. Further investigations into the features of this phenomenon may pour additional light on the process of field-induced desorption, surface diffusion, and surface interatomic interactions.

The authors are grateful to V.I. Paleev for valuable consultations during the work and fruitful discussions of the results. The work was supported by the State Research Program “Surface Atomic Structures,” project no. 3.14.99.

REFERENCES

1. D. P. Bernatskiĭ, Yu. A. Vlasov, and V. G. Pavlov, Zh. Tekh. Fiz. **57**, 2257 (1987).
2. D. P. Bernatskiĭ and V. G. Pavlov, Phys. Low-Dim. Struct. **7**, 93 (1997).
3. E. W. Müller and T. T. Tsong, *Field Ion Microscopy, Field Ionization and Field Evaporation* (Elsevier, New York, 1977; Nauka, Moscow, 1980).
4. W. Spicer, A. H. Sommer, and J. C. White, Phys. Rev. **115**, 57 (1959).
5. M. V. Knat’ko, M. N. Lapushkin, and V. I. Paleev, Pis’ma Zh. Tekh. Fiz. **24**, 48 (1998).

Translated by P. Pozdeev

Technical Physics Letters, Vol. 26, No. 3, 2000, pp. 236–238. Translated from Pis'ma v Zhurnal Tekhnicheskoĭ Fiziki, Vol. 26, No. 6, 2000, pp. 27–31.

Microwave Experiment on a Costas-Array Reflecting Screen

O. I. Kon'kov and A. V. Prikhod'ko

Ioffe Physicotechnical Institute, Russian Academy of Sciences, ul. Politekhnicheskaya 26, St. Petersburg, 194021 Russia

St. Petersburg State Technical University, ul. Politekhnicheskaya 29, St. Petersburg, 195251 Russia

Received June 2, 1999; in final form, November 10, 1999

Abstract—A novel technique to examine thinned-array reflecting screens by means of a microwave interferometer operating at a 8.8 mm wavelength is suggested. The screen is modeled with a 6×6 Costas array, and the standing wave profiles are analyzed for the near-field region of the screen. The results of the experiment show an increase in the fractal dimension of the screen accompanied by a decrease in field strength near the first antinode and by rearrangement of the standing wave profile. © *2000 MAIK "Nauka/Interperiodica".*

As is known, the main problem in the design of thinned-array microwave screens is to synthesize algorithms for the arrangement of reflecting elements so as to obtain optimum reflected signal. It has been theoretically demonstrated that screens with quasi-random arrays provide for the ability to control microwave performance [1]. For example, the fractal dimension of an array controls the distribution of reflected power. This study suggests an experimental technique to reveal the connection between the geometry and the reflection performance of a random array.

In [1], a fractal approach was applied to description of the geometry of a random array, in which the fractal dimension is defined as

$$D = \frac{\log N}{\log r_{\text{ef}}},$$

where N is the number of radiators situated at a distance less than or equal to r, r is the distance to a point assumed to be the origin, $r_{\text{ef}} = \dfrac{8r}{\lambda}$, and λ is the radiation wavelength.

Figure 1 shows examples of the 6×6 Costas arrays, the array numbers being 1, 2, and 12. The array number are arbitrary and correspond to their arrangement in Fig. 23 of [2]. Figure 1 also displays the plots of N versus r for the origin chosen at the left corner of the array in Fig. 2. A distinctive feature of the profiles pertaining to the array groups *A*, *B*, and *C* is a point of inflection at $N = 3$ for groups *A* and *B*. The fractal dimension and reflection performance of such arrays exhibit a change at this point.

We have studied the standing wave profiles as functions of D at a constant element density of the screen (i.e., a constant number of screen array elements per unit area). The measurements were carried out in the near-field region of a random array with 6 elements distributed over a 24×24-mm^2 screen. The standing waves were examined with a microwave interferometer [3, 4]. Specifically, the waves were excited via a 100-μm × 4-mm "bright" slot near a movable screen and their profiles $P(x)$ were traced by varying the distance x between slot *3* and screen *4* (with different arrays) as shown schematically in Fig. 2. The field strength was measured with an antenna situated directly above the slot at a distance of 10λ. The frequency was 33.8 GHz. Three configurations of the array were tested.

The random arrays were modeled by a Costas array [4] comprising half-wave reflecting elements spaced by $n\lambda/2$, where n is an integer. The reflecting elements were $4 \times 4 \times 4$-mm copper–carbon cubes on a foamplastic base.

The results of the experiment are presented in Fig. 3 and the table. They indicate that the increase in fractal dimension from 0.674 to 1.395 (for $N = 6$) amplifies the field strength P_1 at the first antinode, and rearranges (smoothens) the standing wave profile with respect to that obtained with a continuous screen (see curve *F* in Fig. 3). The degree Δ of smoothening at the first antinode was evaluated as the difference between the amplitude at the first antinode and that at the first node (see table).

To sum up, we tested three configurations of a reflecting array at a constant element density of the screen. It has been found that changes in the fractal dimension of the array affect the profile of the standing wave. Thus, a connection between the geometry and the reflection performance of a random array can be established, the reflection being characterized by the near-field reflected intensity and the degree of antinode smoothening. This direction of research can be useful for the creation of passive random reflecting screens or active reflectors with controlled pattern of reflected radiation.

1063-7850/00/2603-0236$20.00 © 2000 MAIK "Nauka/Interperiodica"

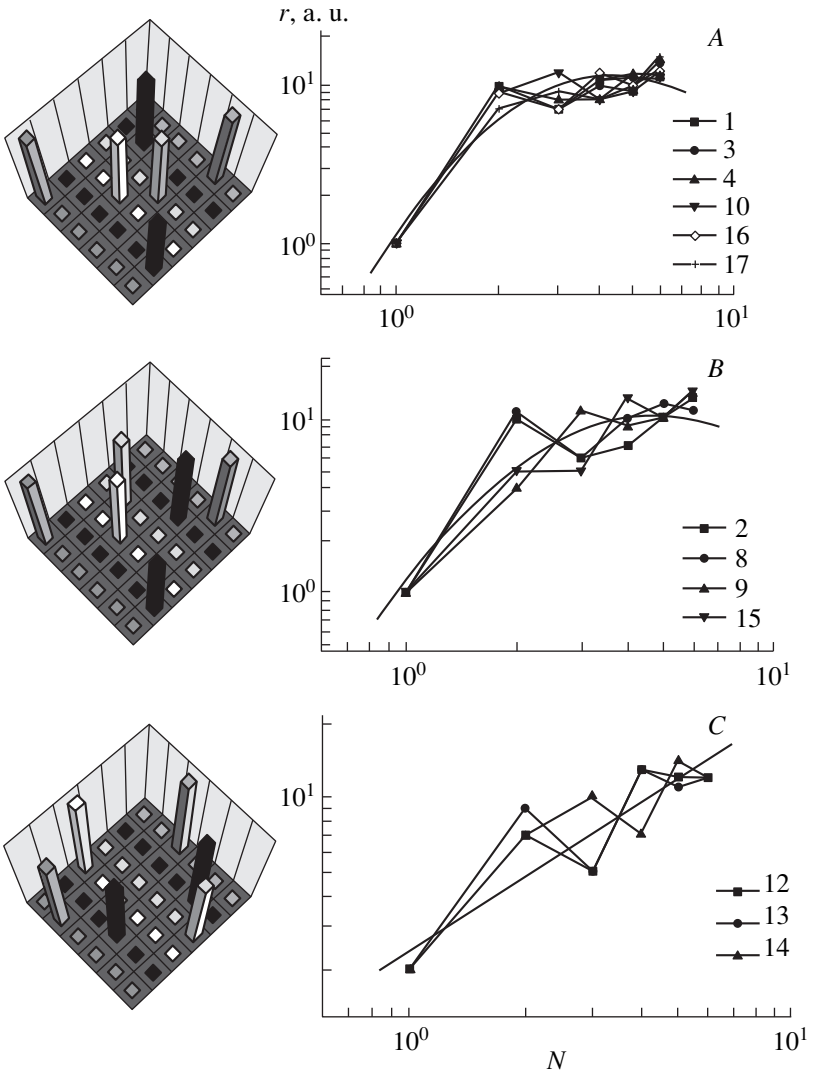

Fig. 1. Plots of the number of radiators N vs. the distance to the origin r for the arrays from classes A, B, and C. The array numbers are given in the boxes. Depicted in the left-hand insets are 6×6 Costas arrays nos. 1, 2, and 12 representing groups A, B, and C, respectively.

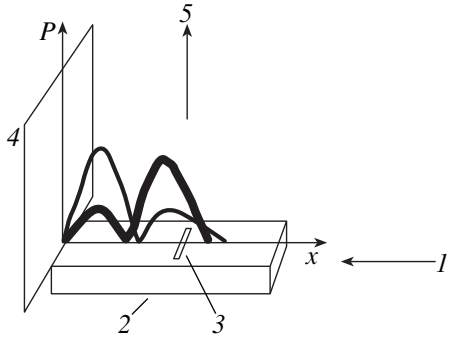

Fig. 2. Schematic drawing of the experimental setup: (*1*) input for the microwave signal from an R2-65 oscillator; (*2*) 8-mm waveguide; (*3*) slot; (*4*) screen; (*5*) radiation output to a horn antenna and an S4-27 amplitude–frequency spectrum analyzer.

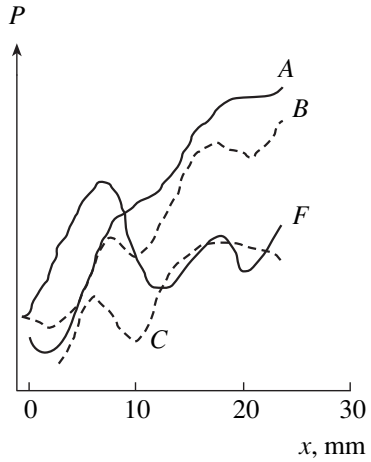

Fig. 3. Typical standing-wave profiles for the Costas arrays from classes A, B, or C and for a continuous screen (F).

Fractal dimensions and microwave characteristics of the Costas arrays

Array no.	D	P_1, a. u.	Δ	Group
1	1.395	35	6	*A*
2	0.972	24	10	*B*
12	0.674	19	14	*C*

This study was supported by the Scientific Council on the Research Direction "Fullerenes and Atomic Clusters," problem 3–2–98.

REFERENCES

1. Y. Kim and D. L. Jaggard, Proc. IEEE **74**, 1278 (1986).
2. S. W. Golomb and H. Taylor, Proc. IEEE **72**, 1143 (1984).
3. M. N. Kotov, V. F. Masterov, A. V. Prichodko, *et al.*, Int. J. Infrared Millim. Waves **14**, 895 (1993).
4. M. N. Kotov, V. F. Masterov, A. V. Prikhod'ko, *et al.*, Proc. SPIE **2250**, 322 (1994).

Translated by A. A. Sharshakov

Technical Physics Letters, Vol. 26, No. 3, 2000, pp. 239–240. Translated from Pis'ma v Zhurnal Tekhnicheskoĭ Fiziki, Vol. 26, No. 6, 2000, pp. 32–35.

Transient Optical Phenomena in Quartz Fibers under High-Power Pulsed Reactor Irradiation

P. V. Demenkov, O. A. Plaksin, V. A. Stepanov, P. A. Stepanov, and V. M. Chernov

Institute of Physics and Power Engineering, Obninsk, Russia

Received November 11, 1999

Abstract—Measurements of the intensity of emission and induced optical absorption at 400–750 nm in KU-1 quartz fibers were performed under pulsed irradiation in a BARS-6 reactor (pulse duration, 80 μs; dose per pulse, up to 5×10^{12} neutrons/cm^2 ($E > 0.2$ MeV); dose rate, up to 10^5 Gy/s). The nondelayed emission component is due to the Cerenkov radiation, the weak relaxation component has a relaxation time of ~150 ± 50 μs, and the radiation-induced optical absorption reaches a value of 2.5×10^{-4} cm^{-1} (relaxation time, 600–1200 μs). A nonlinear dependence of the Cerenkov radiation on the dose rate and the presence of the relaxation emission component and the transient optical absorption may be associated with an optical inhomogeneity of glass induced by the high-power reactor irradiation. © *2000 MAIK "Nauka/Interperiodica".*

When optical fibers are used in radiation fields, there arises a problem of separating and estimating the contributions to optical signals due to the radiation-induced luminescence (RIL), Cerenkov radiation, and radiation-induced (including transient) optical absorption (RIOA). In the case of steady-state irradiation, it is impossible to reliably differentiate the contributions of RIL and Cerenkov radiation to the fiber emission. In addition, the structural features of the radiation devices employed (fission reactors, accelerators, gamma-sources), as a rule, restrict the length of fibers being tested (to 1 m), which hinders the measurement of variations of the absorption coefficient below 10^{-3} cm^{-1} (see, for example, [1]). Therefore, most of the available data on RIOA are associated with irreversible changes in fibers rather than with weaker transient absorption. In view of this, we investigated the kinetics of emission and optical absorption of KU-1 quartz fibers under the conditions of pulsed irradiation in a BARS-6 reactor (pulse duration, 80 μs; dose per pulse, up to 5×10^{12} neutrons/cm^2 ($E > 0.2$ MeV); dose rate, up to 10^5 Gy/s).

The measurements were performed on the optical fibers with a core of KU-1 glass, a fluorosilicate light-reflecting sheath, and an acrylate protective coating (manufactured by the Scientific Center of Fiber Optics at the Institute of General Physics, Russian Academy of Sciences). The fibers 100 μm and 1 mm in diameter were wound on reels (to a total length of 20 and 3 m, respectively).

In order to differentiate between the emission and RIOA components, we recorded the optical signals (wavelength, 488 and 630–635 nm; time resolution of up to 100 ns) due to the intrinsic emission of thin fibers and the emission induced by probing this fiber with the light of an incandescent lamp. The nondelayed component is most intense in the curve of emission kinetics (Fig. 1): the emission maximum corresponds to the maximum of neutron pulse (i.e., to the maximum of the intensity of gamma-radiation accompanying the neutron pulse). The nondelayed component is followed, over a time of 50 μs from the maximum, by the relaxation component identified in this case with RIL. The results of measurements of the intensity of emission from a fiber with the 1-mm-diam core demonstrated that the spectral efficiency of conversion of the energy of absorbed ionizing radiation to optical emission of the fiber does not exceed 10^{-6} nm^{-1}. In the range of 400–750 nm, the integral efficiency is ~10^{-4}. The relaxation time of RIL in the thick fiber was ~150 ± 50 μs and did not vary over a period of 100 irradiation pulses (total dose, 5×10^{14} neutrons/cm^2 ($E > 1$ keV)).

At 630–636 nm, we managed to register the transient absorption with a peak value of 2.5×10^{-4} cm^{-1} (580 dB/km). This value is twice the initial level and corresponds to an ionizing efficiency of ~2.5×10^{-9} cm^{-1}/Gy s. The characteristic relaxation time of RIOA ranges from 600 to 1200 μs, and the RIOA delay relative to the maximum of neutron pulse is 20 μs. At 488 nm, the maximum RIOA does not exceed 10^{-4} cm^{-1}.

The nature of the relaxation emission component (RIL) is not clear. This component is not associated with relaxation of the oxygen-deficient centers, for which the time constant is much greater (~30 ms) [2]. Because the relaxation component shows up in the entire spectral range of measurements (400–750 nm), it cannot be associated with any other centers in glass either.

The nondelayed emission component is apparently associated with the Cerenkov radiation [1, 3]. Given the fixed dose rate of ionizing radiation, the spectral intensity of this emission component decreases with increas-

1063-7850/00/2603-0239$20.00

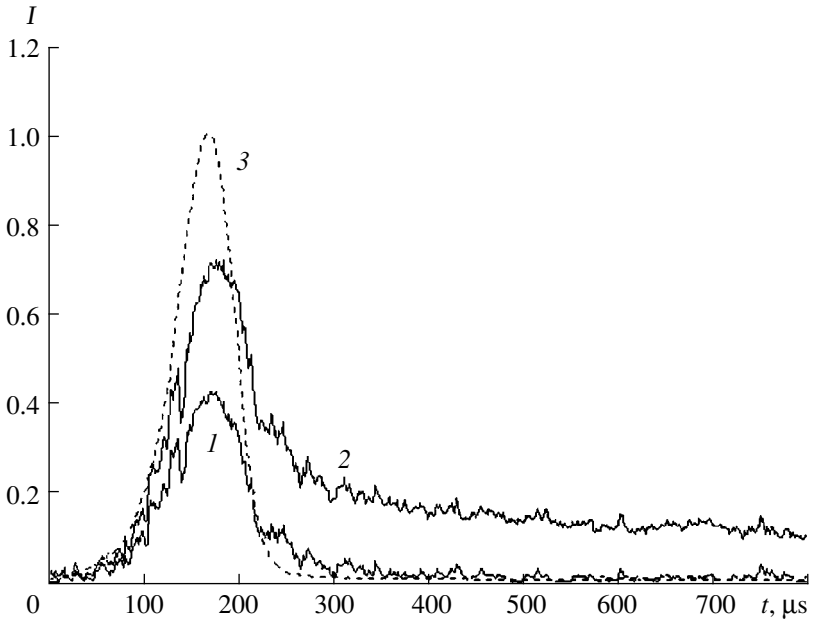

Fig. 1. Time variation of (*1*) glow intensity at 630–636 nm (in relative units), (*2*) optical density, and (*3*) fast neutron flux density (normalized to unity).

ing wavelength (λ) as $1/\lambda^3$ (Fig. 2). However, this emission intensity is not proportional to the dose rate, as one would expect for the Cerenkov radiation, but has a power dependence with an exponent of 0.7 ± 0.05 (the exponent is calculated for the fronts of emission and neutron pulses). The deviation from linear relationship is not associated with optical losses, because the intensity was measured after separating the contributions of emission and RIOA (Fig. 1). One can assume that this nonlinearity is due to the variation of the conditions of generation of the Cerenkov radiation with increasing dose rate. The optical inhomogeneity of the medium (glass) increases with the density of electron excitations. The resulting decrease of coherent radiation leads to a decrease in the Cerenkov radiation yield. Simultaneously, the optical transmission of fiber decreases as a result of scattering from the inhomogeneities of the medium, which is manifested by the RIOA pulse.

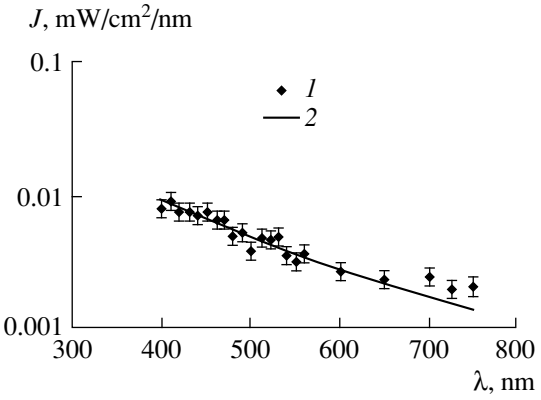

Fig. 2. (*1*) The spectral intensity of emission J at the fiber output for the ionizing dose rate of 8×10^4 Gy/s and (*2*) the shape of the Cerenkov radiation spectrum.

This study received support from the Russian Foundation for Basic Research (project no. 98-02-03571).

REFERENCES

1. T. Shikama, T. Kakuta, M. Narui, *et al.*, J. Nucl. Mater. **212–215**, 421 (1994).
2. R. Tohmon, Y. Shimogaichi, H. Mizuno, Y. Ohki, *et al.*, Phys. Rev. Lett. **62**, 1388 (1989).
3. W. Schneider and U. Babst, Proc. SPIE **506**, 189 (1984).

Translated by Henri A. Bronsteĭn

Technical Physics Letters, Vol. 26, No. 3, 2000, pp. 241–242. Translated from Pis'ma v Zhurnal Tekhnicheskoĭ Fiziki, Vol. 26, No. 6, 2000, pp. 36–40.

The Amplitude of Electric Response as a Function of the Spatial Arrangement of Filler Particles in Mechanically Excited Concrete

V. V. Lasukov and T. V. Fursa

Tomsk Polytechnic University, Tomsk, Russia

Received April 1, 1999; in final form, September 29, 1999

Abstract—Experimental investigation is performed and a model is suggested of the phenomenon of electric signal generation under conditions of mechanical excitation of a medium consisting of a dielectric immersed in a poor conductor. © *2000 MAIK "Nauka/Interperiodica".*

This paper deals with a theoretical and experimental investigation of the dependence of the amplitude of electric signal on the spatial arrangement of filler particles during the mechanical excitation of concrete.

Quite long ago, the phenomenon of electrization of newly forming surfaces under conditions of deformation and fracture of crystals was observed and reported in [1–4]. The electrization of a material is due to the breakage of ionic bonds during the propagation of cracks in the material, the motion of charged dislocations, and the adhesion or electrokinetic phenomena. However, details of this phenomenon that are of practical importance, such as the spatial arrangement of charges, the process of charge formation, the correlation between the characteristics of electric signal generated during the motion of such charges and the physicochemical properties of the loaded body, and the time evolution of the fracture process, have not been adequately studied.

In view of this, we have performed theoretical and experimental investigations of the dependence of the amplitude of electric response signal on the spatial arrangement of the filler particles (pebble) under conditions of mechanical excitation of concrete.

The experimental investigations of the effect of electric signal generation by a mechanically disturbed medium were performed according to the following scheme. The measurements were taken with the aid of a capacitive sensor with a differential input [5], which was arranged at a distance of the order of 0.1–1 cm above the sample surface. The opposite face of the sample was arranged on a grounded metal surface with an area of the order of 1 m^2. In this arrangement, the external measuring system was a capacitor formed by the grounded surface and the sensor surface. The use of this sensor and grounded surface enables one to eliminate the noise and perform experiments without employing a shield. Mechanical vibrations were excited by a single normalized impact of a vibrator. For this scheme of measurements and the impact excitation method, an instrument registers the bias current due to the emergence and variation in time of the dipole moment of the electric double layer of the surface charges. The magnitude and three-dimensional structure of surface charges and their vibration amplitudes depend on the physicochemical properties of bulk regions of the samples investigated.

For a surface radiator model, the voltage at the instrument input is [5]

$$U(h, t) = U_0(t)\frac{1}{h}\left[1 - \left(1 + \frac{R_{\max}^2}{h^2}\right)^{-1/2}\right]\left\{h + \frac{d_0 S_s}{\varepsilon S_0}\right\}, \quad (1)$$

where $U_0(t) = E_0 x(t)$, $E_0 = \dfrac{4\pi\sigma_s}{\varepsilon_0}$, $x(t)$ is the charge shift, σ_s is the surface charge density, ε is the relative permittivity of the sample, d_0 is the linear dimension of the sample, S_s is the area of the sensor, S_0 is the area of the sample face beneath the sensor, and h is the distance from the sample surface to the sensor. The term in braces in expression (1) is defined by the impedance Z and represents the instrumental factor.

Based on the study of dependence (1) of the signal amplitude on the distance between detector and sample surface, it was experimentally shown [5] that the source of electric signal is provided by charged regions of the external surface of the sample. It was suggested that the surface charge is induced either by the volume charges or by the dipole moment of charges located inside the body and formed on inhomogeneities.

In view of this, let us find the surface charge density, which may be estimated by calculating the flow of vector E (due to the charge inside the sample) through the sample surface G over which the sensor is located. We have

1063-7850/00/2603-0241$20.00

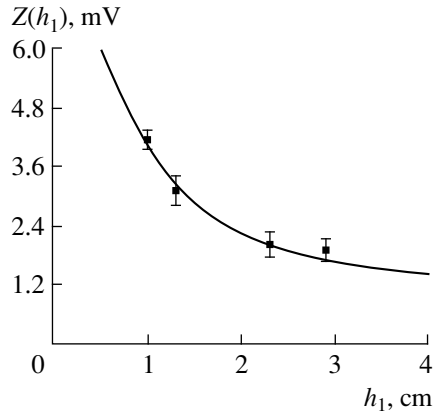

The plot of the function $z(h_1) = \sigma_s(h_1) + \sigma_d(h_1)$ versus the depth h_1 of source location in the sample. The points indicate experimental data. The solid line shows the results of calculation according to the theory.

performed the calculation for a cubic sample to derive

$$\sigma_s = \frac{4\pi\varepsilon_0\varepsilon}{S}\iint_G (\mathbf{E}\cdot\mathbf{n})dS = \sigma_0\sum_{j=1}^{4}\arctan[\varphi_j(h_1, h_2, h_3)], \quad (2)$$

where $\sigma_0 = \frac{Q}{S}$, Q is the magnitude of the charge inside the sample, S is the surface face area of the cubic sample,

$$\varphi_1(h_1, h_2, h_3) = \frac{h_2h_3}{h_1\sqrt{h_1^2 + h_2^2 + h_3^2}},$$

$$\varphi_2(h_1, h_2, h_3) = \varphi_1(h_1, L - h_2, h_3),$$

$$\varphi_3(h_1, h_2, h_3) = \varphi_1(h_1, h_2, L - h_3),$$

$$\varphi_4(h_1, h_2, h_3) = \varphi_1(h_1, L - h_2, L - h_3),$$

$h_{1,2,3}$ denotes the distances from the charge to three faces of the sample, h_1 is the distance from the charge to the sample surface facing the sensor, and L is the length of the cube edge.

For a source located inside the sample and possessing a nonzero specific dipole moment, one can analogously derive

$$\sigma_d = \sigma_{0d}\frac{1}{h_1}\sum_{j=1}^{4}\arctan(\varphi_j(h_1, h_2, h_3)), \quad (3)$$

where l is the linear dimension of the dipole. We performed an experiment to check the validity of relations (2) and (3). For this purpose, four $10 \times 10 \times 10$ cm cubic samples of concrete were manufactured, each accommodating only one assumed volume source (pebble) located at a certain depth. Each sample is an inhomogeneous material consisting of a dielectric element immersed in a poor conductor. In the first sample, the source was located at a point on the axis passing through the geometric centers of two opposite faces of the cube at a distance $h_1 = 1$ cm from the sample surface facing the sensor; in the second sample, $h_1 = 1.3$ cm; in the third sample, $h_1 = 2.3$ cm; and in the fourth sample, $h_1 = 2.9$ cm. The following values of the signal amplitude were observed at the instrument input: 4.16, 3.12, 2.00, and 1.92 mV, respectively. The sensor was always placed at the same distance from the sample surface.

The function $Z(h_1) = \sigma_s(h_1) + \sigma_d(h_1)$ is plotted in the figure.

Good agreement between theory and experiment leads one to the following conclusions.

The dielectric component (pebble) located inside the body possesses a specific dipole moment of mechanical nature and a volume charge. Apparently, the dipole moment is due to the gradient of mechanical stresses arising in the inhomogeneous material.

Our results may serve as an experimental proof of the surface radiator model used to explain the anomalies in the natural electromagnetic field of the Earth that arise on the eve of earthquakes.

The procedure employed by us may be used to investigate development of the fracture process and to verify the inferences of the corresponding theories (especially, the inference of the percolation theory of fracture [6] that the slope and linearization of the graph of the so-called law of recurrence may serve as a prognostic sign of destruction). In addition, the equipment and procedure developed for investigation and utilization of the phenomenon of generation of electric signal by loaded bodies are ideally suited for studying the predicted, but not experimentally investigated, flexoelectric effect [7]. It is important to study the fracture process in view of the fact that this process may underly the low-temperature nuclear fusion [8].

REFERENCES

1. B. V. Deryagin, N. Krotova, and V. G. Smilga, *Adhesion of Solids* (Nauka, Moscow, 1973).
2. A. A. Urusovskaya, Usp. Fiz. Nauk **86**, 39 (1968) [Sov. Phys. Usp. **86** (1968)].
3. V. M. Finkel', *Physical Principles of Deceleration of Destruction* (Metallurgiya, Moscow, 1977).
4. N. G. Khatiashvili, Izv. Akad. Nauk SSSR, Fiz. Zemli, No. 9, 13 (1984).
5. T. V. Fursa, V. F. Gordeev, V. V. Lasukov, and Yu. P. Malyshkov, Pis'ma Zh. Tekh. Fiz. **20**, 1 (1994) [Tech. Phys. Lett. **20**, 853 (1994)].
6. T. L. Chelidze, *Methods of the Percolation Theory in the Mechanics of Geomaterials* (Nauka, Moscow, 1987).
7. D. K. Tagantsev, Usp. Fiz. Nauk **152**, 423 (1987) [Sov. Phys. Usp. **30**, 588 (1987)].
8. V. A. Tsarev, Usp. Fiz. Nauk **160**, 1 (1990) [Sov. Phys. Usp. **33**, 881 (1990)].

Translated by Henri A. Bronsteĭn

Technical Physics Letters, Vol. 26, No. 3, 2000, pp. 243–246. Translated from Pis'ma v Zhurnal Tekhnicheskoĭ Fiziki, Vol. 26, No. 6, 2000, pp. 41–52.

A Multipurpose Holographic Optical Wedge: Theory, Design, and Applications

I. A. Novikov

Mendeleev All-Russia Research Institute of Metrology, State Scientific Center, St. Petersburg, Russia

Received November 9, 1999

Abstract—Theory, design, and some applications of a holographic wedge are considered. The device is an optical wedge inside which a transmission or reflection Bragg grating is recorded. Application to wavelength-division multiplexing in optical-fiber data transmission lines is discussed. An experiment on a reflection-grating holographic wedge is reported. © *2000 MAIK "Nauka/Interperiodica".*

INTRODUCTION

This paper expands on the theory, design, and potential applications of a holographic optical wedge (HW), which was suggested in [1, 2] as a means of wavelength-division multiplexing and demultiplexing in optical-fiber data transmission lines. The HW is an optical wedge with flat faces, containing a transmission or reflection Bragg grating recorded as a phase volume hologram. Previously [1, 2], we used a simplest HW implementing a transmission grating with inclined equiphase surfaces, first-order diffracted beams emerging almost perpendicularly to the wedge face. Due to the total internal reflection at the boundaries, a zero-order beam passes through the HW a number of times (Fig. 1). A disadvantage of this scheme is that the zero-order beam of each multiplexed channel must pass through the HW twice.

The HW could be useful in the following areas: (1) wavelength-division multiplexing in optical-fiber communications; (2) the compression of ultrashort pulses, e.g., chirp pulses; (3) multi-longwavelength interferometry; (4) the optical-fiber networks of multichannel transducers implementing the FBG technologies; (5) simultaneous analysis of optical radiation in terms of wavelength and polarization; (6) optical analog–to–digital conversion and optoacoustic multichannel switching; and (7) the optical realization of one- and two-dimensional wavelet transforms and related data processing systems.

Obviously, the specific features of an HW depend on its application. This paper presents general theory and considers two advanced versions of the device designed for the systems of wavelength-division multiplexing in optical-fiber communications, implementing either a transmission or a reflection symmetric holographic grating. The computed and measured performance characteristics of these systems are given as well.

TRANSMISSION-GRATING DEMULTIPLEXER

The HW may be designed in various ways, each having certain advantages. This paper suggests an HW, which possesses a simple structure and is easy to fabricate, together with a multiplexer built around the HW.

In development of the scheme proposed in [1, 2], we suggest using a compound HW comprising three optical elements: two identical glass wedges and a holographic plate with recorded symmetric phase volume transmission grating (Fig. 2). The HW is assembled through immersion or by using optical contacts. The refractive index of the glass wedges equals the average index of the holographic medium. Metallic or interference thin-film reflective coatings are deposited onto the exterior faces of the HW (Fig. 2). The HW configuration is designed so that a zero-order diffracted beam (the input beam) passes through the HW many times, reflecting from the coatings, whereas the first-order beam leaves the HW freely. (The configuration parameters are the angle of incidence for the input beam, β_1 the dimensions and position of the reflecting coatings, the hologram thickness h, and the wedge thickness h_1.) The input light beam is coupled via gradient-index lens

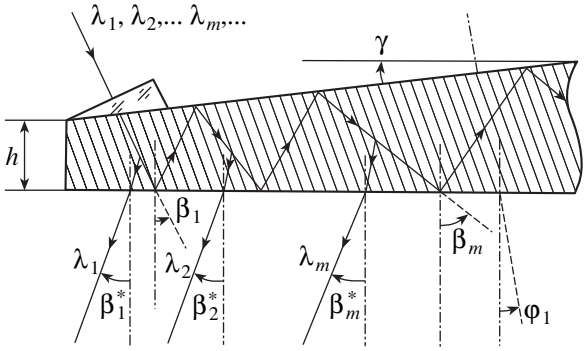

Fig. 1. Wavelength-division multiplexing and demultiplexing with the holographic wedge.

1063-7850/00/2603-0243$20.00 © 2000 MAIK "Nauka/Interperiodica"

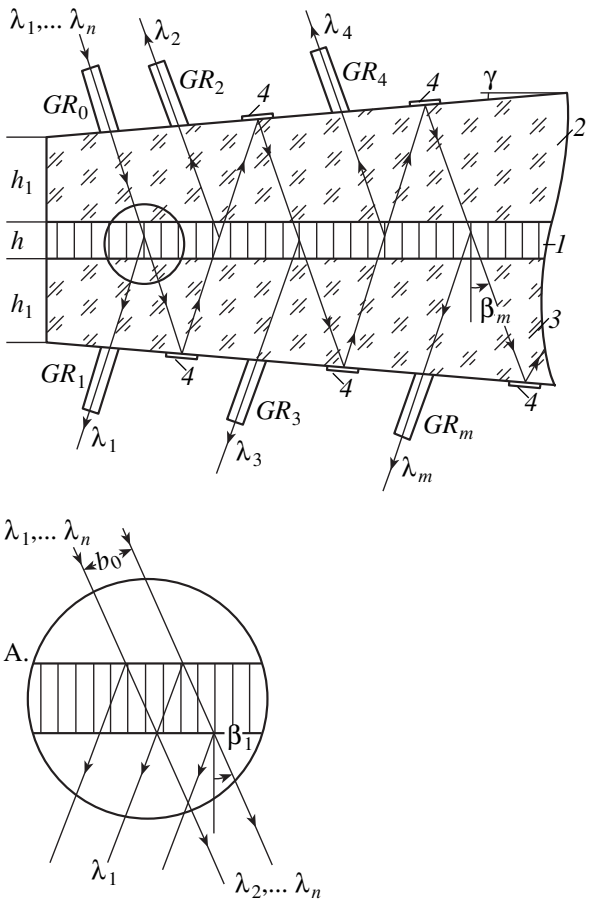

Fig. 2. Wavelength-division demultiplexer with a transmission grating: (*1*) hologram; (*2*) and (*3*) optical wedges; (*4*) reflective coatings.

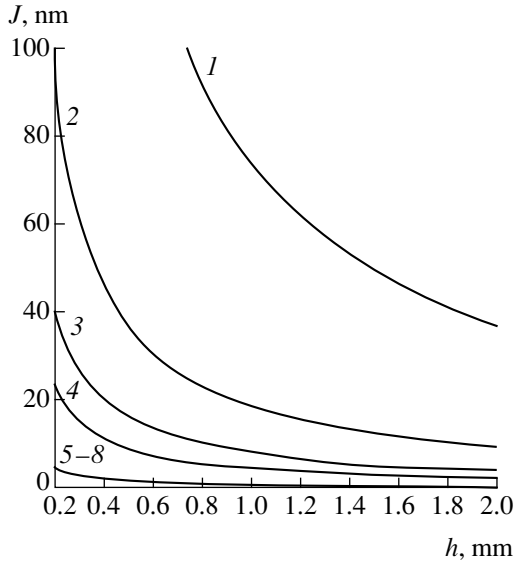

Fig. 3. Demultiplexer: wavelength resolution vs. hologram thickness at an input angle of (*1*, *5*) 0.1, (*2*, *6*) 0.2, (*3*, *7*) 0.3, or (*4*, *8*) 0.4 (rad). Curves *1–4* correspond to a transmission grating, and curves *5–8* to a reflection grating.

GR_0, and the output beam, via the transmission interference coatings or the gradient-index lenses GR_m (Fig. 2).

Since the device is a wedge, the angle between the direction of propagation and the equiphase surfaces of the grating increases with each reflection. The angular increment is proportional to the reflection number m, and the HW region where diffracted light emerges depends on the wavelength, λ_m (according to the Bragg condition).

Now, consider a wavelength-division multiplexer using the HW. The light beam geometry depicted in Fig. 2 suggests that

$$b_m = b_0/\cos\beta_m, \quad h_m^* = b_0/\cos\beta_m + h\tan\beta_m, \quad \beta_m = \beta_1 + m\gamma, \tag{1}$$

where b_m is the width of the input beam, h_m^* is that of the diffracted output beam (without allowance for the diffraction and angular divergence), and γ is the wedge angle. The condition of the spatial separation of zero- and first-order beams places the following constraint on the glass wedge thickness:

$$h_1 > b_0\cos^2\beta_m/2\sin\beta_m. \tag{2}$$

For demultiplexer with m channels, the required clear aperture D_m of the hologram can be estimated as

$$D_m \cong m(2h_1 + h)\tan\beta_m + b_m. \tag{3}$$

For the mth channel, the wavelength resolution and angular resolution are as follows:

$$\delta\lambda_m = \lambda_m\delta\theta_m; \quad \delta\theta_m = \lambda_m\cot\beta_m/2nh\sin\beta_m. \tag{4}$$

Formulas (4) are borrowed from [1–3] with necessary modifications.

Dependence of the demultiplexer resolution on the hologram thickness (at $\lambda = 1.5$ μm) is depicted in Fig. 3.

Optical losses can be computed using the formulas derived in [1]. The component wedges can be made of high-quality glass with a small absorption coefficient. The dielectric interference reflective HW boundary coatings may have a reflection coefficient as high as 99.99%. The optical coupling may be realized via gradient-index devices having optical contact with the HW. Thus, the overall losses P_m of the demultiplexer consist predominantly of the hologram absorption losses B_m, the diffraction losses η_m, and the input and output coupling losses, D_0^* and D_m^*:

$$P_m = D_0^* + D_m^* + B_m + 10|\log\eta_m|. \tag{5}$$

Here,

$$B_m = K_\lambda l_m; \quad l_m = l_{m-1} + h/\cos\beta_m; \quad l_1 = h/\cos\beta_1; \tag{6}$$

K_λ is the absorption coefficient of the holographic medium, and l_m is the distance travelled by the

*m*th-channel beam in the hologram. In computation, K_λ was taken equal to a standard value and l_m was assumed to be approximately $mh/\cos\beta_1$.

The demultiplexer exhibits lower optical losses as composed to the earlier version [1, 2]. This mainly results from the number of passes being decreased twofold and gradient-index lenses being used at the output.

There are two ways to improve the performance of the demultiplexer. The first consists in using several different superimposed holograms instead of a single hologram, which enables one to combine serial and parallel diffraction modes. This would allow the absorption losses to be reduced. However, the idea is difficult to implement.

The second way is to employ a volume phase reflection grating instead of the transmission hologram. The reflection hologram offers better wavelength resolution (see curves *5*–*8* in Fig. 3) and, hence, lower optical losses and crosstalk.

REFLECTION-GRATING DEMULTIPLEXER

The reflection-grating demultiplexer is schematically shown in Fig. 4. The notation is the same as in Fig. 2, and formulas (1)–(3) remain valid.

For an $(m-1)$th and an mth diffracted beam, the Bragg condition $\lambda_m = 2dn\cos\beta_m$ implies that

$$\Delta\lambda_m = \lambda_{m-1}\gamma\tan\beta_{m-1}, \tag{7}$$

where $\Delta\lambda_m = \lambda_m - \lambda_{m-1}$. Here, we use the condition that γ is small ($\gamma < 1$ and $\gamma < \beta_1$): as a rule, the angle is less than 1.0°–1.5°. Thus, $\Delta\lambda_m$ is a linear function of γ.

For the mth channel, the wavelength resolution and the angular resolution are calculated by the well-known formulas [3]:

$$\begin{aligned}\delta\lambda_m &= \xi_0\lambda_m^2/(2nh\pi\cos\beta_m),\\ \delta\theta_m &= \xi_0\lambda_m/(2nh\pi\sin\beta_m),\end{aligned} \tag{8}$$

where ξ_0 corresponds to zero diffraction efficiency. Note that $\xi_0 = 3.5$ for an important particular case of $\nu = \pi/2$ [3].

A photopolymer hologram of thickness $h = 1$ mm provides a wavelength resolution of the order of 1 nm at $\lambda = 1.5$ μm. A very thick hologram ($h = 1$ cm) can provide for 0.2 Å.

Good wavelength resolution [see (8)], together with low losses and crosstalk, require that the input beam would have a small angular divergence, $\delta\theta_0$. Let us estimate the upper limit for the divergence.

For the mth channel, the diffraction efficiency of a reflection-grating demultiplexer is calculated as follows [3]:

$$\eta_m = [1 + (1-(\xi/\nu)^2)\sinh^{-2}(\nu^2-\xi^2)^{1/2}]^{-1}. \tag{9}$$

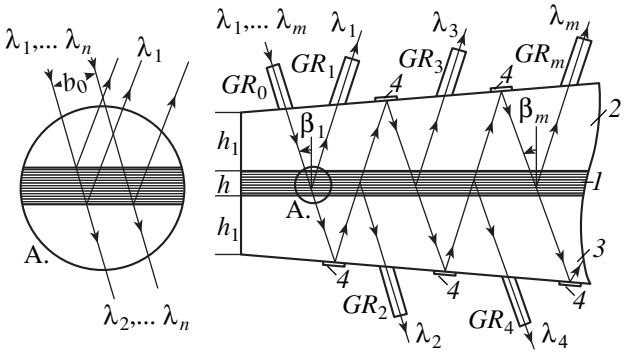

Fig. 4. Wavelength-division demultiplexer with a reflection grating. The notation is the same as in Fig. 2.

It can be demonstrated that, taking into account the angular and wavelength divergence at a small incidence angle β_m ($\beta_m < 1$) the parameters in equation (9) can be expressed as

$$\begin{aligned}\xi &= 2nh\pi[(\delta\theta)^2/2 - \delta\lambda/\lambda_m]/\lambda_m;\\ \nu &= \pi n_1 h/\lambda_m.\end{aligned} \tag{10}$$

The angular divergence of the input beam can be expressed in terms of the Gaussian function:

$$f(\theta) = \exp[-(2\theta/\delta\theta_0)^2], \tag{11}$$

where $\delta\theta_0$ is the angular divergence at the level e^{-1}.

For a divergent input beam possessing radial symmetry, the total internal reflection R of the diffracted beam is evaluated as

$$R = \int\eta(\theta)f(\theta)d\theta/\int f(\theta)d\theta, \tag{12}$$

where integration is performed over the entire range of input angles.

In the typical case $\nu = \pi/2$, the right-hand side of (9) is approximated as

$$\eta = \exp[-(\xi/\pi)^2], \tag{13}$$

where ξ is computed by (10) and side grating lobes are neglected. Calculating the integrals in (12) gives

$$\begin{aligned}R &= \pi^{1/2}p\exp(p^2 - 2p\xi_1/\pi)\mathrm{erfc}(p-\xi_1/\pi),\\ \xi_1 &= 2nh\pi\delta\lambda_m/\lambda_m^2; \quad p = 2\lambda_m/(nh(\delta\theta_0)^2),\end{aligned} \tag{14}$$

where $\mathrm{erfc}(x)$ is the error function [4]. An increase in the input angular divergence (i.e., a decrease in p) leads to lower diffraction efficiency. Computation demonstrates that (14) transforms into (13) (with ξ replaced by ξ_1) for $p > 5$ and that the approximation error is less than 0.01. We thus arrive at the upper estimate for the

angular divergence of the incident beam:

$$\delta\theta_0 < 0/632(\lambda_1/nh)^{1/2}. \quad (15)$$

For the above photopolymer hologram (h = 1 mm and λ= 1.5 μm), $\delta\theta_0$ must not exceed 2°.

The optical losses can be evaluated from (5) and (6). In practice, η_m may attain 0.8–0.9. The crosstalk level can be found by means of the formalism from [1].

EXPERIMENTAL RESULTS AND CONCLUSIONS

We carried out an experiment on a compound HW with a reflection phase grating and metal reflective coatings (Al mirrors). The photograph of the HW is presented in Fig. 5. The HW was assembled using immersion. The hologram was recorded in a PMMA PQ photopolymer, the parameters being h = 0.4 mm and λ = 511 μm. The wavelength-selectivity curve (obtained with a tunable dye laser) is shown in Fig. 6. The base wavelength resolution of the hologram was 5 Å, and the maximum diffraction efficiency was 0.7 (for λ = 511 nm). The reflection coefficient of the Al mirrors was 90%.

Fig. 5. Photograph of the holographic wedge.

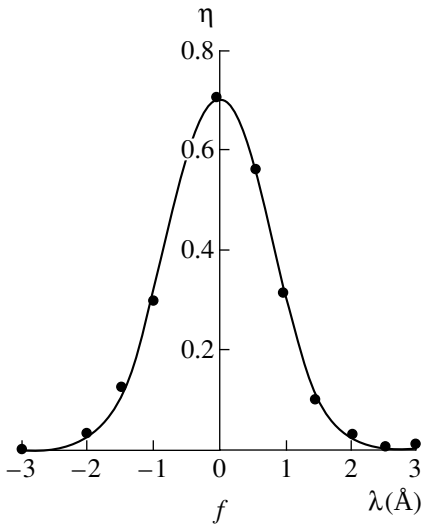

Fig. 6. Wavelength selectivity of the reflection grating used in the holographic wedge.

The experimental setup included a xenon lamp, a collimator, a double monochromator, and a multiplier phototube and was linked to a personal computer. The wavelength resolution $\Delta\lambda$ was measured to be 2.7–3.0 Å (the computed value being 4 Å). Six multiplexed wavelength channels were observed. The intensity attenuation ratio for two adjacent channels was 0.5–0.6. We attribute this to diffraction cross coupling (overlap of the diffraction efficiencies of the adjacent HW channels). With an allowance for this effect, the computed value of the intensity attenuation ratio increases to 0.6–0.7.

To sum up, the experimental results are in close agreement with the theory, showing that it is possible to create an HW-based wavelength-division demultiplexer offering good wavelength resolution and accommodating many channels. Specifically, the resolution can reach a few angstroms or even a fraction of an angstrom and more than ten channels can be multiplexed.

With certain modifications, the HW versions suggested here could also be employed in multi-longwavelength interferometers, optical-fiber transducers (using the FBG technology), chirp-pulse compressors, and optical devices implementing one-dimensional wavelet transforms. Some of the applications will be discussed in subsequent publications.

REFERENCES

1. I. A. Novikov, Pis'ma Zh. Tekh. Fiz. **24**, 76 (1998).
2. I. A. Novikov, in *Program and Abstracts of CLEO/QELS'95, May 21–26, 1995, Baltimore, USA*, p. 86.
3. R. J. Collier, C. B. Burckhardt, and L. H. Lin, *Optical Holography* (Academic Press, New York, 1971; Mir, Moscow, 1973).
4. G. A. Korn and T. M. Korn, *Mathematical Handbook for Scientists and Engineers: Definitions, Theorems and Formulas for Reference and Review*, 2nd ed. (McGraw-Hill, New York, 1968; Nauka, Moscow, 1984).

Translated by A. A. Sharshakov

Technical Physics Letters, Vol. 26, No. 3, 2000, pp. 247–249. Translated from Pis'ma v Zhurnal Tekhnicheskoĭ Fiziki, Vol. 26, No. 6, 2000, pp. 53–58.

Interaction of an Optically Dense Bose Condensate with a Resonant Laser Pulse

I. E. Mazets, B. G. Matisov, and I. V. Kazinets

Ioffe Physicotechnical Institute, Russian Academy of Sciences, St. Petersburg, Russia

St. Petersburg State Technical University, St. Petersburg, Russia

Received November 10, 1999

Abstract—Propagation of a resonant laser pulse through an optically dense Bose–Einstein condensate is theoretically investigated. Changes in the spatial distribution of the condensate after the laser pulse propagation are analyzed. It is shown that atoms escape from the condensate due to the joint action of two factors: the transition of atoms from the ground state to an excited state upon absorption of the resonant photons and the effect of a zero-result measurement. The latter effect is interpreted in terms of the theory of quantum measurements.

The Bose–Einstein condensate (BEC) was produced for the first time [1, 2] with cooled alkali-metal atoms in magnetic traps. Currently, the main method of detection and investigation of BEC implies the registration of resonant laser radiation scattered by a condensate and processing of the resulting signal. A detailed theoretical analysis of the interaction of resonant laser radiation with an optically thin BEC was performed, for example, by Javanainen [3]. However, development of the experimental techniques results in the increasing number of atoms in a condensate, necessitating the development of a consistent theory that would describe the interaction of laser radiation with an optically dense BEC.

In this paper, we consider the one-dimensional propagation of a resonant laser pulse in an optically dense BEC in a trap with an effective (averaged in time) potential $U(x)$. To simplify the calculations, we assume that the trap potential can be represented as a rectangular well with infinitely high walls. The left- and right-hand walls of this potential well are assumed to have the coordinates 0 and L, respectively. At the initial moment of time, all atoms occur in the ground state of the trap potential.

Suppose that the intensity of laser radiation is far from the level of saturation, and we can write the excitation rate of an atom as $\sigma u(x, t)/\hbar\omega$, where σ is the cross section of absorption of a photon by an atom, $\hbar\omega$ is the photon energy, and $u(x, t)$ is the intensity of laser radiation. The propagation equation for the laser radiation intensity is written as

$$\frac{\partial}{\partial x}u + \frac{1}{c}\frac{\partial}{\partial t}u = -\sigma\langle\hat{\psi}^{+}(x, t)\hat{\psi}(x, t)\rangle u. \qquad (1)$$

The right-hand side of this equation involves a term describing absorption of the laser pulse, which is proportional to the density of the condensate, the intensity of the laser pulse, and the effective cross section of absorption of a photon by an atom. We assume that the radiation frequency ω is exactly equal to the atomic transition frequency, and the boundary and initial conditions are written as $u(0, t) = u_0(t)$ and $u(x, -\infty) = 0$, $x > 0$.

The equation for the atomic field operator $\hat{\psi}(x, t)$ governing the condensate can be represented as

$$\frac{\partial}{\partial t}\hat{\psi}(x, t) = -\frac{i}{\hbar}\hat{H}\hat{\psi}(x, t) - \frac{\sigma}{2\hbar\omega}u(x, t)\hat{\psi}(x, t), \quad (2)$$

where $\hat{H}$ is the Hamiltonian that includes the kinetic energy of atoms, the internal energy of atoms (corresponding to their electron states), and the trap potential. The second term on the right-hand side of (2) is responsible for the escape of excited atoms from the condensate. For simplicity, we assume that an atom absorbing a photon never returns to the condensate. In other words, we exclude a contribution related to the elastic scattering of light, leaving the BEC state unchanged, from the cross section.

Expanding the atomic field operator in the eigenfunctions $\varphi_k(x)$ of the operator $\hat{H}$, we obtain

$$\hat{\psi}(x, t) = \sum_{k=0}^{\infty}\varphi_k(x)\hat{b}_k(t), \qquad (3)$$

where $\hat{b}_k(t)$ are the annihilation operators for the state k.

Equation (2) can be interpreted in terms of the quantum theory of measurements [4]. Let us consider, for example, a quantum system occurring in an excited coherent superposition state $\frac{1}{\sqrt{2}}(|1\rangle + |2\rangle)$ with unequal rates of spontaneous relaxation, $\gamma_1 \gg \gamma_2$. If the system

does not decay within the time interval T (a zero result of measurements), then the system evolves to the following state:

$$(\exp(-2\gamma_1 T) + \exp(-2\gamma_2 T))^{-1/2}$$

$$\times (\exp(-\gamma_1 T)|1\rangle + \exp(-\gamma_2 T)|2\rangle).$$

It can be easily seen that the level $|2\rangle$, which is characterized by a longer lifetime, acquires a greater weight than the level $|1\rangle$ after a measurement with zero result. A similar effect is observed when a photon propagates through an optically dense condensate. The escape rate of atoms from the condensate is proportional to the laser pulse intensity and is generally a function of coordinates. The event of absorption of a photon can be interpreted as the measurement of an atomic coordinate. Thus, a measurement with zero result, when a photon passes through a condensate without absorption, changes the translation state of atoms in the condensate. In other words, it is more likely that one finds atoms in the right-hand part of the condensate, lying at a greater distance from the point where the laser pulse enters the medium.

Suppose that the natural frequency of the trap is much lower than the rate of optical excitation of atoms by laser radiation and than the inverse duration of the laser pulse. In this approximation, we can neglect the term involving $\hat{H}$ in equation (2). Let the transit time of a photon passing through a BEC be much less than the duration of the laser pulse. Then, we can also neglect the time derivative on the left-hand side of equation (1). The solution to equation (2) in this case is written as

$$\hat{\psi}(x, t) = \exp\left(-\frac{1}{2}\int_0^{\theta(t)} J(\theta')d\theta'\right)\hat{\psi}_0(x). \quad (4)$$

Here, we have introduced the dimensionless intensity $J = \frac{u}{u_0}$ and the dimensionless parameter $\theta = \frac{\sigma}{\hbar\omega}\int_{-\infty}^{t} u_0(t')dt'$, which characterizes the influence of the laser pulse on the BEC and depends on the laser pulse intensity and the interaction time; $\hat{\psi}_0(x)$ is the initial value of the atomic field operator.

Substituting expression (4) into equation (1), we derive the closed equation

$$\frac{\partial}{\partial\xi}J = -\exp\left(-\int_0^{\theta} J d\theta'\right)J \quad (5)$$

subject to the boundary condition $J|_{\xi=0} = 1$, where $\xi = n\sigma\int_0^x |\varphi_0(x')|^2 dx'$ is the dimensionless optical thickness and n is the initial concentration of the condensate. A solution to equation (5) can be written as

$$J = \frac{\exp(\theta - \xi)}{\exp(-\xi)(\exp(\theta) - 1) + 1}. \quad (6)$$

In the case of a weak laser pulse ($\theta \ll 1$), this solution describes exponential decay of the laser pulse intensity: $u = u_0\exp(-\xi)$ (the Bouguer–Lambert law). In the case of high-intensity radiation ($\theta \gg \max\{1, n\sigma L\}$), the condensate is being destroyed, after which the laser radiation propagates without losses.

Now, let us consider changes that occur in the condensate. The occupation numbers of states k, $n_k(t) = \langle \hat{b}_k^+(t)\hat{b}_k(t)\rangle$, are convenient parameters for this purpose. At the initial moment of time, we have $n = \sum_k n_k(0)$. Substituting (6) into (4), we arrive at

$$n_k(t) = n|\alpha_{k0}|^2, \quad (7)$$

where

$$\alpha_{k0} = \int_0^L \frac{\varphi_k^*(x)\varphi_0(x)}{\sqrt{\exp(-\xi(x))\exp(\theta) - 1 + 1}}. \quad (8)$$

In the case when the trap potential can be represented as a rectangular well with infinitely high walls at $x = 0, L$, the eigenfunctions of the Hamiltonian $\hat{H}$ can be written as

$$\varphi_k(x) = \sqrt{\frac{2}{L}}\sin\frac{\pi(k+1)x}{L} \quad (9)$$

and the corresponding eigenvalues within the interval $x \in [0, L]$ are given by

$$E_k = \frac{\hbar^2}{2M}\left(\frac{\pi}{L}\right)^2(k+1)^2, \quad (10)$$

where M is the atomic mass.

Let us represent the density of the atomic field operator of the condensate in the following form:

$$\langle \hat{\psi}^+(x)\hat{\psi}(x)\rangle\big|_t$$

$$= n\sum_{k,m=0}^{+\infty} \alpha_{k0}^*\alpha_{m0}\exp\left(\frac{i}{\hbar}(E_k - E_m)t\right)\varphi_k^*(x)\varphi_m(x). \quad (11)$$

The series (11) rapidly converges in k and m, since the integrand in (8) is a rapidly oscillating function. Therefore, to calculate the density of the atomic field operator, it is sufficient to perform summation in the series up to $k, m = 3$. For time intervals on the order of the pulse

duration, we neglect the variation of the phase factor $\exp\left(\frac{i}{\hbar}(E_k - E_m)t\right)$ and set this factor equal to unity for small k and m.

The figure shows evolution of the distribution density of the atomic field operator $\langle\hat{\psi}^+(x)\hat{\psi}(x)\rangle$ as function of the parameter characterizing the interaction of the condensate with a laser pulse within the range $1 \le \theta \le 5$ for the dimensionless optical thickness of the condensate equal to $\xi = 3$. As can be seen from this plot, the interaction of the laser pulse with an optically dense BEC shifts the maximum of the condensate density in the direction of radiation propagation, so that, effectively, the radiation "destroys" the condensate from the side where the laser pulse enters the medium. In the case of an optically thin BEC, the escape rate of atoms from the condensate is independent of the coordinate. Therefore, the density distribution of the atomic operator remains symmetric with respect to the center of the trap.

In conclusion, we should note that the absorption of light in an optically dense BEC not only optically excites ground-state atoms, but also changes the initial state for some part of atoms due to the above-described effect of measurement with zero result. Thus, even the component of a degenerate atomic ensemble that contributes to radiation absorption is eventually transformed to a state of collective excitation. The results obtained in this paper hold true on a qualitative level for a condensate of higher density, when we have to take into consideration the interaction between atoms, and for traps of other types.

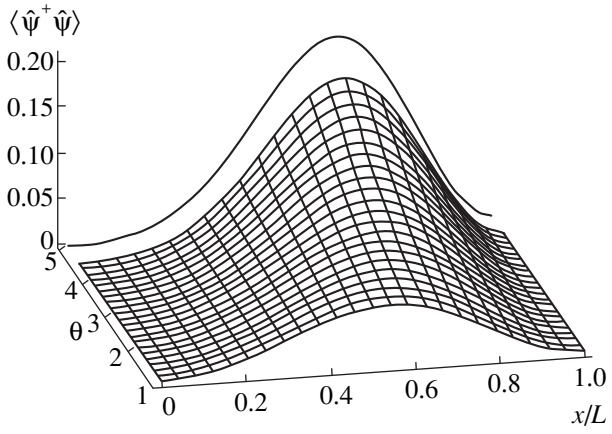

The distribution density of the atomic field operator $\langle\hat{\psi}^+(x)\hat{\psi}(x)\rangle$ as function of the parameter characterizing the interaction of the condensate with a laser pulse within the range $1 \le \theta \le 5$ for the dimensionless optical thickness of the condensate equal to $\xi = 3$.

This study was supported by the Russian Foundation for Basic Research, project no. 99-02-17076.

REFERENCES

1. M. H. Anderson, J. R. Ensher, M. R. Matthews, *et al.*, Science **269**, 198 (1995); C. C. Bradley, C. A. Sackett, J. J. Tollett, *et al.*, Phys. Rev. Lett. **75**, 1687 (1995).
2. K. B. Davis, M.-O. Mewes, M. R. Andrews, *et al.*, Phys. Rev. Lett. **75**, 3969 (1995).
3. J. Javanainen, Phys. Rev. Lett. **72**, 2375 (1994); J. Javanainen, Phys. Rev. Lett. **75**, 1927 (1995).
4. R. J. Cook, Prog. Opt. **28**, 363 (1990).

Translated by A. M. Zheltikov

Technical Physics Letters, Vol. 26, No. 3, 2000, pp. 250–253. Translated from Pis'ma v Zhurnal Tekhnicheskoĭ Fiziki, Vol. 26, No. 6, 2000, pp. 59–66.

Solid–Liquid Transition Described by the Particle Method

G.-P. Ostermeyer* and V. L. Popov**

** TU Berlin, Institut für Mechanik, Sekr. C8, Straße des 17 Juni 135, D-10623 Berlin, Germany*

*** Institute of Strength Physics and Materials Science, Siberian Division, Russian Academy of Sciences, Tomsk, Russia*

Received October 11, 1999

Abstract—In recent years, the method of mesoparticles has proved to offer an effective approach to discretization and modeling of the mechanical behavior in various systems. However, a principal disadvantage of these methods is the inability to describe systems possessing differential (in particular, small) transverse rigidity. This difficulty can be bypassed using many-particle potentials instead of the conventional pairwise functions. Proceeding from a two-particle interaction potential of the Lennard–Jones type, we derive an explicit form of the many-particle (temperature-dependent) potential capable of describing systems with arbitrarily small (up to zero) transverse rigidity, while retaining all other advantages of the particle method. A particular form of the many-particle dissipative function is proposed possessing the general symmetry properties. © *2000 MAIK "Nauka/Interperiodica".*

In the previous work [1], the need in methods providing joint consideration of the thermodynamic and mechanical properties of solids was justified. On approaching the melting temperature, the shear modulus of many solids markedly decreases and turns zero at the melting point. As a result, the solids loose their mechanical stability with respect to shear stresses. The ability to describe systems with significantly variable shear moduli, as well as the media possessing zero modulus, is therefore an important requirement posed on any approach to the description of elastic-plastic bodies, including theories based on the particle methods.

Below, we will consider a question as to how can a drop in the transverse rigidity near the melting point and the very transition from solid to liquid state be described within the framework of the method of mesoparticles. According to this method, a medium is divided into separate "mesoparticles" and the interaction potential between these particles is selected so as to satisfy the condition of retained macroscopic properties of the medium (elastic moduli, etc.). Evolution of this system under the action of applied forces is descried using the classical equations of motion, which makes this approach somewhat analogous to the method of molecular dynamics. At the same time, the joint description of the thermodynamic and mechanical properties of the medium implies that the interaction potential should depend on the temperature, which is therefore treated as a parameter characterizing individual particles.

An attempt to describe the interaction between thermodynamic and mechanical degrees of freedom was undertaken in [2] based on an interaction potential of the type

$$V = V_0\left[\left(\frac{r_0}{r}\right)^{12} - 2\sqrt{1-\left(\frac{T}{T_c}\right)^2}\left(\frac{r_0}{r}\right)^6\right], \qquad (1)$$

with the attracting part turning zero at a critical temperature T_c. In equation (1), the quantities V_0 and r_0 represent the potential well depth and the equilibrium distance between particles at $T = 0$.

Although the method developed in [2] is capable of describing the melting of a sample with free faces heated from beneath, as well as the extrusion process, this approach should be only considered as the first step toward the consistent joint thermomechanical description of mesoparticle systems. The need in further development of the mesoparticle method is related to the following circumstances.

1. The equilibrium distance between particles interacting according to the potential (1) tends to infinity by the law $r = r_0(1 - T/T_c)^{-1/2}$ when the temperature approaches the critical value. Thus, we deal with a transition from solid to gaseous state, rather than from solid to liquid.

2. On the other hand, a system of particles interacting by the law (1) would occur in a crystalline state even at temperatures above T_c, provided that a nonzero external pressure P is applied. The shear modulus is proportional to $P^{14/13}$, representing approximately a linear function of the pressure.

Both these properties are at variance with the known penomenological properties of the transition from solid to liquid state. As can be readily demonstrated, these

difficulties cannot be principally bypassed within the framework of a model based on the two-particle interaction potentials.

Below we propose a new formulation of the method of mesoparticles that allows the above difficulties to be avoided. The consideration begins with description of the liquid state, since major difficulties arise when the method of mesoparticles is applied to liquids.

Many-particle interaction potential. Let us proceed from the main phenomenological property of liquids, whereby their potential energy depends only on the density of medium. Any motions not affecting the density do not change the potential energy of this system and, hence, do not give rise to returning forces. This property is just what is associated with "fluidity" of a liquid medium.

At the same time, the elastic properties of a liquid with respect to hydrostatic compression and extension are the same as in solids. This circumstance is what essentially differs liquids from gases. Thus, we have to select a potential of interaction so as to provide an elastic compression modulus of the same order as in solids, while admitting a zero modulus of shear.

We proceed from a system of particles in the solid state, described by a two-particle potential of the Lennard–Jones type:

$$V = V_0\left[\left(\frac{r_0}{r}\right)^{12} - 2\left(\frac{r_0}{r}\right)^{6}\right]. \quad (2)$$

Let us represent the potential energy of this system in the equilibrium state as a function of the number density of particles n. Taking into account that the density of a two- (2D) and three-dimensional (3D) system is inversely proportional to the squared and cubic interparticle distance (provided that changes in the particle spacing do not alter the character of the system packing), $n \propto r^{-2}$ and $n \propto r^{-3}$, respectively, we obtain

$$V = AV_0\left[\left(\frac{n}{n_0}\right)^{6} - 2\left(\frac{n}{n_0}\right)^{3}\right], \quad D = 2, \quad (3)$$

$$V = AV_0\left[\left(\frac{n}{n_0}\right)^{4} - 2\left(\frac{n}{n_0}\right)^{2}\right], \quad D = 3, \quad (4)$$

where A is a constant factor independent of the density. The value of A can be determined by summing potential (2) over all particles in the system and comparing the result with equations (3) and (4). Since the potential (2) rapidly decreases with the distance, we may restrict the consideration to the nearest neighbors (neglect of the more distant particles leads to a n error of the order of 1.5%). In this approximation,

$$A = \frac{1}{2}NZ, \quad (5)$$

where N is the total number of atoms in the system and Z is the coordination number of close packing ($Z = 6$ and 12 for 2D and 3D systems, respectively). For brevity, we will consider below only the 2D case (the 3D systems are described similarly).

In 2D systems, the potential energy per atom is

$$V^* = \frac{Z}{2}V_0\left[\left(\frac{n}{n_0}\right)^{6} - 2\left(\frac{n}{n_0}\right)^{3}\right], \quad D = 2. \quad (6)$$

A decisive step in constructing the required interaction potential consists in treating equation (6) as the definition of the potential energy in the system studied. For an inhomogeneous system, the total potential energy is determined by summing the values (6) over all particles:

$$V = \sum_i V^*(n^{(i)}), \quad (7)$$

where the quantities $V^*(n^{(i)})$ are given by equation (6) with $Z = 6$ and $n^{(i)}$ is an appropriate "density" of particles at the point $r^{(i)}$ corresponding to coordinates of the ith particle.

Apparently, a system of particles described by equation (7), subjected to homogeneous compression or extension, would exhibit the same elastic properties as a solid with the potential energy described by formula (3). At the same time, the motions of particles not changing their local densities would not affect the potential energy. Thus, both principal phenomenological properties of the liquid state formulated above are adequately reflected within the framework of the method of particles with the new interaction potential proposed.

Let us determine the local density of medium at the point $r^{(i)}$ with the aid of a weight function K significantly decreasing at a distance $R_0 > r_0$ (in fact, even $R_0 \approx 2r_0$ is sufficient for practical calculations):

$$n^{(i)} \equiv n(r^{(i)}) \equiv \sum_{j \neq i} K(|r^{(i)} - r^{(j)}|). \quad (8)$$

The weight function K has to be normalized so as to provide that equation (8) would give the equilibrium density n_0 for an equilibrium configuration of the system with potential (2).

Note that use of the weight function is equivalent to smoothening of the liquid structure over distances of the order of a few interatomic spacings, which makes the proposed approach similar to the method of smooth particles developed by Lucy [3] and Monogham [4]. Some applications of the smooth particle method to hydrodynamic problems can be found, for example, in [5]. However, the smooth particle method as such is inapplicable to media with variable transverse rigidity, and the more so, to description of the transition from solid to liquid state, which is the main purpose of our work and the major advantage of the particle method proposed.

A force acting upon the ith atom from the surrounding atoms is described by the equation

$$F^{(i)} = -\frac{\partial V}{\partial r^{(i)}}$$
$$= -\sum_{j\neq i}\left(\frac{\partial V^*(n^{(i)})}{\partial n^{(i)}} + \frac{\partial V^*(n^{(j)})}{\partial n^{(j)}}\right)\frac{\partial K}{\partial r}\bigg|_{r=|r^{(i)}-r^{(j)}|}\frac{r^{(i)}-r^{(j)}}{|r^{(i)}-r^{(j)}|}. \quad (9)$$

It should be recalled that the many-particle potential (7) was introduced so as to ensure that the elastic properties of the liquid subjected to homogeneous compression or extension would be the same as those of the corresponding solid. The only difference between the system with many-particle potential (7) and the system with two-particle potential (2) is related to behavior of the transverse rigidity: the former potential refers to a liquid, while the latter describes a solid. Thus, by introducing a mixed potential,

$$V_{\text{tot}} = \alpha V_{\text{two}} + \beta V_{\text{many}} \quad (\alpha + \beta = 1) \quad (10)$$

we may describe systems in which the transverse rigidity varies (up to a zero shear modulus in the liquid state, which corresponds to $\alpha = 0$).

If the melting in our system were a second-order phase transition (this is only possible at separate points of the equilibrium P–V diagram [6]), the shear modulus μ would tend to zero by the law $\mu \propto (T - T_c)$ [1]. Accordingly, the interaction potential (10) in the vicinity of the melting temperature could be presented in the following for:

$$V_{\text{tot}} = (T/T_c - 1)V + (T/T_c)V^*. \quad (11)$$

In real systems featuring the first-order transitions, the coefficients α and β will be functions of the temperature exhibiting a jumplike change to 0 and 1, respectively, at the melting point. As for a system with inhomogeneous temperature distribution, an obvious generalization of equation (11) to this case is provided by the relationship

$$V_{\text{tot}} = \sum_i\left[(T^{(i)}/T_c - 1)\sum_{j\neq i}V(r_{ij}) + (T^{(i)}/T_c)V^*(r^{(i)})\right]. \quad (12)$$

Energy dissipation. A principal difference between the method of molecular dynamics and the method of mesoparticles is that the latter particles possess individual thermodynamic properties such as temperature. This poses an important problem concerning the pathways of energy dissipation in a system of quasiparticles. An approach to description of the energy dissipation within the framework of the particle method was considered in [2] in application to systems with a single degree of freedom. In a many-particle system, however, the dissipation of energy cannot be considered separately for each pair of particles, since the process depends, in the general case, on the correlated motion of many neighboring particles. The general conditions, to which any dissipative function must obey, can be formulated based on the symmetry considerations. In particular, the dissipative function must turn zero for any motion of the system as a whole. At the same time, the dissipation must tend to zero with vanishing interaction between particles, even if the latter perform relative motions. Both these conditions can be satisfied with a dissipative function representing a product of the potential (corresponding to a given frequency) and a function of the appropriate "deformation rate tensor" at the given point. The latter term would automatically turn zero for any translational and rotational motion of the system as a whole.

In order to derive an expression for the dissipative function, let us consider a system of moving particles with the configuration determined by a set of coordinates $[r^{(i)}]$ at a time instant t, and by a set $[r'^{(i)} = r^{(i)} + u^{(i)}]$ at $t' = t + \Delta t$. An optimum local approximation of this motion in the vicinity of the ith particle can be provided by the motion equivalent to a homogeneous deformation of the system. For a homogeneous deformation characterized by the tensor ε_{km}, the displacements of particles are described as

$$(\tilde{u}^{(j)} - \tilde{u}^{(i)})_k = \varepsilon_{km}(r^{(j)} - r^{(i)})_m. \quad (13)$$

The actual displacements differ from those given by (13) by the values

$$[(u^{(j)} - u^{(j)})_k - (\tilde{u}^{(j)} - \tilde{u}^{(j)})_k]$$
$$= [(u^{(j)} - u^{(j)})_k - \varepsilon_{km}(r^{(j)} - r^{(i)})_m].$$

Let us determine tensor ε_{km} so as to minimize the sum of square deviations with the weight function $\Phi(r)$:

$$\Delta = \sum_{j\neq i}\sum_{k,m}\Phi(|r^{(i)} - r^{(j)}|) \times [(u^{(j)} - u^{(j)})_k - \varepsilon_{km}(r^{(j)} - r^{(i)})_m]^2. \quad (14)$$

The condition of minimum is as follows:

$$\frac{\partial\Delta}{\partial\varepsilon_{km}} = \sum_{j\neq i}\Phi(|r^{(i)} - r^{(j)}|) \times [(u^{(j)} - u^{(j)})_k - \varepsilon_{km}(r^{(j)} - r^{(i)})_m](r^{(j)} - r^{(i)})_m = 0 \quad (15)$$

and yields

$$\varepsilon_{km}^{(i)} = \frac{\sum_{j\neq i}\Phi(|r^{(i)} - r^{(j)}|)(u^{(j)} - u^{(j)})_k(r^{(j)} - r^{(i)})_m}{\sum_{j\neq i}\Phi(|r^{(i)} - r^{(j)}|)(r^{(j)} - r^{(i)})_m^2}. \quad (16)$$

Finally, the dissipative function for the ith particle, which describes the rate of the energy conversion from

mechanical to thermal, can be determined (taking into account the above methodological considerations) as

$$D^{(i)} = V^{(i)}\left\{\eta\left(\dot{\varepsilon}_{mn} - \frac{1}{3}\delta_{mn}\dot{\varepsilon}_{ll}\right)^2 + \frac{\zeta}{2}\dot{\varepsilon}_{ll}^2\right\}, \quad (17)$$

where δ_{mn} is the Kronecker delta symbol and η, ζ are phenomenological (positive) coefficients related to the viscosity of medium (although not having the corresponding dimensionality). The term in braces is the most general form of a quadratic scalar function of the symmetric second-rank tensor for an isotropic medium [7].

The total dissipative function of the medium has the following form:

$$D = \sum_i D^{(i)}. \quad (18)$$

The equations of motion can be written as

$$\frac{d}{dt}\left(\frac{\partial L}{\partial \dot{r}^{(i)}}\right) - \frac{\partial L}{\partial r^{(i)}} + \frac{\partial D}{\partial \dot{r}^{(i)}} = 0, \quad (19)$$

$$\frac{d}{dt}T^{(i)} = \frac{1}{c^{(i)}}\dot{r}^{(i)}\frac{\partial D}{\partial \dot{r}^{(i)}}$$
$$\Rightarrow \frac{d}{dt}\left(\dot{r}^{(i)}\frac{\partial L}{\partial \dot{r}^{(i)}} - L + c^{(i)}T^{(i)}\right) = 0, \quad (20)$$

where $c^{(i)}$ is the heat capacity of the ith particle, $L = K - V_{\text{tot}}$ is the Lagrange function of the system, $K = \sum_i \frac{m^{(i)}\dot{r}^{(i)2}}{2}$ is the kinetic energy, and V_{tot} is the potential energy determined by equation (12). Temperature variations related to the thermal conductivity can be considered using an approach analogous to that employed in [2].

Thus, we have arrived at a closed system of mechanical and thermodynamic equations describing the mechanical behavior of both solid and liquid media and their mutual transformations. Examples of the application of the proposed method to the description of various processes such as melting, plastic deformation and fracture, extrusion, sintering, friction and wear, etc., will be given in a separate publication.

The authors are grateful to Deutsche Forschungsgemeinschaft, SFB 605, for financial support.

REFERENCES

1. V. L. Popov, Pis'ma Zh. Tekh. Fiz. (1999).
2. G.-P. Ostermeyer, ZAMM (1999) (in press).
3. L. B. Lucy, Astron. J. **82**, 1013 (1977).
4. J. J. Monoghan, Ann. Rev. Astron. Astrophys. **30**, 543 (1992).
5. O. Kum, W. G. Hoover, and H. Posch, Phys. Rev. E **52**, 4899 (1995).
6. L. D. Landau and E. M. Lifshits, *Statistical Physics* (Nauka, Moscow, 1976), Vol. 1.
7. L. D. Landau and E. M. Lifshits, *Theory of Elasticity* (Nauka, Moscow, 1987).

Translated by P. Pozdeev

Technical Physics Letters, Vol. 26, No. 3, 2000, pp. 254–258. Translated from Pis'ma v Zhurnal Tekhnicheskoĭ Fiziki, Vol. 26, No. 6, 2000, pp. 67–77.

Crack Propagation: Dynamic Stochasticity and Scaling

O. B. Naĭmark, V. A. Barannikov, M. M. Davydova, O. A. Plekhov, and S. V. Uvarov

Institute of Mechanics of Continua, Ural Division, Russian Academy of Sciences, Perm, Russia

Received October 7, 1999

Abstract—The results of theoretical and experimental investigations provide explanation of the mechanism of stochastic branching during crack propagation in a solid, relating this phenomenon to changes in the fundamental symmetry relationships in a nonlinear system representing the solid with defects. The character of the stochastic behavior of quasibrittle materials is determined by nonlinear dynamics of the ensemble of microscopic defects under the conditions of kinetic transitions. The transition from dispersed to macroscopic fracture is accompanied by the appearance of multiple fracture zones in the regime of explosion-like instability development over a discrete spectrum of spatial scales. *© 2000 MAIK "Nauka/Interperiodica".*

INTRODUCTION

In recent years, a number of new experimental data were reported on the dynamics of cracking. These results showed qualitative discrepancies with the classical mechanics of crack propagation.

(i) The limiting crack propagation velocity in brittle materials (glass, PMMA) amounts to only 0.6 of the Rayleigh wave velocity V_R considered as limiting value in the classical fracture mechanics.

(ii) A sharp transition from longitudinal propagation to branching is observed at a crack velocity of $0.4V_R$ [1].

(iii) Crack propagation in a supercritical regime is accompanied by pronounced acoustic emission [2].

(iv) Fracture surfaces exhibit a structure correlated to oscillations in the crack velocity [3–5].

Fractographic analysis of the cleavage surfaces showed that an adequate explanation of the observed scenarios of fracture development can be based on description of the physical mechanisms governing the dynamics of cracking. Previously [6], we proposed a model explaining the existence of a limiting crack propagation velocity and the transition to branching by interaction of the crack with an ensemble of microcracks formed in the region of the crack tip.

In this work, we have experimentally studied the dynamics of crack propagation in PMMA samples using a high-speed video camera. The results of these experiments showed evidence of a threshold character of the transition from longitudinal crack propagation to branching (upon reaching the critical velocity) and confirmed the determining role of nonlinear kinetics in the accumulation of microcracks in the zone adjacent to the crack tip. Combination of the methods of photoelasticity and high-speed video registration allowed us to establish a wave character of the stress field during propagation of a crack, showed a pronounced deviation from radial symmetry in the distribution of stress waves (Doppler effect), and revealed correlation between the qualitative patterns of the fracture surface relief and the regimes of nonlinear cracking dynamics.

STOCHASTIC MODEL AND DETERMINING EQUATIONS

Taking into account a decisive role of mesoscopic defects (microcracks, microshifts) in the fracture development, these defects can be represented [7] as localization of the corresponding symmetry group of the tensor of distortion. According to this, a symmetric tensor $s_{ik} = sv_iv_k$ describes the volume s and orientation $\mathbf{v}$ of a normal tear-off crack. The energy of a unit defect, modeled by a dislocation pileup, can be written as

$$E = E_0 - H_{ik}s_{ik} + \alpha s_{ik}^2. \quad (1)$$

In equation (1), the term $H_{ik}s_{ik}$ describes the work against the "effective" field $H_{ik} = \gamma\sigma_{ik} + \lambda p_{ik}$ (representing a sum of applied stresses σ_{ik} and the "mean" field $\lambda n\langle s_{ik}\rangle$) isolated by defects, while the quadratic term αs_{ik}^2 reflects a local increase in energy in the vicinity of the defect (related to its growth); parameters γ, λ, and α characterize the material and n describe the concentration of microcracks.

The macroscopic tensor p_{ik} of the density of microdefects is determined by averaging

$$p_{ik} = n\int s_{ik}W(s, \mathbf{v}, \mathbf{l})ds d^2\mathbf{v} d^3\mathbf{l} \quad (2)$$

with a distribution function obtained [9] upon solving the Fokker–Planck equation with an assumption of the statistical automodel (self-similar) character of the defect distribution [8]. Figure 1 shows the plots of p_{zz} versus σ_{zz} for the case of uniaxial tension at various vales of the parameter $\delta = 2\alpha/\lambda n$. Solution (2) indicates that a solid may exhibit three qualitatively different

reactions to the growth of defects, which correspond to the passage over certain critical values δ_* and δ_c representing the points of bifurcation. These values separate the monotonic ($\delta > \delta_*$), metastable ($\delta_c < \delta < \delta_*$), and unstable ($\delta < \delta_c$) behavior. An analysis of these reactions [9] showed that quasibrittle fracture corresponds to the region of $\delta < \delta_c$, where the transition through a threshold level p_c results in the explosion-like growth of defects.

The free energy F, reflecting the spectrum of reactions of the solid in response to the crack formation (Fig. 1), can be presented in the following for [9]:

$$F = \frac{1}{2}A(\delta)p_{ik}^2 + \frac{1}{4}Bp_{ik}^3 + \frac{1}{6}C(\delta)p_{ik}^4 + D\sigma_{ik}p_{ik} - \frac{1}{2}\chi(\nabla p_{ik})^2, \quad (3)$$

where A, B, C, and D are the coefficients of expansion. Here, the gradient term allows for the nonlocal effects in the so-called longwave approximation (χ is the nonlocal parameter). Coefficients at the square and high-order terms of expansion (3) depend on δ, which accounts for the change of asymptotic behavior upon transition through the bifurcation points δ_* and δ_c.

According to the Ginzburg–Landau approach [10], the kinetics of accumulation of the defects is determined by the rate of free energy decrease with increasing density of defects $\frac{\delta F}{\delta t} = \frac{\delta F}{\delta p_{ik}}\dot{p}_{ik} \le 0$ ($\frac{\delta}{\delta p_{ik}}$ is the variational derivative). Using this approach, a kinetic equation for the p_{ik} tensor can be written as

$$\frac{dp_{ik}}{dt} = -\Gamma\frac{\partial F}{\partial p_{ik}} + \frac{\partial}{\partial x_1}\left(\zeta\frac{\partial p_{ik}}{\partial x_1}\right), \quad (4)$$

where Γ is the kinetic coefficient and $\zeta = \Gamma\chi$. The deformation tensor is determined by the well-known relationship $\varepsilon_{ik} = -\frac{\partial\Phi}{\partial\sigma_{ik}}$ ($\Phi = F - \sigma_{ik}\varepsilon_{ik}$), which yields

$$\varepsilon_{ik} = \frac{1}{2\mu}\sigma'_{ik} + \frac{1}{9k}\sigma_{11}\delta_{ik} + Dp_{ik}, \quad (5)$$

where μ and k are the shear and bulk moduli, respectively, and σ'_{ik} and σ_{11} are the off-diagonal and shear components of the stress tensor, respectively. Equations (4) and (5) serve as determining relationships for a solid with microcracks.

Special features of the behavior of a nonlinear system with $\delta \le \delta_c$ upon the transition through the instability threshold p_c were studied previously [6]. It was established that the final stage of fracture development

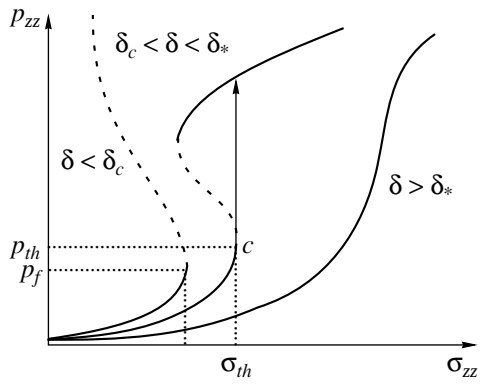

Fig. 1. Schematic diagram illustrating nonlinear response of a solid to the crack formation.

(Fig. 1) is described by an automodel solution of the type

$$\hat{p} = g(t)f(\xi), \quad \xi = \frac{x}{\phi(t)}, \quad (6)$$

which exhibits a singularity in the time variation $g(t) = G(1 - t/t_c)^{-m}$. In this expression, the function $g(t)$ governs the increase in the density of defects in the spectrum of spatial scales ξ_i (the spectrum of eigenvalues of the nonlinear problem); the quantity φ determines variation of the halfwidth of the delocalization region; $G > 0$ and $m > 0$ are the effective parameters of the material in the vicinity of the critical point p_c.

THE AUTOMODEL CHARACTER OF FRACTURE. DYNAMIC CLEAVAGE BRANCH

The spectrum of intrinsic forms (6) determines a new set of independent coordinates for the nonlinear system of equations (4) and (5) in a developed stage of the fracture process, at which the fracture is localized and the foci of macroscopic cracks are formed. The fact that the nonlinear dynamics of the system is described by new coordinates implies a sharp change in the symmetry and topology of the system. The existence of a spectrum of localization scales (which is essentially the energy spectrum) suggests the possibility of resonance excitation of the corresponding nonlinear automodel modes and regimes. This conclusion was experimentally confirmed [11] by the effect of "dynamic branch" observed during cleavage. According to this, the cleavage sections, obtained for various tensile stress amplitudes, exhibited pronounced local fracture foci having the form of mirror-symmetric zones featuring different spatial scale of localization. The resonance excitation of these fracture structures, observed for the corresponding impact pulse amplitudes ($\sigma_A = 1.5 \times 10^7$ Pa for PMMA) and durations (~10^{-6} s), accounts for a weak dependence of the time of fracture on the stress wave amplitude.

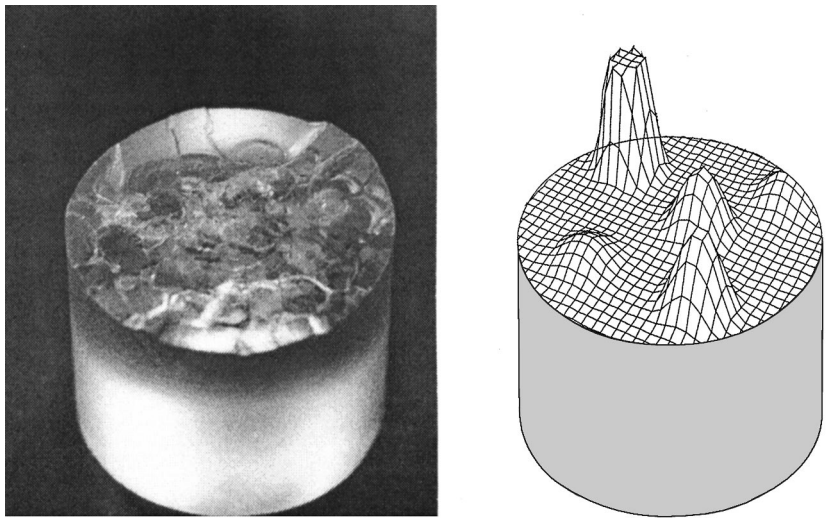

(a) (b)

Fig. 2. (a) Micrograph of a typical cleavage zone; (b) a numerically modeled distribution of the density of microcracks in a fracture cross-section.

Figure 2a shows micrograph of a typical fracture surface showing numerous mirror-symmetric zones; Fig. 2b presents the results of numerical modeling of the distribution of microcrack density in a cross-section belonging to the "dynamic branch" region. Note that characteristic localized maxima in the defect density distribution with "sharpening kinetics" correspond to the experimentally observed mirror zones having close dimensions for the given stress amplitude in the fracture cross-section.

MECHANISM OF INSTABILITY DEVELOPMENT DURING CRACK PROPAGATION

The concept of spatial–temporal pattern developed above for the kinetics of accumulation of microcracks can be used to explain the special features of the process of crack propagation. The dynamics of interactions between a propagating crack and the ensemble of microdefects formed at the crack tip includes two stages. The first stage features the formation of a region of localized dispersed fracture. As a result a new macroscopic defect structure appears in which dimensions of the stress field fluctuations markedly exceed the size of a single microdefect. The second stage corresponds to the explosion-like growth in the density of microcracks localized on the L_T spatial scale. The time to fracture τ_c consists of two parts: t_u, the time required for the formation of a nearly automodel spatial distribution of defects, and t_c, called the sharpening time [9]. The L_T and t_c values determine a critical velocity of the longitudinal crack propagation $V_c \approx \dfrac{L_T}{t_c}$.

Let us consider in more detail the two characteristic regimes of crack propagation: longitudinal growth ($V < V_c$) and branching ($V > V_c$). The longitudinal growth corresponds to the case when t_u accounts for the most part of τ_c, whereby the crack propagation velocity does not exceed the critical value V_c. In this case, a region is formed on the L_T scale at the crack tip in which the stress level exceeds the critical value ($\sigma > \sigma_c$). Under these conditions, new cracks are nucleated during the time $\tau_c = \dfrac{L_T}{V} \geq t_c$ along the line of the initial macrocrack orientation. If the external load reaches a level sufficient to provide for the condition $V \sim V_c$, the fracture surface exhibits a characteristic cellular structure (Fig. 3a). Figure 3b presents the results of numerical modeling of the microcrack density evolution in the zone situated in front of the crack tip (C–C' line).

Statistical inhomogeneity of the properties of a material leads to sharpening of the defect structures both in the vicinity of the primary crack and at a certain distance from the crack edge, for $V > V_c$, the automodel profiles of defect distribution can form over a certain spectrum of trajectories characterized by an opening angle θ determined by the stress level σ_c inducing the automodel regime. Taking into account the asymptotic law of stress distribution at the crack tip, $\sigma_{ij} \approx K_I r^{-1/2} f_{ij}(\theta)$ (where K_I is the stress intensity coefficient and r, θ are the polar coordinates in the vicinity of the crack tip), we may determine the branching angle φ. This value indicates the interval in which critical stresses forming an automodel profile on the L_T scale are developed for the given external conditions (K_I value). Further increase in the crack propagation velocity leads to increasing extent of branching, that is, to the expansion of a zone featuring multiple nucleation of the localized automodel fracture defect structures.

EXPERIMENTAL INVESTIGATION OF CRACK PROPAGATION

Our experiments were performed on the samples of PMMA (Young's modulus E = 6.0 GN/m^2; Poisson's coefficient ν = 0.33; density ρ = 1.18 g/cm^3) with a length of L = 141 mm, a height of 66 or 86 mm, and a thickness varied from 0.6 to 1.9 mm. The Rayleigh wave velocity for PMMA is V_R = 1400 m/s). The experimental setup was capable of developing stresses ranging from 13 to 45 MPa. The experimental conditions were described by the applied force, and the sample was characterized by the average crack propagation velocity and the stress field distribution. The fracture surfaces were examined in an optical microscope. The cracking was initiated by a notch made at the middle of the sample side edge with a sharp knife. The stress field distribution was studied by method of photoelasticity. The crack propagation was registered using a high-speed digital video camera Remix REM 100-8. These experiments were conducted at the LAMEF laboratory (ENSAM, Bordeaux, France). The camera was capable of making a series of eight shots with resolution of 740×574 dots. The minimum exposure time of each shot was 5 ns and the time interval between sequential shots was 5–10 μs.

The velocity of crack propagation was determined by two methods. According to the first technique, the average crack velocity was determined by using the crack length (measured in each shot) and the time interval between shots. The second technique is based on the Doppler effect. We have measured the characteristics of advancing (ν_1, λ_1) and retarded (ν_2, λ_2) acoustic waves induced by the propagating crack. The crack velocity was calculated using a difference of the wavelengths $\lambda_2 - \lambda_1$ (or frequencies $\nu_1 - \nu_2$):

$$V = \frac{\lambda_2 - \lambda_1}{\lambda_2 + \lambda_1} V_R = \frac{\nu_1 - \nu_2}{\nu_1 + \nu_2} V_R, \qquad (7)$$

where ν_i are the wave frequencies, λ are the wavelengths, and V_R is the Rayleigh velocity. The V_R value

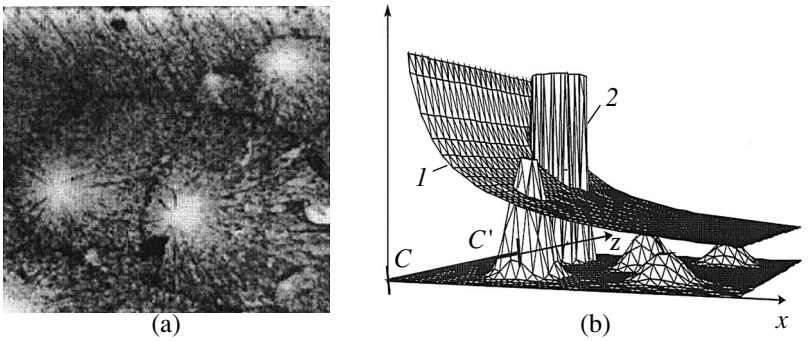

Fig. 3. (a) Micrograph of a typical cellular fracture surface corresponding to the beginning of transition to the branching regime of crack propagation; (b) numerically modeled distribution of (*1*) stresses and (*2*) defect density in the vicinity of the crack tip (line *C*–*C*').

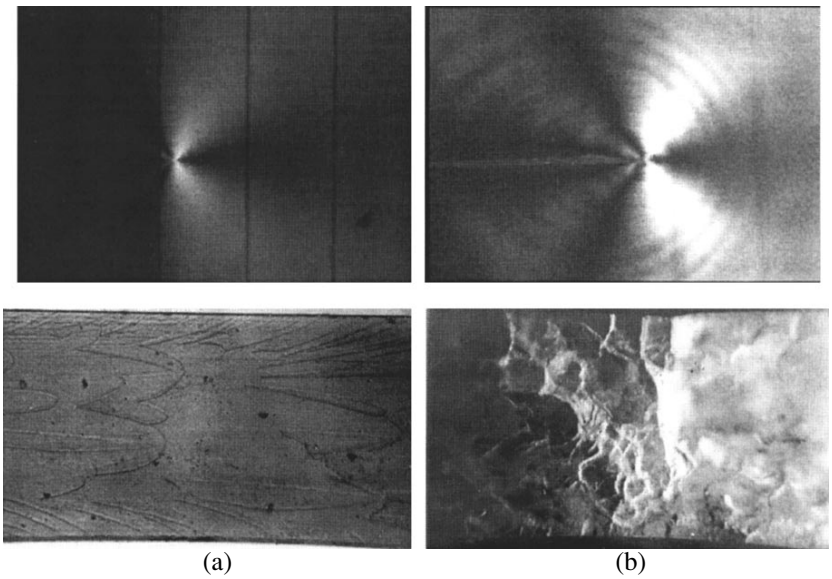

Fig. 4. Micrographs showing the patterns of stress distribution and fracture surface morphology.

was determined by measuring the velocity of propagation of a single wave front produced by interaction of the crack with an obstacle (a round hole). It was found that the crack generated stress waves traveling at a velocity of 1400 ± 100 m/s, which is very close to the Rayleigh velocity V_R^* [23]. The results the crack velocity determination by the two methods showed good agreement, the difference not exceeding 7–8%.

EXPERIMENTAL RESULTS

It was established that the crack can propagate in two regimes: uniform-longitudinal and branching (Fig. 4). In the former case, the crack propagated at a velocity of up to 416 m/s ($0.3V_R$) and formed a smooth fracture surface (Fig. 4a). In the branching mode, the crack velocity reached 500–800 m/s ($0.36–0.6V_R$) and the fracture surface exhibited considerable roughness (Fig. 4b). The fracture surface corresponding to a fast crack comprised numerous mirror-symmetric zones (Fig. 4b), which appeared at the sites of daughter microcrack nucleation at the primary crack tip. The arrangement, number, and character of development of these fracture zones depend on the crack propagation velocity. If the primary crack velocity is low, the mirror zones form only in the direction of maximum tensile stresses (coinciding with the initial crack orientation), which accounts for the generally smooth fracture surface. At a high crack propagation velocity, the zones acquire different orientations leading to a rough fracture surface. The degree of roughness increases with the crack propagation velocity. At a crack velocity exceeding 650 m/s, the fracture surface shows evidence of a partial fragmentation of the sample.

CONCLUSION

The transition from dispersed to macroscopic fracture is accompanied by the appearance of multiple localized fracture zones developed in the regime of explosion-like instability over a discrete spectrum of spatial scales.

The stochastic nature of the behavior of quasibrittle materials is related to nonlinear dynamics of the ensemble of microdefects under the conditions of kinetic transitions. The experimentally observed change in the regime of crack propagation (from uniform-longitudinal to branching) reflect the process of nucleation of multiple daughter cracks on the trajectories with orientations different from the primary crack direction.

The authors are grateful to Prof. J.L. Latayade (LAMEF–ENSAM), France) for kindly providing the opportunity of using the unique experimental equipment and for fruitful discussions. The work was supported by the Russian Foundation for Basic Research, project no. 96-01-00471.

REFERENCES

1. K. Ravi-Chandar and W.G. Knauss, Int. J. Fract. **26**, 65 (1984).
2. J. F. Boudet, S. Ciliberto, and V. Steinberg, J. Phys. II (Paris) **6**, 1493 (1996).
3. E. Bouchaud, J.-P. Bouchaud, J. Planes, *et al.*, Fractals **1** (4), 1051 (1993).
4. J. Planes, E. Bouchaud, and G. Lapasset, Fractals **1**, 1057 (1993).
5. E. Sharon, S. P. Gross, and J. Fineberg, Phys. Rev. Lett. **74**, 5096 (1995).
6. O. B. Naĭmark, M. M. Davydova, and O. A. Plekhov, in *Proceedings of the NATO Workshop "Probamat-21 Century," Kluver, 1998*, p. 127–142.
7. O. B. Naĭmark, *On the Deformation Properties and Fracture Kinetics of Solids with Microcracks. A Preprint* (Ural Division of the Russian Academy of Sciences, Sverdlovsk, 1982).
8. G. I. Barenblat and L. R. Botvina, Probl. Prochn., No. 12, 17 (1985).
9. O. B. Naĭmark, in *Proceedings of the IUTAM Symposium on Nonlinear Analysis of Fracture*, Ed. by J. R. Willis (Kluver, 1996), p. 285–298.
10. L. D. Landau and E. M. Lifshits, *Statistical Physics* (Nauka, Moscow, 1976), Part 5.
11. E. P. Evseenko, E. O. Zil'berbrandt, N. A. Zlatin, *et al.*, Pis'ma Zh. Tekh. Fiz. **3**, 684 (1977).

Translated by P. Pozdeev

Technical Physics Letters, Vol. 26, No. 3, 2000, pp. 259–261. Translated from Pis'ma v Zhurnal Tekhnicheskoĭ Fiziki, Vol. 26, No. 6, 2000, pp. 78–83.

Treatment of Inhomogeneous Radiation Broadening in Quantum Dot Heterostructures Described within the Framework of the Superradiation Model

N. Yu. Gordeev, S. V. Zaĭtsev, V. I. Kopchatov, L. Ya. Karachinskiĭ, I. I. Novikov, V. M. Ustinov, and P. S. Kop'ev

Ioffe Physicotechnical Institute, Russian Academy of Sciences, St. Petersburg, 194021 Russia
Applied Optoelectronics Inc., Kingfisher Dr. Sugar Land, TX 77478

Received November 10, 1999

Abstract—Based on the simplest expressions of the theory of superradiation for a two-level system, a model is suggested to describe inhomogeneously broadened spectra of radiation from heterostructures with quantum dot. A 98% agreement between predicted and experimental spectra is demonstrated in the entire wavelength range for an InGaAs/AlGaAs/GaAs heterostructure with quantum dots. Estimates of inhomogeneous broadening and characteristic time of superradiation are given. *© 2000 MAIK "Nauka/Interperiodica".*

The need in simulating the radiation spectra of semiconductor electronics devices (lasers, light emitting diodes) raises the problem of analyzing the form factors of homogeneous and inhomogeneous broadening. Previously we have demonstrated [1, 2] that one can use the simplest formulas of the theory of superradiation for a two-level system to derive an analytical expression for the form factor of homogeneous broadening of the radiation spectrum of laser semiconductor heterostructures,

$$F(\omega - \omega_0) \propto 2\pi\tau_N \operatorname{sech}(\pi\tau_N(\omega - \omega_0)), \qquad (1)$$

where τ_N is the characteristic time of superradiation, and $\omega - \omega_0$ is the frequency detuning.

The radiation spectrum of a quantum well at a low temperature (77 K), when inhomogeneous broadening may be ignored relative to the homogeneous one, is described with a high accuracy by the expression

$$R(E) = A\operatorname{sech}\left(\pi\tau_N\frac{E - E_0}{\hbar}\right), \qquad (2)$$

obtained as a convolution of the form factor of homogeneous broadening (1) and inhomogeneously broadened spectrum R_0 (in this case, $R_0(E) = \delta(E_0)$).

From the standpoint of theory, the radiation spectra of heterostructures with the active region of quantum dots (QDs). The "ideal" QD must have a discrete energy spectrum of the density of states (like an atomic one), which is in fact the δ-function [3]. In actual practice, however, the QDs making up the active region are inhomogeneous in size, composition, and shape [4]. All this results in a considerable inhomogeneous broadening of the radiation spectra, including the low-temperature ones.

It follows from the above considerations that, in simulating the radiation spectra of heterostructures with QDs, one must introduce the form factor of inhomogeneous broadening other than the δ-function. We will write inhomogeneous broadening in the simplest form (a rectangle of unit height and width equal to the characteristic energy of inhomogeneous broadening ΔE),

$$R_0(E) = \Theta\left(E - \left(E_0 - \frac{1}{2}\Delta E\right)\right)\Theta\left(\left(E_0 + \frac{1}{2}\Delta E\right) - E\right), \qquad (3)$$

where E_0 is the energy of transition.

This approximation allows the radiation spectrum to be described by the analytical expression

$$R(E) = B\left[\arctan\left(\sinh\left(\frac{\pi\tau_N\left(E_0 - \frac{1}{2}\Delta E - E\right)}{\hbar}\right)\right) + \arctan\left(\sinh\left(\frac{\pi\tau_N\left(E - E_0 - \frac{1}{2}\Delta E\right)}{\hbar}\right)\right)\right]. \qquad (4)$$

We have investigated samples of an AlGaAs/GaAs laser heterostructure grown by the molecular-beam epitaxy (MBE) method, in which the active region is provided by an array of ten layers of vertically bound InGaAs quantum dots. The MBE growth technology and the properties of the QDs are described in more detail in [5].

The samples were investigated under conditions of pulsed excitation (pulse duration, 3 μs; repetition frequency, 5 kHz) at a temperature of 77 K; for this pur-

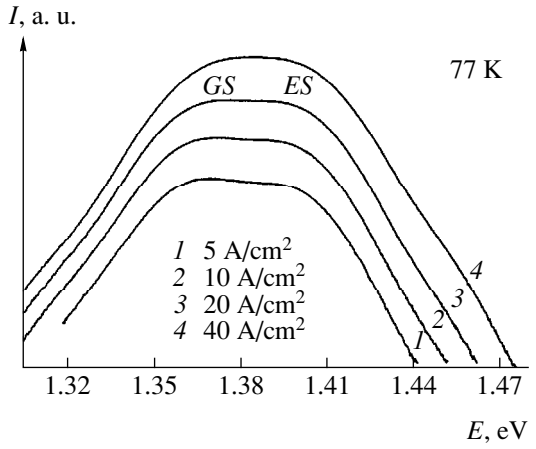

Fig. 1. Spontaneous radiation spectra of an InGaAs/AlGaAs/GaAs laser heterostructure with quantum dots measured through a window in the substrate for different values of the pumping current density.

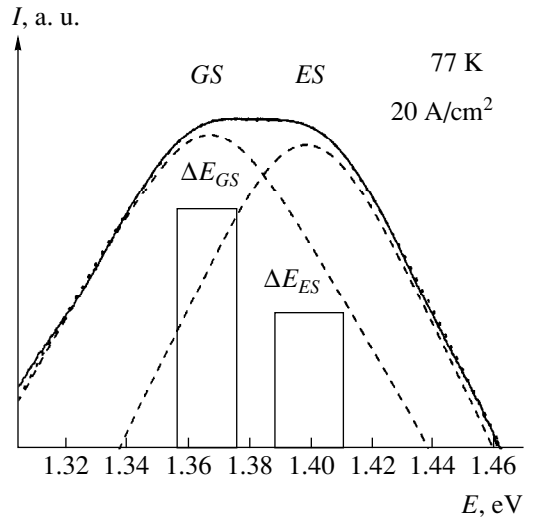

Fig. 2. A spontaneous radiation spectrum of a laser heterostructure with quantum dots (solid line). The points indicate the model spectrum, and the broken lines indicate the *GS* and *ES* components. Schematically shown by rectangles are the inhomogeneously broadened spectra for the ground and excited states of QDs.

pose, the samples were soldered to a heat sink, with their layers facing downwards, and then placed in a cryostat. The radiation was measured via special window in the upper contact of the laser structure. Special attention was given to the feedback suppression, the mirrors were etched and given a coat of black paint with a high refractive index. We have successfully used this method, which makes it possible to eliminate the effect of reradiation, in our earlier experiments [1, 2].

Figure 1 gives, on a semilog scale, the spectra of spontaneous radiation measured for different values of the pumping current density. Note the fact that, starting with even a low density of the injection current, several maxima are observed in the spectra. This situation is rather typical of the structures with QDs and is due to recombination via the ground and excited states of quantum dots [3].

It is obvious that the radiation spectrum has to be treated as a superposition of recombination via the ground and excited states, i.e.,

$$R(\hbar\omega) = R_{GS}(\hbar\omega) + R_{ES}(\hbar\omega), \qquad (5)$$

where R_{GS} and R_{ES} are the component spectra of radiation via the ground and excited states, respectively. The terms in the right-hand part of the equation are expressions analogous to (4) and differing from one another by the amplitude B, the characteristic energy of inhomogeneous broadening ΔE, and the transition energy E_0.

Figure 2 shows the experimentally obtained spectrum and the model spectrum constructed by formula (5) using the parameters selected by computer simulation. As is seen, the model spectrum coincides with the experimental one to within a high accuracy (of the order of 98%). It is only in the low-energy region that minor differences are observed. The characteristic energy of inhomogeneous broadening corresponding to the model and, consequently, experimental spectra is 17 meV for the ground state and 23 meV for the excited state. These values agree with the estimates of inhomogeneous broadening for QD (see, for example, the review by Ledentsov *et al.* [3]). The characteristic time of superradiation τ_N, estimated by the procedure described in [1, 2], was 14 fs for the ground state and 17 fs for the excited state, being virtually independent of the pumping current. The invariance of this parameter with respect to the pumping current agrees with the data obtained previously for structures with quantum wells [2].

Therefore, we have demonstrated for the first time that expressions of the theory of superradiation for a two-level system may be used to describe, with a high accuracy, the experimental radiation spectra of heterostructures with quantum dots using a small number of parameters which have a clear physical meaning. The model spectrum parameters made it possible to estimate the characteristic time of superradiation and the characteristic degree of inhomogeneous broadening. For this reason, the proposed model may be used for indirect investigation of the mechanisms of inhomogeneous broadening of radiation in low-dimensional structures.

This study received support from the Russian Foundation for Basic Research (project no. 98-02-18212, Investigation of Space-Time Structure of Radiation of Heterostructures on Quantum Wells and Quantum Dots in A3B5 Systems) and from the Competition–Appraisal of Projects Proposed by Young Scientists in the Russian Academy of Sciences in the Field of Basic and Applied Research.

REFERENCES

1. A. M. Georgievskiĭ, S. V. Zaĭtsev, N. Yu. Gordeev, V. I. Kopchatov, L. Ya. Karachinskiĭ, I. I. Novikov, and P. S. Kop'ev, Fiz. Tekh. Poluprovodn. **33**, 847 (1999) [Semiconductors **33**, 779 (1999)].
2. S. V. Zaĭtsev, N. Yu. Gordeev, L. A. Graham, V. I. Kopchatov, L. Ya. Karachinskiĭ, I. I. Novikov, D. L. Huffaker, and P. S. Kop'ev, Fiz. Tekh. Poluprovodn. **33**, 1456 (1999) [Semiconductors **33**, 1309 (1999)].
3. N. N. Ledentsov, V. M. Ustinov, V. A. Shchukin, P. S. Kop'ev, Zh. I. Alferov, and D. Bimberg, Fiz. Tekh. Poluprovodn. **32**, 385 (1998) [Semiconductors **32**, 343 (1998)].
4. D. Leonard, S. Fafard, K. Pond, Y. H. Zhang, J. L. Merz, and P. M. Petroff, J. Vac. Sci. Technol. B **12**, 2516 (1994).
5. V. M. Ustinov, A. Yu. Egorov, A. E. Zhukov, *et al.*, J. Cryst. Growth **175**/**176**, 689 (1997).

Translated by Henri A. Bronsteĭn

Technical Physics Letters, Vol. 26, No. 3, 2000, pp. 262–264. Translated from Pis'ma v Zhurnal Tekhnicheskoĭ Fiziki, Vol. 26, No. 6, 2000, pp. 84–89.

Selective Laser Sintering of PZT Ceramic Powders

D. M. Gureev, R. V. Ruzhechko, and I. V. Shishkovskiĭ

Samara State Technical University, Samara, Russia

Received April 30, 1999; in final form, September 27, 1999

Abstract—Conditions for the selective laser-induced layer sintering of a stoichiometric mixture of PbO, ZrO_2, and TiO_2 powders with the formation of bulk PZT ceramic articles were studied. The laser processing allows articles of the PZT ceramics to be obtained immediately in the course of sintering or upon additional annealing. Data on the microstructure and phase composition of the synthesized PZT ceramics are presented. © *2000 MAIK "Nauka/Interperiodica"*.

Articles made of the ceramic materials based on the solid solutions of lead zirconium titanium oxide system $Pb(Zr_xTi_{1-x})O_3$ (PZT) are traditionally obtained in the form of monolithic composites. These materials exhibit a piezoelectric effect and acquire polarization even upon the simplest forming process, which accounts for their wide application in various technologies. However, there are applications (medical ultrasonic equipment, hydrogeology, etc.) where maximum possible values of the hydrostatic charge d_h, hydrostatic voltage g_h, and the degree of acoustic matching (between the ceramics and ambient medium) [2] have to be provided, probably, at the expense of decrease in some less important parameters such as the piezoelectric modulus. Unfortunately, the traditional processing methods fail to provide for the obtaining of biocompatible bulk PZT ceramic articles of preset shape and low density. Thus, new technological processing schemes have to be developed.

In recent years, there has been progress in the technology of laser-induced layer synthesis of bulk articles from various powdered materials, known as the Rapid Prototyping or Solid Free Form Fabrication [3]. In particular, bulk articles of arbitrary shape can be obtained by a layer synthesis method based on the selective pouring of a polymer solution onto powdered PZT ceramics [4].

The purpose of this work was to study the possibility to replace one or several operations (sintering, molding), involved in the conventional PZT synthesis, by using selective laser layer sintering (SLS) technology.

The initial material for the sintering processing was prepared from powdered TiO_2 (State Standard STU 62), ZrO_2 (PTU 4357-53), and PbO (GOST 5539-50). According to [1], the component powders were mixed in the following proportion: 61.17% PbO, 20.87% ZrO_2, and 11.95 TiO_2. The SLS treatment was effected using a Nd:YAG laser. The maximum working laser power P (monitored by a TI-3 instrument) did not exceed 16 W. The laser beam was focused to a spot diameter of 50 μm and scanned in a computer-controlled regime over the material surface by a preset trajectory at a scan velocity V variable within broad limits. The SLS processing is described in detail elsewhere [5].

The microstructure of materials was studied using an optical microscope of the MVT-71 type. The phase composition of PZT ceramics was determined by X-ray diffraction on a DRON-3 diffractometer using CoK_α radiation. The synthesized bulk models were annealed in a vacuum furnace of the UVNSh-1600 type operated in the following regime [1]: temperature rise to 1000°C during 30 min; exposure at 1000°C, 10 min; increase in the temperature to 1240°C; annealing at 1240°C for 3 h.

In preliminary experiments, the powder composition was processed in a freely poured state, at a layer thickness definitely greater tan the sintered monolayer thickness. The parameters P and V were varied so as to determine the interval of possible sintering depths Z per laser beam scan, which ensured a minimum laser-induced deformation level. Figure 1 shows typical data characterizing the SLS process. At a low laser power, the sintered layer thickness was very small and the material disintegrated when touched. As the power P increases and the scan velocity V decreases, the sintered layer thickness grows (Fig. 1). This is accompanied by an increase in the level of laser-induced deformations, which reach a critical level at high laser powers. This is a negative factor hindering the fusion of sequential SLS layers to each other. Upon optimization of the laser processing conditions with respect to maximum strength and minimum warping of the sintered material, the following working parameters for the SLS processing of PZT ceramics were established: P = 11–14.5 W; V = 15–30 mm/s.

Using these experimentally established optimum conditions for the layer sintering, we have prepared and studied several bulk PZT samples. Three samples in the form of a parallelepiped were prepared using each of the following three fixed regimes: (1) P = 11.4 W, V = 30 mm/s; (2) P = 14.5 W, V = 30 mm/s; (3) P = 11.4 W,

V = 15 mm/s. The samples had a cross-section are of 10.1 × 10.1 mm and a height of ~3.2–3.5 mm.

Figure 2 shows photographs illustrating the microstructure of the laser-synthesized PZT ceramic samples. As seen, the material represents a porous system comprising equiaxial grains of grey color.

A typical grain size in the PZT samples upon SLS was ~0.36–0.45 mm (Fig. 2a) for an initial powder particle size of ~50 μm. The average material density was ~1.65 g/cm^3. The X-ray diffraction pattern from a sample obtained by SLS showed only weakly pronounced reflections. In our opinion, this is explained by the formation of large grains of finely-crystalline (almost amorphous) phase in the course of high-rate laser sintering. Unfortunately, we failed to identify the bright inclusions observed in the micrograph between the large grains. It should be noted that a similar pattern was observed in the PZT samples obtained by plasma-chemical synthesis [6].

In the next experiment, two samples from each group were annealed by the schedule descried above. The linear shrinkage did not exceed 10%. The average grain size upon annealing decreased to ~0.27–0.32 mm, while the density increased to 2.0 g/cm^3 (Fig. 2b). Data calculated using the X-ray diffraction pattern for the PZT ceramics upon annealing are presented in the table. As seen, the prolonged high-temperature annealing allowed the PZT phase formation to be accomplished, although the intensity of reflections due to oxide components are still rather high. Note that the problem of oxide separation is also encountered in traditional technologies [1] and has to be solved by thoroughly selecting the annealing conditions.

The sintered PZT samples with and without annealing were studied with respect to their polarization properties. The maximum electric field strength to which the samples could be exposed without breakdown was ~0.95 kV/mm. The breakdown developed predominantly via pores. However, filling pores with an epoxy resin only insignificantly increased the breakdown threshold. Upon preliminary experiments, the following regime was selected for polarization of the laser-sintered PZT samples: exposure to the electric field with a strength of 0.54 kV/mm for 2 h, followed by 40 min in an oil at 70°C. The X-ray diffractograms of samples polarized in this regime retained all the initial diffraction peaks, but their widths were somewhat greater compared to those observed for the nonpolarized annealed sample.

Thus, we have demonstrated the principal possibility of combining the operations of synthesis and forming for the obtaining of bulk PZT ceramic articles from a stoichiometric mixture of lead, zirconium, and titanium oxides, as confirmed by the data of X-ray diffraction measurements. Optimum regimes for the selective

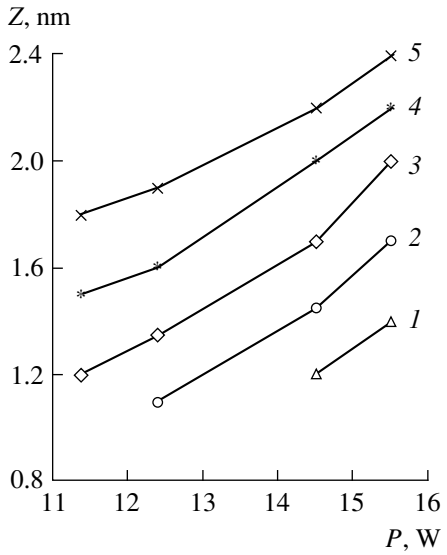

Fig. 1. The plots of sintered bulk layer thickness Z versus laser power P for various laser beam scan rates (mm/s): (*1*) 60; (*2*) 30; (*3*) 20; (*4*) 15; (*5*) 12.

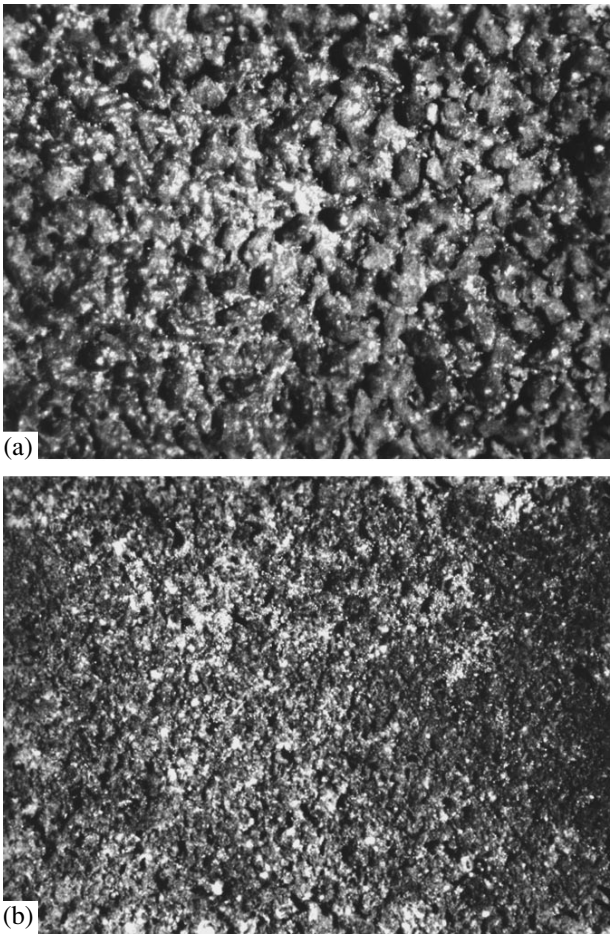

Fig. 2. Microstructure of the surface of laser-sintered PZT ceramic samples obtained by (a) SLS and (b) SLS + annealing (SLS regime: P = 14.5 W, V = 30 mm/s; magnification, ×16).

Table

I, arb. units	*d*, A	Phase
0.19	2.871	PZT
0.19	2.544	TiO_2
0.27	2.454	Pb
0.72	2.103	Pb_2O_3
1.00	1.809	PbO_2
0.04	1.672	PZT
0.28	1.662	PZT
0.18	1.569	–
0.22	1.440	PZT
0.13	1.403	–

laser sintering, the subsequent annealing leading to the formation of phases responsible for the piezoelectric properties of PZT ceramics, and polarization of the samples have been established. Simple model bulk articles of PZT ceramics were obtained

REFERENCES

1. I. A. Glozman, *Piezoceramics* (Énergiya, Moscow, 1972).
2. T. R. Gururaja, Am. Ceram. Soc. Bull. **73**, 50 (1994).
3. A. M. Ivanova *et al.*, Kvant. Élektron. **25**, 433 (1998).
4. A. Bandyopadhyay, R. K. Panda, *et al.*, J. Am. Ceram. Soc. **80**, 1366 (1997).
5. V. V. Bagrov *et al.*, Preprint Fiz. Inst. Akad. Nauk, No. 14, 19 (1996).
6. N. V. Dedov *et al.*, Fiz. Khim. Obrab. Mater., No. 1, 45 (1998).

Translated by P. Pozdeev

Technical Physics Letters, Vol. 26, No. 3, 2000, pp. 265–267. Translated from Pis'ma v Zhurnal Tekhnicheskoĭ Fiziki, Vol. 26, No. 6, 2000, pp. 90–94.

Epitaxial Garnet Ferrite Films with Anisotropy of the Inclined Easy Plane Type

R. M. Mikherskiĭ and S. V. Dubinko

Domain Design Bureau at the Simferopol State University, Simferopol, Ukraine

Received August 31, 1999

Abstract—The character of the magnetic anisotropy in epitaxial (112)-oriented garnet ferrite films has been studied. It is shown that at a certain ratio of the constants of uniaxial and orthorhombic anisotropy in these films, the anisotropy of the "inclined easy plane" type can appear. The possible application of epitaxial garnet ferrite films with the inclined easy-plane anisotropy in highly sensitive transducers of inhomogeneous magnetic fields is substantiated. © *2000 MAIK "Nauka/Interperiodica".*

Magnetooptical sensors based on epitaxial garnet ferrite films find increasing application for the visualization of inhomogeneous magnetic fields, e.g., those created in the magnetic information recording media. The most promising sensors of this kind are based on epitaxial garnet ferrite (EGF) films possessing the easy-plane-type anisotropy, which provide accurate determination of the intensity of an external magnetic field and its spatial distribution.

In the absence of an external magnetic field, an EGF film with the easy plane type anisotropy is uniformly magnetized in the film plane. Under the action of the normal field component of a signal recorded on an information carrier, the magnetic moment deviates from the film plane, which is the plane of easy magnetization (easy plane). The angle of the magnetic moment deviation from the film plane at any point of this plane depends on the magnitude of the normal component of the external field at this point. The appearance of the magnetization component along the direction normal to the film plane can be measured using the Faraday effect. Despite all the advantages of these sensors, they have insufficient sensitivity because the Faraday effect is sensitive toward the magnetization vector deviation from the easy plane, which is energetically less favorable than the motion of this vector within this plane. This motion cannot be determined using the Faraday effect, because the magnetization vector oriented in the easy plane has a zero projection onto the axis normal to the film plane.

One of the possible methods of increasing the sensitivity of magnetooptical sensors is the search for epitaxial garnet ferrite films possessing new types of magnetic anisotropy.

We had the aim to study the character of the magnetic anisotropy in (112)-oriented epitaxial garnet ferrite films.

The energy of the magnetic anisotropy for a (112)-oriented film can be represented as a sum of three terms, representing the uniaxial, orthorhombic, and cubic anisotropy components. Experiments show that

Table

Region	Relationships for constants	Solutions
1	$K_{ort} > 0$, $K_{ort} \le K_u < 2K_{ort}$	1) $\theta = \frac{\pi}{2} + \alpha$, $\varphi = \frac{\pi}{2}$; 2) $\theta = \frac{\pi}{2} - \alpha$, $\varphi = \frac{3\pi}{2}$
2	$K_{ort} \ge 0$, $K_{ort} \ge K_u$	1) $\theta = \pi - \alpha$, $\varphi = \frac{\pi}{2}$; 2) $\theta = \alpha$, $\varphi = \frac{3\pi}{2}$
3	$K_{ort} < 0$, $K_{ort} \ge K_u$	1) $\theta = \alpha$, $\varphi = \frac{\pi}{2}$; 2) $\theta = \pi - \alpha$, $\varphi = \frac{3\pi}{2}$
4	$K_{ort} < 0$, $K_{ort} \le K_u$	1) $\theta = \frac{\pi}{2} - \alpha$, $\varphi = \frac{\pi}{2}$; 2) $\theta = \frac{\pi}{2} + \alpha$, $\varphi = \frac{3\pi}{2}$
5	$K_u > 0$, $K_{ort} = 0$	$\theta = \frac{\pi}{2}$, $\varphi \in [0, \ldots, 2\pi]$
6	$K_u > 0$, $K_{ort} > 0$, $K_u > 2K_{ort}$	1) $\theta = \frac{\pi}{2}$, $\varphi = 0$; 2) $\theta = \frac{\pi}{2}$, $\varphi = \pi$
7	$K_u > 0$, $K_{ort} > 0$, $K_u = 2K_{ort}$	$\sin\varphi = -\sqrt{2}\cot\theta$

1063-7850/00/2603-0265$20.00 © 2000 MAIK "Nauka/Interperiodica"

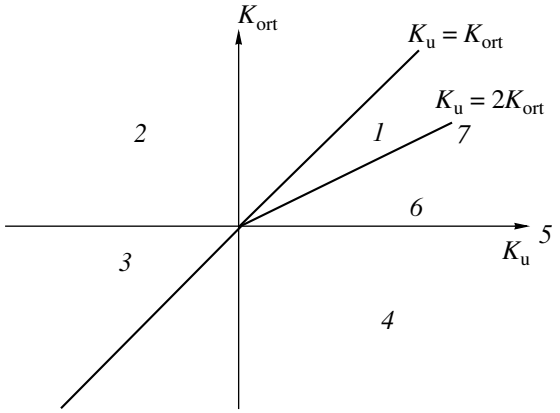

Fig. 1. Dependence of the regions of the equilibrium position of the magnetization vector on the constants of magnetic anisotropy.

the constant of the cubic anisotropy is lower by one–two orders of magnitude than the anisotropy constants of other types and therefore cannot considerably influence the process of magnetization reversal in the film. Ignoring the energy of the cubic anisotropy, we can represent the density of the magnetic anisotropy energy in the form

$$W = K_u \cos^2\theta + K_{ort}(\sin^2\theta \sin^2\varphi + \sqrt{2}\sin(2\theta)\sin\varphi),$$

where $K_u = K_u' + 2\pi M_s^2$, K_u' is the constant of the uniaxial anisotropy, M_s is the saturation magnetization, K_{ort} is the constant of the orthorhombic anisotropy, and φ and θ are the spherical coordinates of the magnetization vector measured along the *x*- and *z*-axes, respectively. In this case, the Cartesian *x*- and *y*-axes coincide with the crystallographic $[\bar{1}10]$ and $[\bar{1}\bar{1}1]$ directions, respectively, whereas the *z*-axis is oriented along the [112] direction lying in the plane normal to the film surface.

Minimizing (1) with respect to the spherical coordinates, we obtain solutions describing the equilibrium positions of the magnetization vector listed in table, where $\alpha = \frac{1}{2}\arctan\frac{2\sqrt{2}|K_{ort}|}{|K_{ort} - K_u|}$.

Figure 1 represent the tabulated data in a clear graphical form. In regions 1–4, the magnetization vector has two equilibrium positions corresponding to the magnetic anisotropy of the "angular phase" type. In particular, at the boundary between regions 2 and 3, the

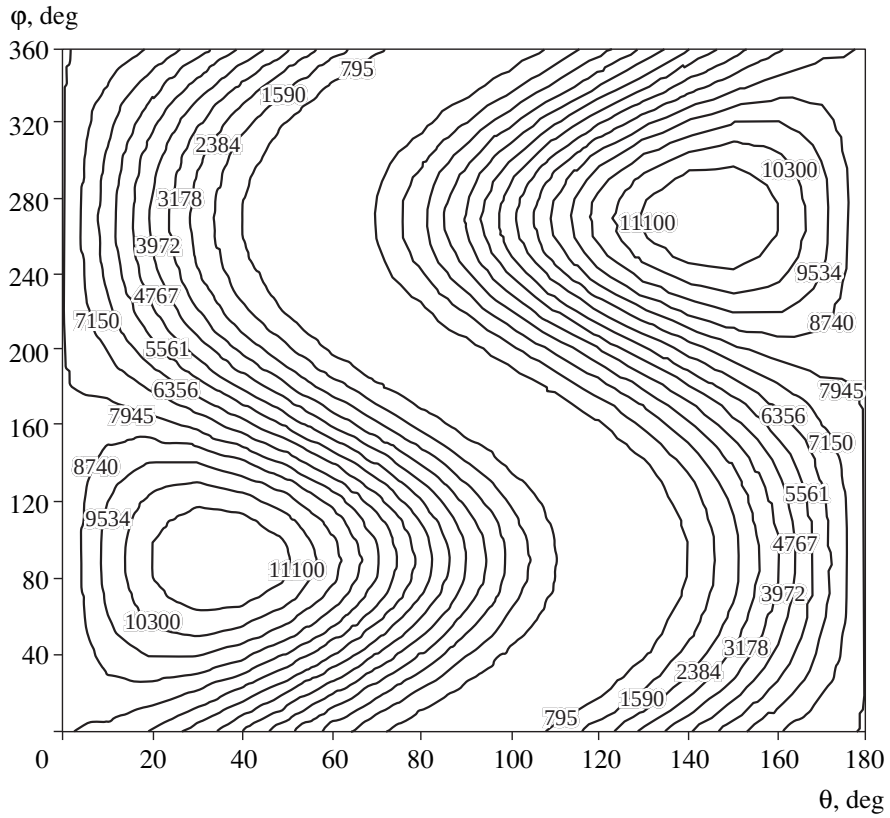

Fig. 2. Density of the magnetic anisotropy energy for a film with inclined easy plane type anisotropy at $K_u = 0.8 \times 10^4$ J/m^3 and $K_{ort} = 0.4 \times 10^4$ J/m^3 in the spherical coordinates φ and θ. Isolines connect the points with equal densities of the magnetic anisotropy energy indicated at each line.

"easy axis" type anisotropy exists. In region 5, the easy plane type magnetic anisotropy exists. In region 6, the "easy axis in the plane" type anisotropy takes place. The most interesting case of all those listed in table is that for $K_u > 0$, $K_{ort} > 0$, and $K_u = 2K_{ort}$ (region 7). Consider the energy of the magnetic anisotropy for this case, e.g., at $K_u = 0.8 \times 10^4$ J/m^3 and $K_{ort} = 0.4 \times 10^4$ J/m^3. Figure 2 shows this energy in the φ and θ coordinates. It is seen that, instead of two solutions corresponding to the minimum magnetic-anisotropy energy (as in regions 1 and 6), in this case the equation has only one solution—the surface defined by the expression $\sin\varphi = -\sqrt{2}\cot\theta$. Investigations showed that this expression can describe nothing but the plane intersecting the film plane along the crystallographic $[\bar{1}10]$ direction at an angle of 35°16′. By analogy with the easy plane, the plane corresponding to the minimum anisotropy energy is hereafter called "inclined easy plane."

The possible existence of EGF films with the inclined easy plane anisotropy is of considerable theoretical and practical interest, because such films can be used in highly sensitive transducers of inhomogeneous magnetic fields. Indeed, in the general case, a magnetization vector lying in the inclined easy plane has a nonzero projection onto the normal to the film surface and, therefore, changes in its position in this plane can be detected with the use of the Faraday effect.

In the above model, the films with the inclined easy plane anisotropy should be sensitive to infinitely weak magnetic fields. Indeed, any field with a nonzero projection onto the inclined easy plane lifts the degeneracy along this projection. Therefore, the real sensitivity should be evaluated upon introduction of the energy of cubic anisotropy into expression (1). The corresponding calculations show that, even upon the allowance for the cubic anisotropy, the sensitivity of such films to external magnetic films is the higher (at least by one–two orders of magnitude) than the sensitivity of the films with the easy plane anisotropy presently used in magnetic field sensors.

Translated by L. Man